The Thesis Committee for Jonathan Grant Martin
certifies that this is the approved version of the following thesis:

Measuring Liquefaction-Induced Deformation from Optical Satellite Imagery

APPROVED BY
SUPERVISING COMMITTEE:

Supervisor:

Ellen Rathje

Brady Cox

Measuring Liquefaction-Induced Deformation from Optical Satellite Imagery

by

Jonathan Grant Martin, B.C.E.

Thesis

Presented to the Faculty of the Graduate School of

The University of Texas at Austin

in Partial Fulfillment

of the Requirements

for the Degree of

Master of Science in Engineering

The University of Texas at Austin

May 2014

Dedication

To my wife, thank you for all your love, encouragement, and support. You have been with me every step of the way, including many late nights. I love you, and I could not have accomplished this without you.

Acknowledgements

I would like to thank Dr. Ellen Rathje for her support and guidance through the completion of this research. I greatly appreciate the time and dedication she invested, and her patience and insight have proven invaluable. I am truly honored to have worked with such an intelligent and innovative individual. I also want to thank Dr. Brady Cox for his support and willingness to give his time and expertise.

I would like to thank my wife, parents, and brother for their support throughout my time at the University of Texas. Your prayers and encouragement have been instrumental in the completion of this thesis.

I would also like to thank the other professors at the University of Texas who have invested in my professional and personal development. I have learned more than I could have imagined while at UT. Additionally, I appreciate the support from my fellow graduate students, especially Oscar Suncar who taught me much of what I know about optical image correlation.

Finally, I want to thank the USGS, Department of Interior for their financial support on this project. Funding was provided under grant G13AP00027. The views and conclusions contained in this document are those of the author and should not be interpreted as necessarily representing the official policies, either expressed or implied, of the U.S. Government.

Abstract

Measuring Liquefaction-Induced Deformation from Optical Satellite Imagery

Jonathan Grant Martin, M.S.E.

The University of Texas at Austin, 2014

Supervisor: Ellen Rathje

Liquefaction-induced deformations associated with lateral spreading represent a significant hazard that can cause substantial damage during earthquakes. The ability to accurately predict lateral-spreading displacement is hampered by a lack of field data from previous earthquakes. Remote sensing via optical image correlation can fill this gap and provide data regarding liquefaction-induced lateral spreading displacements. In this thesis, deformations from three earthquakes (2010 Darfield, February 2011 Christchurch, and 2011 Tohoku Earthquakes) are measured using optical image correlation applied to 0.5-m resolution satellite imagery. The resulting deformations from optical image correlation are compared to the geologic conditions, as well as field observations and measurements of liquefaction. Measurements from optical image correlation are found to have a precision within 0.40 m in all three cases, and results agree well with field measurements.

Table of Contents

List of Figures

Chapter 1: Introduction

1.1 Research Significance and Objectives

During earthquakes, loose, saturated soils may lose strength in a phenomenon known as liquefaction. Liquefaction manifests itself in many ways including slope failures, foundation failures, extreme settlement, sand boils, and lateral spreads. Lateral spreads occur as soil on a gentle slope or river bank liquefies and flows downslope or into the river, often developing cracks perpendicular to the direction of movement and causing extensive damage. Lateral spread deformation can cause significant damage to overlying infrastructure such as roads, bridges, buildings, as well as subsurface infrastructure like pipelines, utilities, and tunnels. Figure 1.1 shows a lateral spread from the 2010 Haiti Earthquake. Extensive cracking is oriented perpendicular to the waterway, and the depth of the affected soil is significant. Both overlying structures and subsurface infrastructure were affected by these deformations. Although this spread terminates within 50 meters of the waterway, lateral spreads may extend further inland for a few hundred meters. For example, the lateral spread in Figure 1.2 covers a much larger area. Again, cracking runs roughly perpendicular to the waterway. Extensive damage to the round structure, parking lot, roadways, and surrounding areas is clearly visible, and a large crack extends through the center of the structure's foundation.

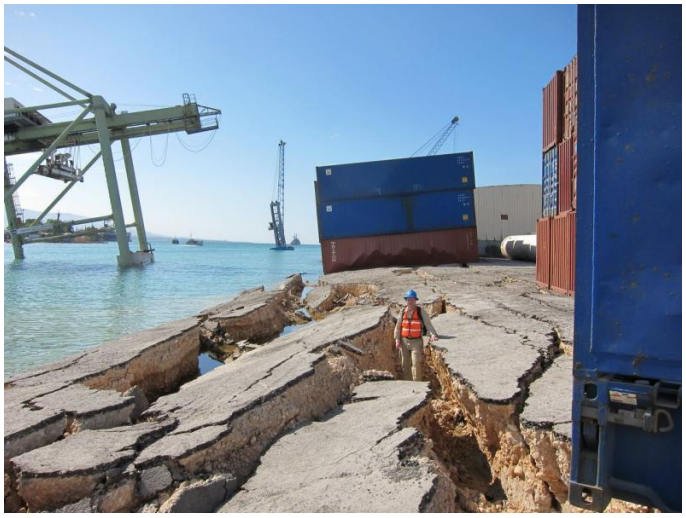

Figure 1.1. Lateral Spreading (EERI 2010).

Figure 1.2. Lateral Spread with Large Spatial Extent (www.caee.utexas.edu, accessed 2013)

Due to the complex nature of lateral spread mechanics, empirical models are typically used in practice to assess an area's susceptibility to lateral spread deformation and predict displacements in the event of an earthquake (Glaser 1994). More advanced numerical models derived from finite element analyses and theoretical liquefaction

mechanics exist as well. However, all methods are limited by the quantity, quality, and accuracy of the lateral spread measurements used to develop or calibrate the models.

Traditionally, lateral spread displacement is measured manually using the widths of the cracks associated with lateral spreading. For example, if a lateral spread has occurred near a river, the widths of cracks running perpendicular to the orientation of displacement are measured, typically with a tape or GPS measurements on either side of the crack. Figure 1.3 illustrates the typical measurement of lateral spread induced cracking. Only cracks caused by the lateral spread are measured, and these crack widths are summed to determine the displacement of the lateral spread. However, this approach assumes that all lateral spread deformation is manifested in cracks and that the materials between cracks act as rigid blocks.

(a) Measurement of Crack using Tape (b) Measurement of Crack with GPS

Figure 1.3. Traditional Measurement of Lateral Spreads (Robinson et al. 2011)

Such manual measurements present many challenges. They are time consuming and labor intensive. Assessment of only a few kilometers along a river may take weeks to perform, even with a sizable crew. The time and labor requirements translate to high costs. Additionally, the large spatial extent of many lateral spreads causes difficulty in

determining the termination of lateral spread induced cracking. At far distances from the toe of the spread, visible cracking may not be due to lateral spreads, but other earthquake related phenomena. Accessibility of obstructed areas can be an issue with manual measurement as well. Last, recognition of cracking and the determination of crack widths are often difficult. Cracks may be hidden under debris or sand boils, and cracks which can be seen may not have an obvious cause. After determining a crack is associated with a lateral spread, the measurement of its width requires judgment and skill. For example, the width may be overestimated if the sides of the crack have slumped.

Measurements of deformation using optical image correlation can mitigate these challenges. In optical image correlation, a pre-earthquake image of an affected area is compared with a post-earthquake image of the same area. A map of lateral displacements is produced from this comparison, and lateral spread displacement measurements can be determined from this map. A single person can perform a correlation analysis of images covering over 30 km^2 in just a few days, which is must faster than field measurements. Additionally, a pair of 0.5 m resolution satellite images can be purchased for less than $500, making this approach cost effective. Imagery of areas which are inaccessible in the field may be attainable with satellites or aerial photography. Because displacements derived from this method are based on identifying homologous areas, measurements are not dependent on judgments of cracking patterns and widths. With optical image correlation techniques, existing databases of lateral spreading measurements can be expanded and diversified to include lateral spread deformation measurements that traditional techniques are unable to capture. With better displacement databases, better models can be developed for assessing lateral spread susceptibility, predicting lateral spread displacements, and mitigating lateral spread potential.

The research discussed in this thesis aims to apply optical image correlation to measure lateral spreads from the 2010 Darfield Earthquake in New Zealand, the February 2011 Christchurch Earthquake in New Zealand, and the 2011 Tohoku earthquake in Japan.

1.2 THESIS ORGANIZATION

Following this introduction, Chapter 2 discusses the optical image correlation process and its previous uses. A brief overview of the process is followed by an in depth explanation of its methodology, and previous uses of optical image correlation to measure deformations are discussed.

Chapter 3 applies optical image correlation to the February 2011 Christchurch earthquake. Areas in Christchurch, New Zealand are analyzed to estimate lateral spread displacements. Characteristics of the earthquake are discussed, and the results of the optical image correlation process are presented. Deformation results are presented with comparisons to expected displacement patterns and field measurements.

In Chapter 4, optical image correlation is used to measure lateral spread deformation in Kaiapoi, New Zealand from the 2010 Darfield Earthquake. Earthquake characteristics are presented, and the specific image correlation process is recounted. Results are examined with comparisons to expectations and field measurements.

Chapter 5 uses optical image correlation to quantify lateral spread deformation near Katori, Japan from the 2011 Tohoku earthquake. After a discussion of the earthquake, the image correlation as applied to the Katori imagery is reviewed. Results with comparisons to expected patterns and field measurements are presented.

Chapter 6 contains a summary of the information presented in this thesis with concluding remarks.

Chapter 2: Optical Image Correlation

2.1 Introduction

This chapter will describe the methodology of the correlation process used for the analyses presented in later chapters. Previous uses of optical image correlation also are discussed. In Section 2.2, the methodology is broken into its five main steps and each component is discussed in detail. Finally, Section 2.3 briefly reviews previous uses of optical image correlation as they relate to geotechnical and earthquake engineering.

2.2 Methodology

The optical image correlation process can be divided into three categories: (1) pre-processing, (2) correlation analysis, and (3) post-processing. A flow chart of the process is shown below in Figure 2.1. In pre-processing, an image pair is selected and distortions in the images are corrected through orthorectification and co-registration. During the correlation analysis, displacements are determined. Finally, in post-processing, the results are filtered and derivative products such as transects, vector maps, and displacement contour maps are created from the correlation results.

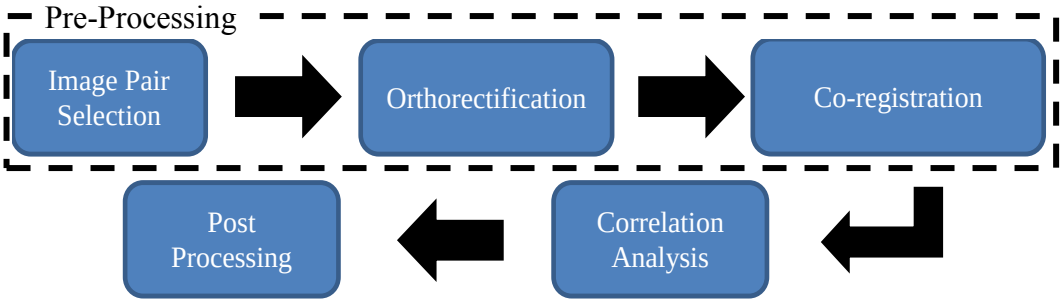

Figure 2.1. Image Correlation Process Flow Chart

2.2.1 Image Pair Selection

The properties of the selected images have the greatest influence on the quality of results. Images are selected on three main criteria: (1) coverage, (2) cloud cover, and (3) acquisition geometry. Images must contain the region of interest and surrounding areas. A significant area surrounding the region of interest is required because these areas are used in the co-registration process to reduce distortions. Additionally, images must be free of significant cloud cover near the region of interest. Last, but certainly not least, the acquisition geometry must be favorable.

The acquisition geometry describes the location of the optical sensor relative to the location of the target image on the surface of the earth. Typically, the acquisition geometry is described using one of two parameter sets: (1) the off-nadir (i.e., off-vertical) and azimuth angles or (2) the sensor's path azimuth, cross-track, and in-track angles. Figure 2.2 illustrates the angles used to describe the line-of-sight from an optical sensor on a satellite to a point in an image (i.e. a pixel). Using the first parameter system, the off-nadir angle is represented by ϕ_L and the azimuth angle is θ_L. The second parameter system is referenced by T, S, and θ_0, which represent the cross-track, in-track, and orbital path azimuth angles, respectively. Note that the azimuth angles in both systems are measured clockwise from north. These angles are related by the following equations.

$$\tan(\phi_L) = \sqrt{\tan^2 S + \tan^2 T} \tag{2.1}$$

$$\tan(\theta_I) = \frac{\tan(S)}{\tan(T)} \tag{2.2}$$

$$\theta_L = \theta_I + \theta_0 \tag{2.3}$$

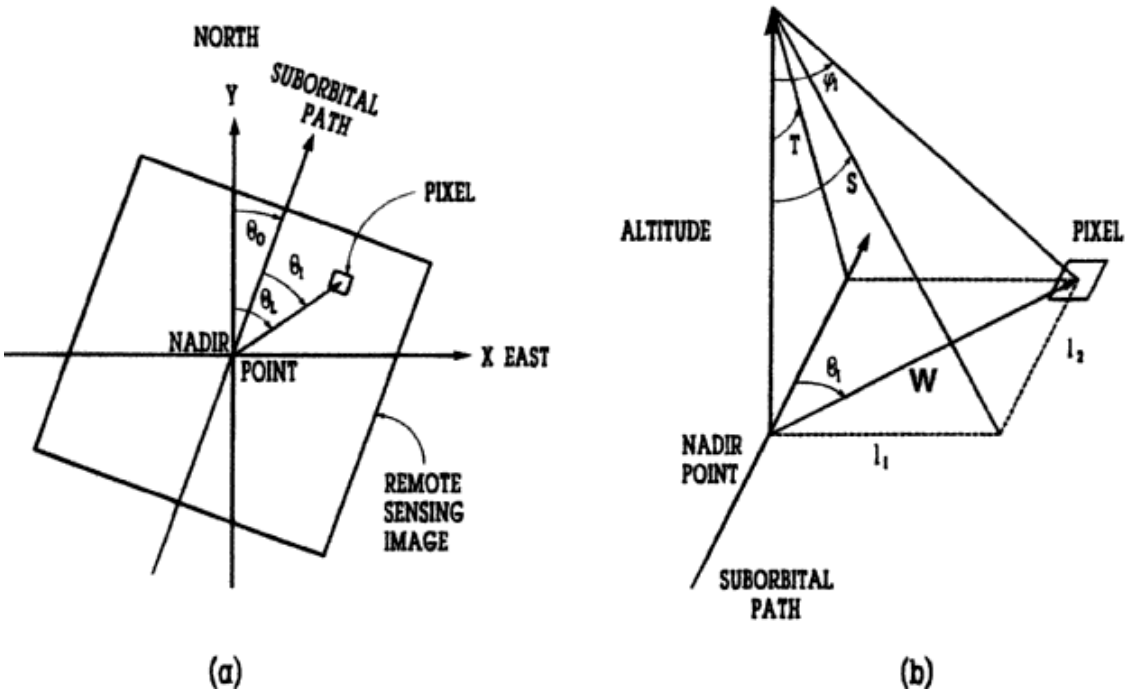

Figure 2.2. Acquisition angles from (a) plan view and (b) isometric view. Note: (b) shows angles referenced from the satellite orbital path (Bukata 1977)

Two important considerations must be made regarding acquisition angles when selecting image pairs. First, the off-nadir angle should be minimized because distortions due to the topography of the target area are greater when the off-nadir angle is greater. Second, the acquisition angles of the pre-event image should be similar to those in the post-event image. As the acquisition angles differ more from each other, apparent (not true) displacements may be obtained from the analysis. Additionally, patterns of pixels are more easily identifiable if the post- and pre-event images are captured from the same perspective.

2.2.2 Orthorectification

Orthorectification corrects for geometric distortions such as relief displacement to generate a nadir (i.e., vertical) view of the target. Relief displacement is the difference in the perceived position of an object from its actual position due to parallax. Figure 2.3 illustrates relief displacement of an office building. Because the building is viewed from an angle, its roof is incorrectly placed. Figure 2.4 shows two images in which the effects of relief displacement are clearly visible. The top of the water tower appears in different locations depending on the acquisition angle of the image. Relief displacement is magnified when an object is viewed at a greater off-nadir angle and when topographic variation is larger.

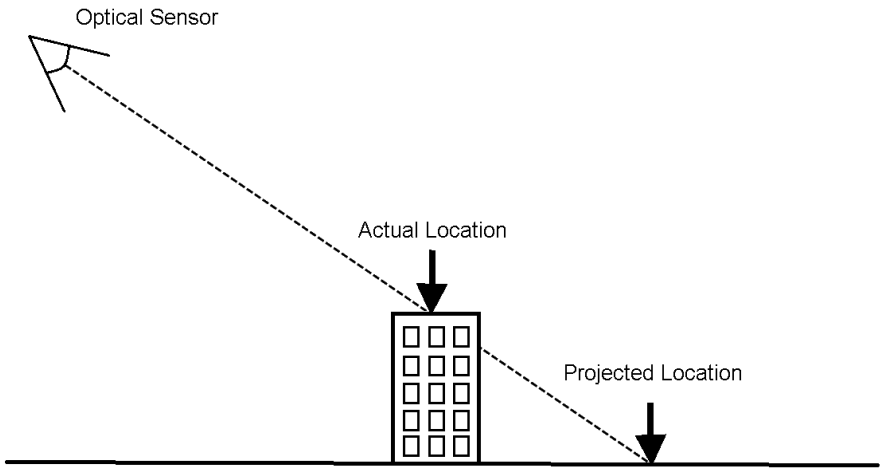

Figure 2.3. Relief displacement due to off-nadir angle.

L  R

Figure 2.4. Relief displacement of top of water when viewed from left and right of tower. (Bethel 2014)

Another common geometric distortion is one of scale. Figure 2.5 (a) shows a profile view of an area with three equally sized features. Without geometric corrections, object (2) will appear smaller than the other objects because it is further away (Figure 2.5b). After orthorectifying the image, all three objects are the same size (Figure 2.5c).

Orthorectification uses a digital elevation model (DEM) of the ground surface and an image's acquisition angles to correct geometric distortions. Typically, the DEM resolution is coarser than the distorted image, so all distortions are not removed through orthorectification. Additionally, some distortions of buildings are not removed because the elevations of buildings are not included in the DEM.

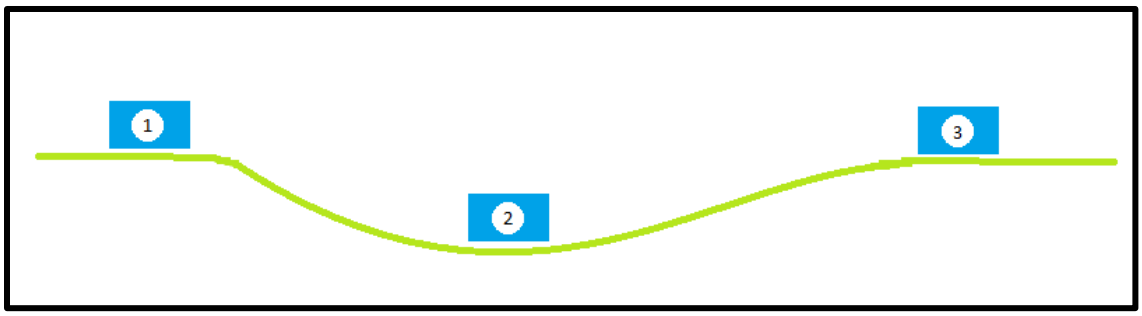

(a) Profile view

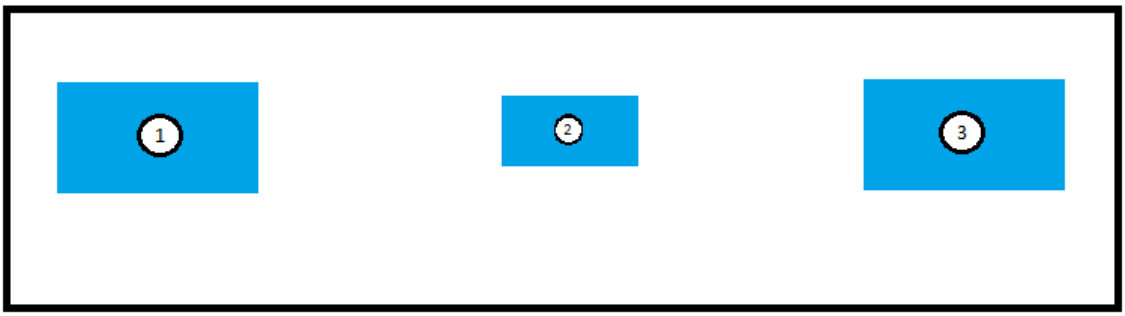

(b) Plan View – Pre-orthorectification

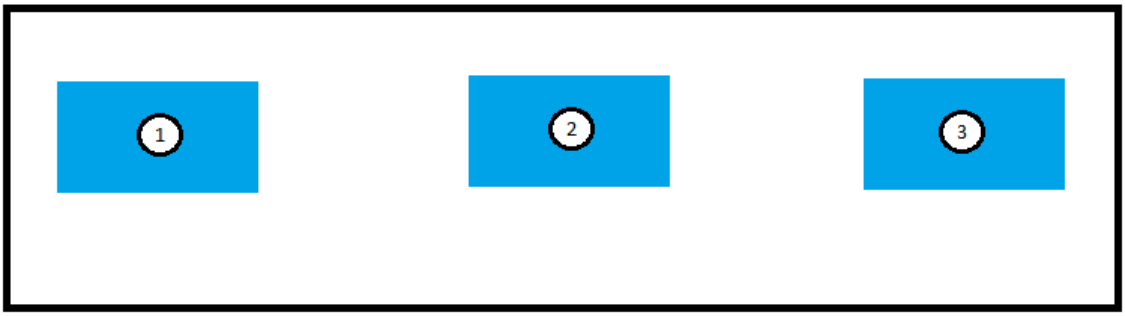

(c) Plan View – Post-orthorectification

Figure 2.5. Using orthorectification to correct scale: (a) profile view of area with three equally sized features, (b) plan view of acquired image before orthorectification, and (c) plan view after orthorectification.

2.2.3 Co-registration

Co-registration involves precisely aligning the pre- and post-event images. Distortions and geo-referencing errors that remain after orthorectification are mitigated

through co-registration. Co-registration warps the post-event image so that defined tie points (i.e., homologous points between the images) are at the same location when overlaid. The post-event image is warped using a first order polynomial that is fit with selected tie-points.

Tie points are generated using an automated process in which groups of pixels in the pre-event image are compared with those in the post-event image. While the specific implementation of the automatic tie-point generation may vary, most area-based tie point generation processes are similar to that which is illustrated in Figure 2.6 and described in Gao et al. (2009). A given group of pixels (chip window) in the pre-event image (red box in Figure 2.6) is compared to multiple groups of pixels in the post-event image (green and orange boxes in Figure 2.6). For each comparison, a correlation coefficient is calculated to reflect the quality of match. The post-event chip window with the highest correlation coefficient is assumed to match the pre-event chip window. This process is repeated at multiple locations to obtain tie-points.

Figure 2.6. Optical Image Correlation Process.

Automated tie-point generation methods work well in areas with unique features that manifest themselves in variations in pixel values or texture (e.g. urban areas). However, these methods are less reliable in areas with few features or homogenous texture (e.g. rural areas with fields). Figure 2.7 illustrates the use of automated tie-point generation methods in areas with little texture (Figure 2.7a) and significant texture (Figure 2.7b). In this figure, the correlation coefficient is plotted again the location index, which represents the shift applied to the pre-event chip window within the post-event image. In Figure 2.7a, multiple locations potentially match the pre-event chip window, so a false positive is more likely. Conversely in Figure 2.7b, the pre-event chip window clearly matches one location in the post-event image. Therefore, the automated tie-point generation is more reliable in areas with unique features/texture.

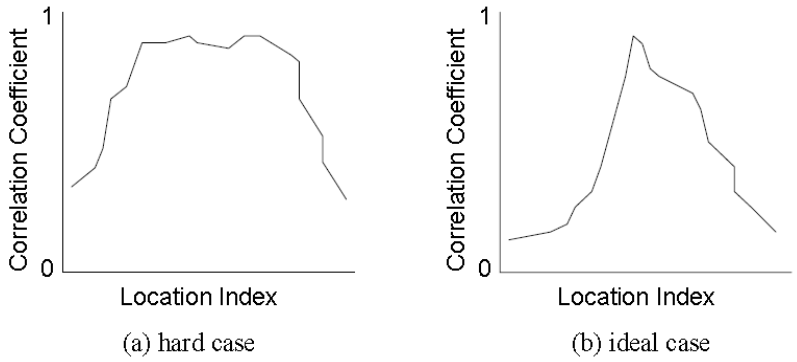

Figure 2.7. Comparison of automated tie point generation in two areas (Gao et al 2009).

Once tie-points have been generated, they are filtered to ensure the first order polynomial is fit using only appropriate tie-points. Tie points in areas of expected displacement (e.g. near rivers) are removed. Remaining tie points are assessed by fitting the first order polynomial with the points and calculating the residuals for each point. In

addition, a root mean square error (RMSE) is determined for the entire fit and represents the scatter of all points about the best fit line. Because the first order polynomial can only account for distortions common throughout the whole image, tie points with high residuals are likely false positives or located in areas of localized deformation. Therefore, tie points with high residuals are removed until an acceptable RMSE is reached with an appropriate density and distribution of tie points.

2.2.4 Correlation analysis

Correlation analysis provides estimates of displacement across an area in a process similar to that of the automated tie point generation described above. Figure 2.6 can be used again to illustrate the correlation analysis. The pre-event image is divided into patches of pixels, called chip windows. For each chip window in the pre-event image, a search is performed in the post-event image to find the location of the same chip. For example, the red square in the pre-event image (Figure 2.6) outlines a chip window centered at location (x1, y1). In the post-event image, the chip window first is compared to the pixels at the same (x1, y1) position (shown in green in Figure 2.6). The comparison is quantitatively measured with a correlation coefficient between the corresponding pixel values within the two chips. The chip also is compared to surrounding locations (illustrated by the orange squares in Figure 2.6), and a correlation coefficient is calculated for each location. The chip with the highest correlation (the red square in the post-event image in Figure 2.6) is considered the best match, and this location is taken as the location of the pre-event chip in the post-event image. A signal-to-noise ratio (SNR) is assigned to the match reflecting the quality of correlation (1 = perfect correlation; 0 = no correlation). The position of the best-match chip in the post-

event image (x2, y2) is compared with the position in the pre-event image (x1, y1) to obtain relative east-west and north-south displacements. The correlation process has been shown to be accurate to 1/20 of a pixel using some algorithms (Leprince et al. 2007). Therefore, the precision of the displacement measurements is typically controlled by the precision of the co-registration process.

The selection of the chip window size significantly influences the pattern of results. A correlation measurement represents an average displacement across an entire chip window, and thus smoothing of displacement is greatest for large chip windows. Correlation using small chip windows produces less averaging and more localized estimates of displacement, but noisy, incoherent displacement patterns are more likely due to false matches. Therefore, the smallest chip window that produces an acceptable level of noise should be used. The spacing at which a new chip is compared is called the step size. A smaller step size produces more displacement measurements but is more computationally intensive.

2.2.5 Post-Processing

Post-processing involves filtering the displacement estimates by their SNR and creating derivative products from the correlation results. Displacement estimates under a specified SNR are removed such that only displacements from well-correlated chips are present. The minimum allowable SNR is determined based on the use of the end products.

The smallest detectable displacement magnitude should also be assessed during post-processing. As noted in the discussion on correlation analysis, the limiting precision typically comes from the co-registration process. Specifically, the RMSE from the co-

registration provides important information on the variability of displacement in non-moving areas. The RMSE essentially represents the scatter (i.e., standard deviation) of the tie points about the best-fit warping polynomial and thus is a measure of the variability of displacement in non-moving areas. Therefore, the RMSE can be used to estimate the minimum detectable displacement magnitude.

From the correlation results, many derivative products can be generated. Maps showing displacement in different directions (e.g. North/South and East/West directions) or as amplitude (i.e. square root of sum of components squared) can be created. Transects showing displacement versus distance from the riverbank and vector arrows can be derived from the correlation results. Even contour maps showing displacement concentrations are possible.

2.3 Previous Uses of Optical Image Correlation to Measure Deformations

Optical image correlation has previously been used in geotechnical and earthquake applications. Hamada et al. (1987) used two aerial photographs of Noshiro City, Japan to measure liquefaction induced lateral displacements from the 1983 Sea of Japan Earthquake. Hamada et al. (1987) compared an image taken in 1981 to one acquired seven days after the earthquake. They first aligned the images by identifying points in areas that were assumed to have no permanent displacement. Next, points in the moving areas were manually identified in both images to determine a relative displacement. Where possible, manhole covers, bases of lamp-posts, corners of drainage channels, and property boundary stones were used as reference points. When such objects could not be found, corners of buildings were used. Figure 2.8 shows some points used to measure permanent displacement on Maeyama Hill in Noshiro City. Once

points were identified, they were assigned a location based on a coordinate system. By comparing the coordinate position of the object in the pre- and post-event images, the lateral displacement was quantified. Hamada et al. (1987) estimated the error in these measurements as being no greater than 20 cm. They used the same technique to estimate displacements near Niigata, Japan from the 1964 Niigata Earthquake.

Figure 2.8. Location of lateral displacement measurements near Noshiro City, Japan; measured points shown as circles (Hamada et al. 1987).

With advances in computing technology, optical image correlation techniques are now automated. Many researchers have estimated earthquake fault rupture displacement using optical image correlation. Binet and Bollinger (2005) measured the fault

displacement of the 2003 Bam (Iran) earthquake with a pair of SPOT-5 panchromatic images (2.5 m pixel width). They used the correlation technique described by Van Puymbroeck et al. (2000), which matches pre- and post-event areas through Fourier transforms. Figure 2.9 shows the area of their analysis and the correlation results. With a correlation window size of 256 pixels (640 m) and a step size of 64 pixels (160 m), they measured right lateral strike slip displacement of roughly 0.77 ± 0.05 m on average. Near the center of the fault rupture, their measurements showed a maximum displacement of 1.2 ± 0.15 m. These measurements were larger than field estimates (average field displacement was estimated at 0.2 m), but the authors believe the field estimates are under predictive because they only represent discrete rupture along the fault.

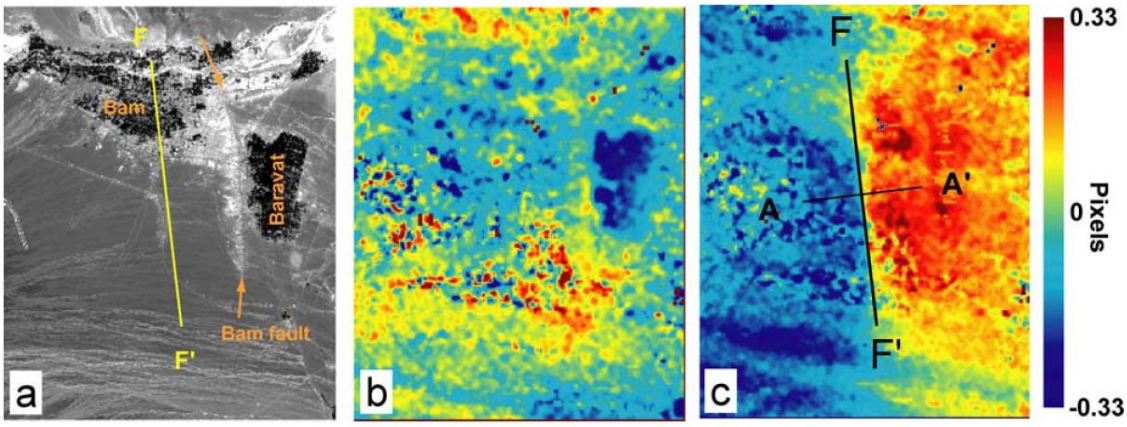

Figure 2.9. Image and map of displacements induced by Bam (Iran) earthquake: (a) SPOT optical image, (b) east/west component of displacement, and (c) north/south component of displacement. Note the fault displacement along F-F' is clearly visible (Binet and Bollinger 2005).

Debella-Gilo and Kääb (2012) used an area-based optical image correlation process (Least Squares Matching (LSM) algorithm) to assess displacement and strain

rates of three mass movements: a glacier flow, a rockglacier creep, and a landslide. While the correlations for the glacier flow and rockglacier creep yielded positive results, only the land slide analysis will be discussed in detail as it most closely relates to the topics in this thesis. Two Quickbird satellite images from September 2003 and September 2010 were analyzed to determine the displacement and seven-year average velocity of the La Clapière landslide in the French Alps near the town of Saint-Etienne-de-Tinée. Figure 2.10 shows a portion of the 2003 Quickbird image. These images have a pixel resolution of 0.6 m, and the co-registration process yielded a mean error of about 1.2 m, or 2 pixels. Using a window size of 51 pixels (30.6 m), displacements were calculated. Figure 2.11 shows the correlation results. The spatial pattern of displacement agrees with results from other studies, particularly with the results of Casson et al. (2003) where points were manually compared in two stereoscopic aerial images acquired 17 years apart. While the spatial pattern of displacement from Debella-Gilo and Kääb (2012) compared well with other studies, uncertainty in the displacement measurements was high. Specifically, the average displacement measured outside the landslide area (i.e. non-moving areas) was 2.01 pixels (1.2 m), so calculated displacement measurements were within the error margin. Therefore, the reliability of the displacement magnitudes is questionable. Since the mean precision of the LSM algorithm was found to be within 0.06 to 0.15 pixels (0.04 to 0.09 m), the uncertainty in measurements was controlled primarily by errors in the co-registration process.

Figure 2.10. 2003 Quickbird Image of La Clapière landslide (Debella-Gilo and Kääb 2012).

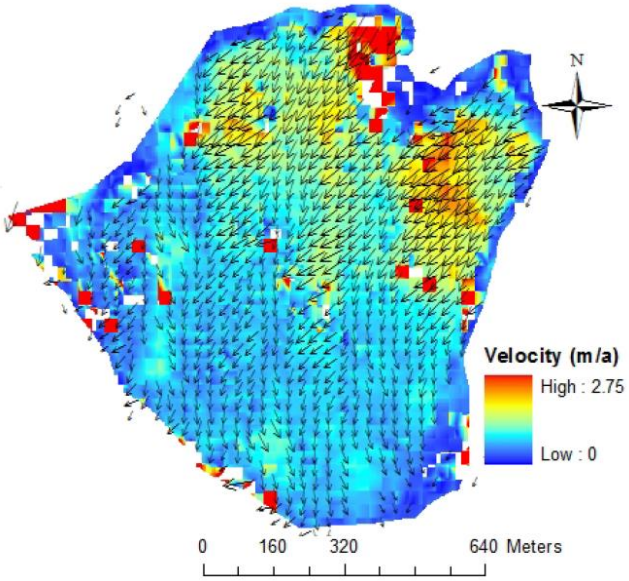

Figure 2.11. Displacement rate results of La Clapière landslide correlation (Debella-Gilo and Kääb 2012).

Suncar et al. (2013) measured the displacement of the Portuguese Bend landslide in Los Angeles County using the optical image correlation process discussed in Leprince et al. (2007). Figure 2.12 shows the location of the landslide. Correlating two panchromatic images with 0.5 m pixel resolution acquired in August 2010 and May 2011

with a 128 pixel (64 m) window size, they determined the magnitude and extent of landslide deformations and compared their results to measurements from 64 GPS benchmarks within and around the landslide area. Figure 2.13 shows the deformation results along with those inferred from GPS measurements. Displacements from 0.5 m to greater than 6 m were measured. Measurements from optical image correlation agreed well with GPS measurements and provided a more coherent deformation pattern than could be derived solely using the GPS measurements.

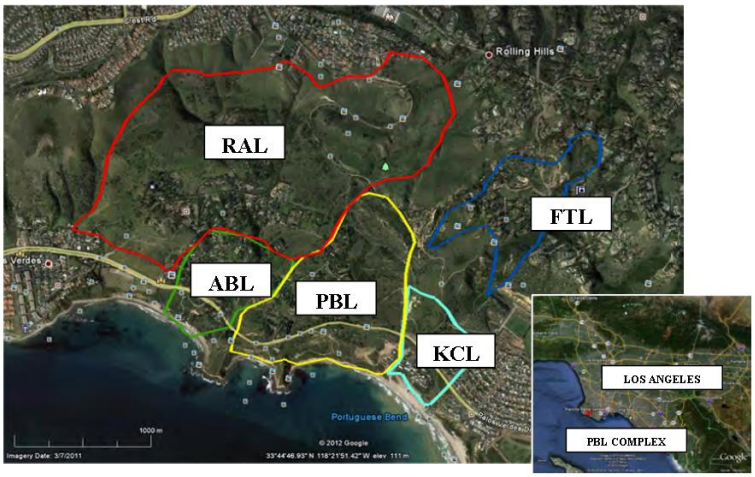

Figure 2.12. Location of Portuguese Bend Landslide (PBL) (Suncar et al. 2013)

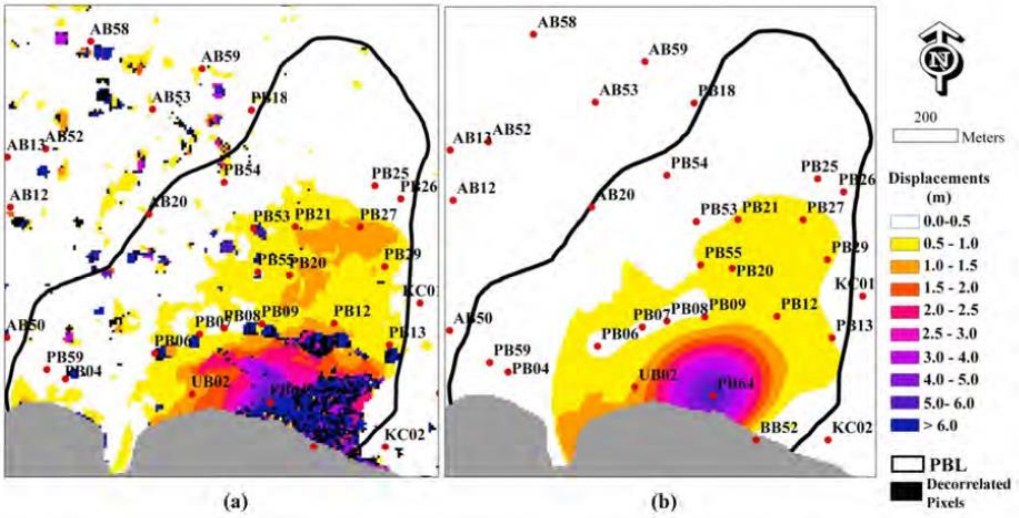

Figure 2.13. Comparison of displacement patterns: (a) displacements from optical image correlation and (b) displacements from GPS measurements. Note: the precision in defining the landslide geometry is greater with the optical image correlation results (Suncar et al. 2013).

Chapter 3: Optical Image Correlation Analysis of Lateral Spread Displacements from the February 2011 Christchurch, New Zealand Earthquake

3.1 INTRODUCTION

This chapter describes the use of optical image correlation to measure liquefaction-induced horizontal deformation near Christchurch, New Zealand from the February 2011 Christchurch Earthquake. Section 3.2 discusses the characteristics of the February 2011 Christchurch Earthquake, and Section 3.3 presents the region of analysis, the specifics of the image correlation process, and the statistical characteristics of the results. In Section 3.4, the results of the correlation analysis are examined and compared with the near surface geology and measured deformation patterns from ground observations, crack measurements, LiDAR correlation, and transect surveys.

3.2 FEBRUARY 2011 CHRISTCHURCH EARTHQUAKE

On February 22, 2011, a M_w=6.3 earthquake occurred near Christchurch, New Zealand severely damaging infrastructure and claiming 181 lives (Cubrinovski et al. 2011). Figure 3.1 shows the city of Christchurch, surrounding neighborhoods, and the epicenter of the earthquake. Much damage was caused by severe liquefaction and lateral spreads in and around the Christchurch Central Business District (CBD) and surrounding neighborhoods. In particular, lateral spreading due to liquefaction caused permanent horizontal displacements of more than 2 m in the neighborhoods along the Avon River to the east of the CBD (Cubrinovski et al. 2011). Figure 3.2 shows a lateral spread in a

surrounding neighborhood of Christchurch. The lateral spread caused permanent displacement toward the Avon River, and the affected areas were severely damaged.

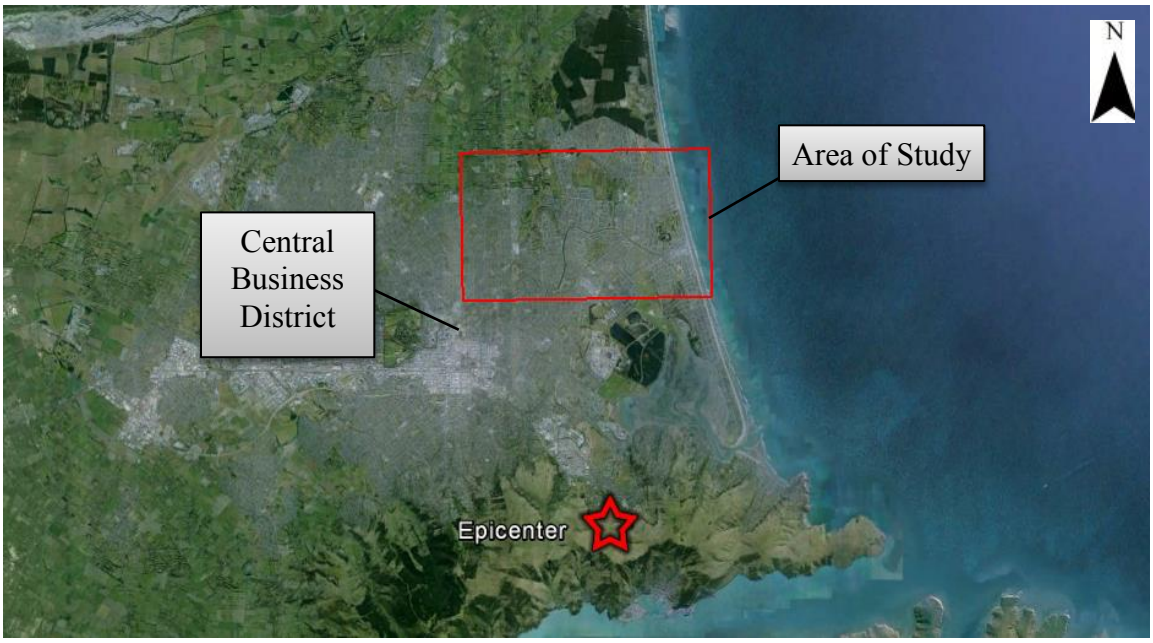

Figure 3.1. Area of study for the February 2011 Christchurch Earthquake (Google Earth 2014).

Figure 3.2. Lateral spread toward Avon River in Christchurch, NZ (Cubrinovski et al. 2011).

3.3 IMAGE SELECTION AND PROCESSING

Given the severity of liquefaction induced horizontal displacements and availability of satellite imagery, an area encompassing the neighborhoods along the Avon River to the east of the CBD was selected for study. The area of study is outlined in red in Figure 3.1. The near surface soils in this area consist of fine sands and silty sands deposited by fluvial processes, and the upper 5-6 m of soil is very loose. Additionally, the water table is approximately 1 m below the surface (Cubrinovski et al. 2011).

Pre- and post-earthquake images from the 2011 Christchurch earthquake were selected based on their similar acquisition angles and 0.5 meter pixel resolution. These panchromatic (i.e., gray-scale) images were collected by the WorldView-1 (pre-event) and GeoEye-1 (post-event) satellites. The pre- and post-earthquake images were acquired on September 21, 2010 and February 26, 2011, respectively, with off-nadir

angles of 19.8° and 18.2° and target azimuths of 55.1° and 51.1°, respectively. Importantly, the pre-event image was acquired after the September 3, 2010 Darfield earthquake. Figure 3.3 shows the pre-event image with the location of neighborhoods indicated that will be discussed in detail later.

By using equations 2.1, 2.2, and 2.3 and assuming a pseudo-suborbital path of 0° (i.e. $\theta_0 = 0$), north/south look angles (T) of 11.64° and 11.67° and east/west look angles (S) of 16.45° and 14.35° can be established for both the pre- and post-event image, respectively. The difference in the north/south look angles is 0.03°, and the difference in the east/west look angles is 2.10°. These differences in acquisition angles are small enough that there should not be noticeable displacement signatures associated with DEM errors, etc.

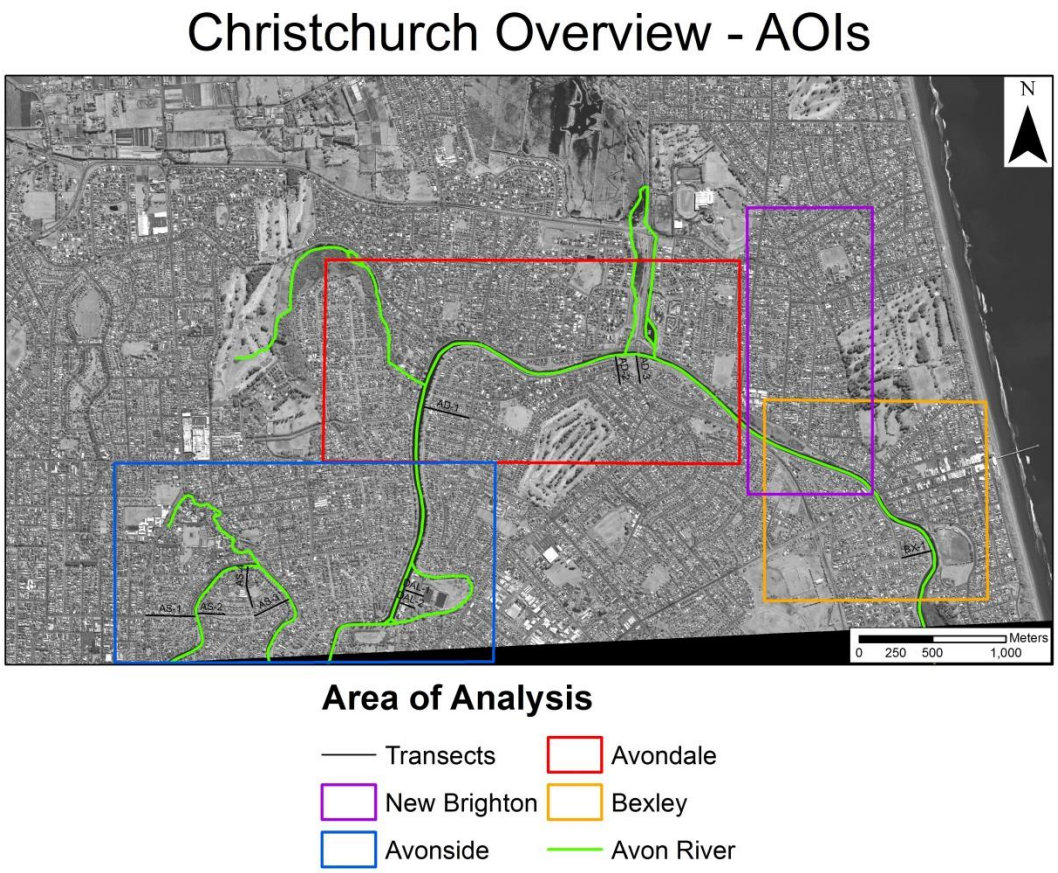

Figure 3.3. Pre-event (Sept. 21, 2010) satellite image and neighborhoods of interest.

The two images were orthorectified using open source software GDAL (Geospatial Data Abstraction Library, GDAL 2012) and a digital elevation model (DEM) of 90 m resolution from the Shuttle Radar Topography Mission (SRTM, USGS 2004). Next, tie points were generated for co-registration using the software ENVI (ENvironment for Visualizing Images, ENVI 2014). ENVI generates tie points automatically using normalized cross correlation to identify corresponding locations in the two images (EXELIS 2013). Tie points identified within 300 m of the river were discarded because lateral spreading movements were expected within this zone and

therefore these locations should not be tied between the two images. Additionally, tie points with large residuals relative to the warping polynomial were removed because (1) large residuals potentially indicate false-positive tie points (i.e., the areas identified in the two images are not the same) and (2) the first order polynomial should not correct for localized differences in the images. Figure 3.4 shows all the tie-points generated from ENVI's automatic tie point generation tool overlaid with correlation results (performed later) near the Avondale neighborhood. Points which were discarded are displayed as red x's, while selected tie points are represented with colored circles. Note that most tie-points near areas of large displacement were discarded and the few remaining tie-points in these have higher residuals because the warping polynomial does not account for localized deformation. This observation validates the use of tie point residuals as selection criteria. Ultimately, a density of 47 tie points per square kilometer was obtained, and 1,700 well-distributed tie points were used in the co-registration. The resulting RMSE across the image was 0.30 m. Figure 3.5 shows the tie points selected for post-event image warping with the residual of each tie-point represented by its color.

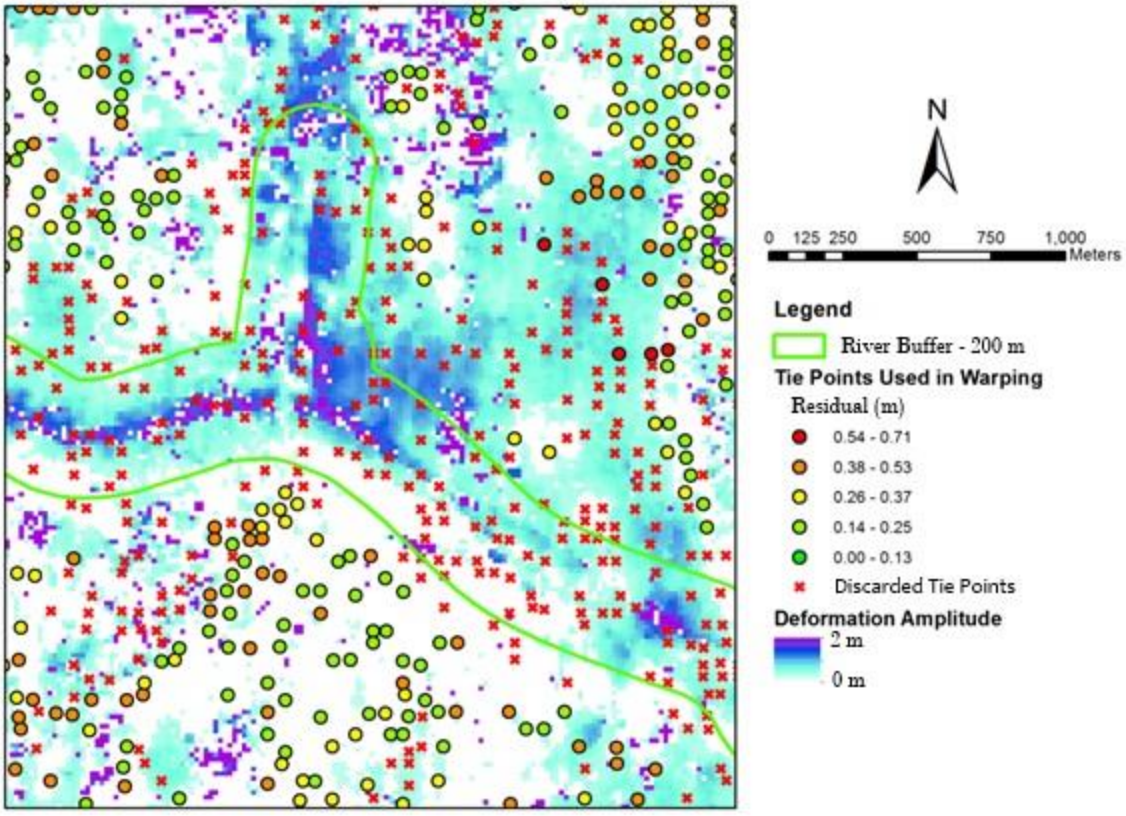

Figure 3.4. Tie point locations compared with deformation results.

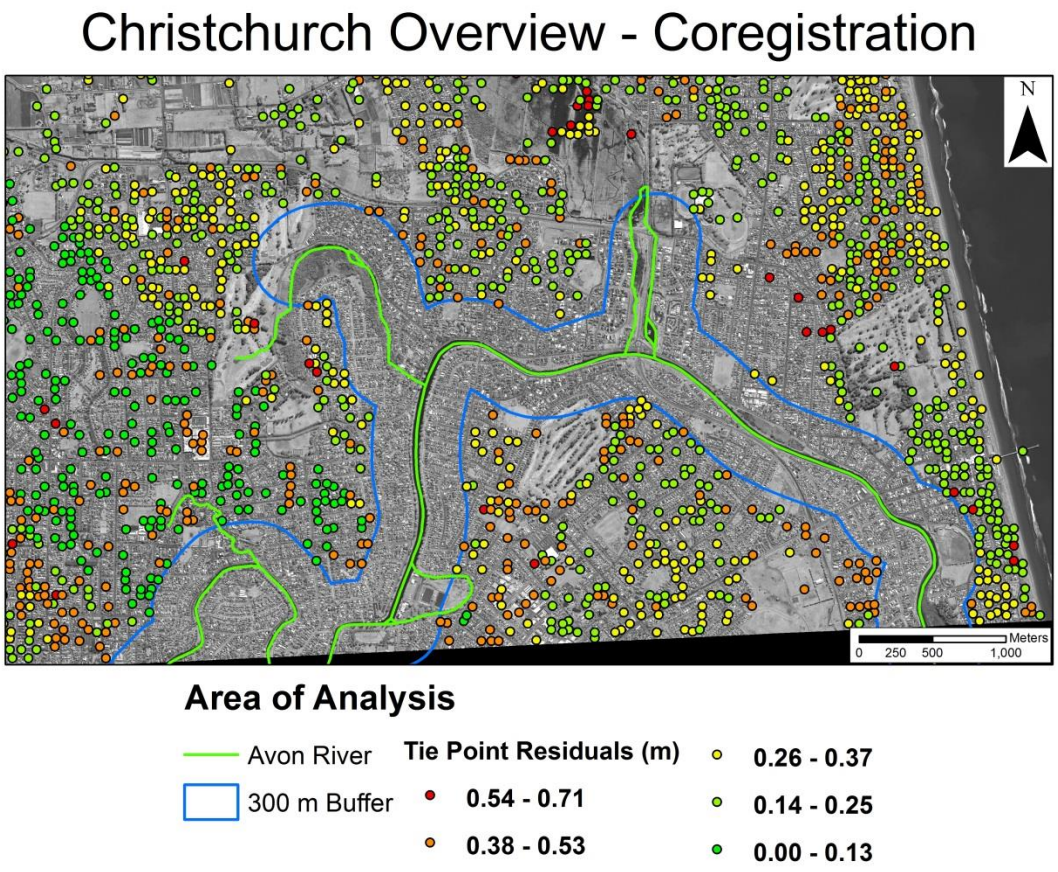

Figure 3.5. Tie points selected for post-event image warping.

After co-registration, optical image correlation was performed using the program COSI-Corr (Leprince et al. 2007). A chip window of 128 by 128 pixels (64 m) was used with a step size of 32 pixels, which produced a displacement estimate every 16 m. Results with an SNR less than 0.95 were removed as "decorrelated" pixels. A precision displacement threshold of 0.30 m was established that represents the potential variation between the measured and actual displacement, as well as the smallest displacement that can be confidently distinguished from zero. The precision threshold value of 0.30 m was determined from the co-registration RMSE of 0.30 m, which dominates other sources of error, as discussed in Section 2.2.4. This threshold can also be estimated by examining

measured displacements in non-moving areas (e.g. Debella-Gilo and Kääb 2012). Non-moving areas are areas where displacements measurements should be zero. Therefore, areas where coherent patterns of deformation are detectable or where correlation techniques are not expected to work (e.g. in bodies of water or in a large grass field) are excluded from statistical analysis of non-moving areas. Figure 3.6 shows frequency-distribution histograms of (a) north/south and (b) east/west displacements in non-moving areas from correlation analysis (results presented later). Each bin width is 0.02 m, and the center value of each bin is shown on the x-axis. The histogram of the north/south displacements indicates the mean displacement is close to zero (0.013 m) and 68% of the correlation measurements are within ± 0.164 m of the mean. Similarly, the histogram of the east/west displacements indicates the mean displacement is nearly zero (0.037 m) with 68% of the measurements occurring within ± 0.229 m of the mean. Taking the square-root of the sum of the squares of these standard deviation values results in a value of 0.28 m. Thus, the statistics of the correlated displacements in non-moving areas confirm that the threshold, or precision, of the displacement measurements is about 0.30 m.

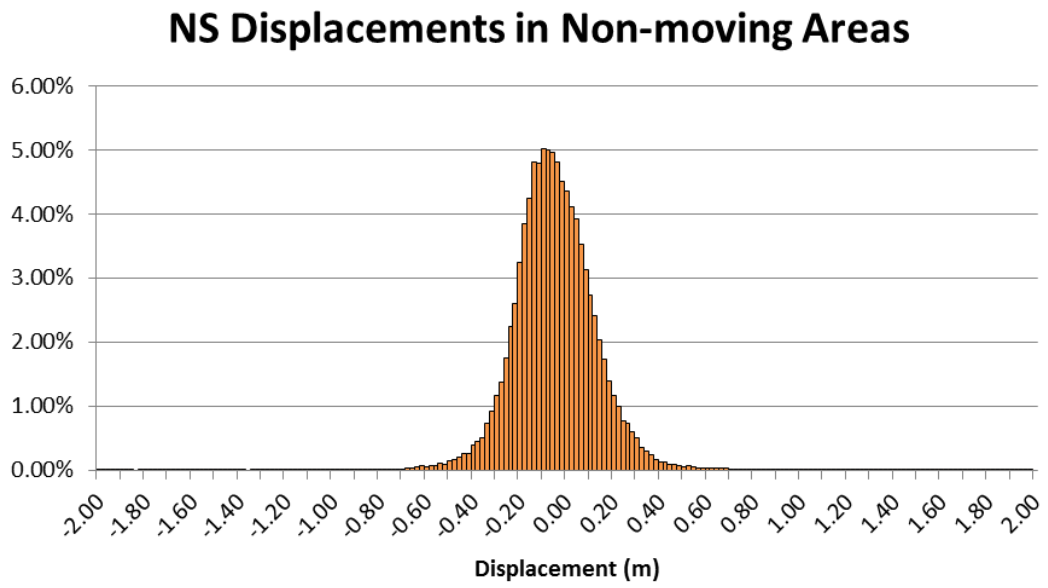

(a)

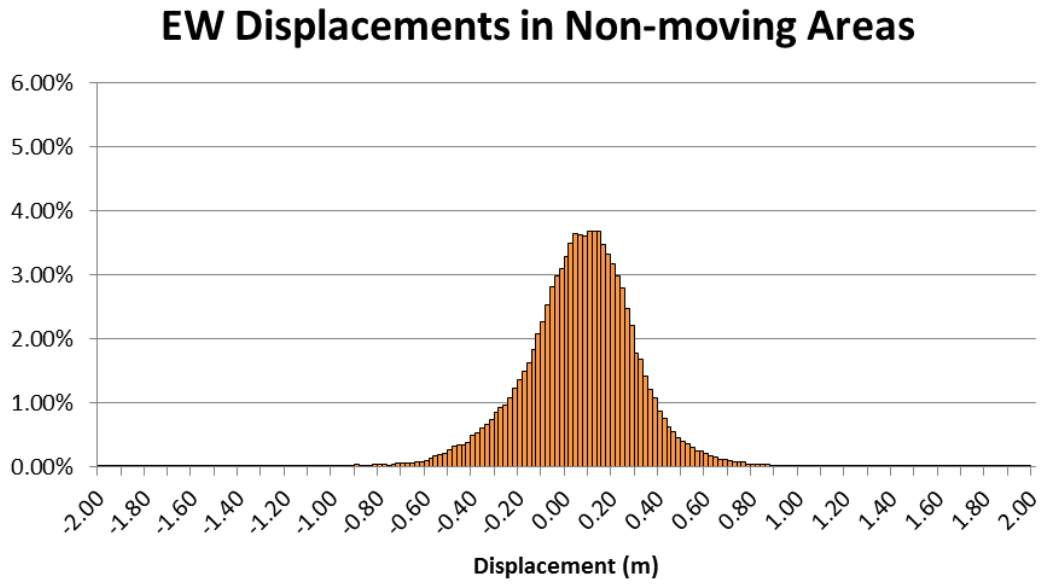

(b)

Figure 3.6. Histogram of (a) north/south and (b) east west displacements in non-moving areas.

3.4 DEFORMATION RESULTS

Displacements were measured in the north-south and east-west directions using optical image correlation. Figure 3.7 shows the amplitudes of the north-south displacements across the study area. Displacements less than the precision threshold were set to zero for visual purposes. Movements towards the north are shown in red/yellow, and movements towards the south are shown in blue/purple. Coherent zones of deformation are concentrated along the river with most displacement occurring within 150 m of the river. However, the lateral spread in the New Brighton area (purple box) extends further than 500 m from the river and would be difficult to define using traditional measurement techniques. North-south movements are largest in areas where the river runs directly east-west due to spreading towards the river. As expected, areas north of the river displace southward, while areas south of the river displace northward. This change in displacement direction from north to south at the river indicates that the deformations are associated with lateral spreading towards the river. The largest north/south displacements are on the order of 2 m or more (red areas).

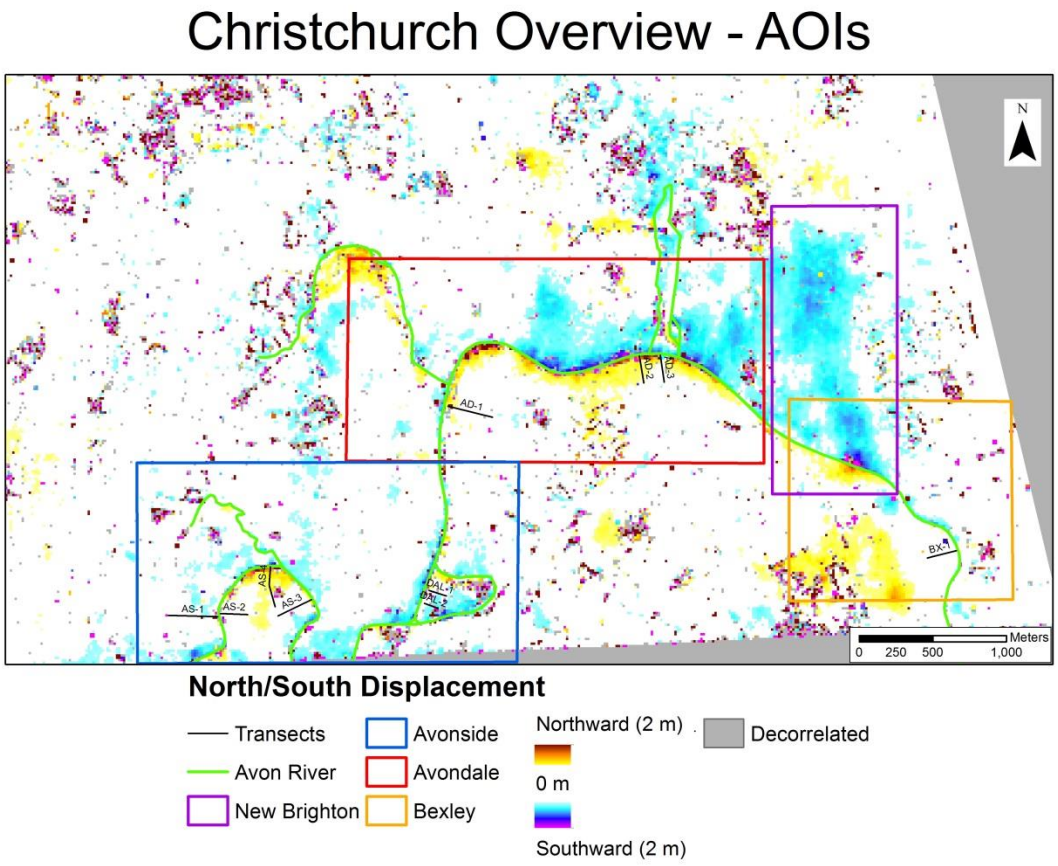

Figure 3.7. Overview of north/south displacements from correlation results

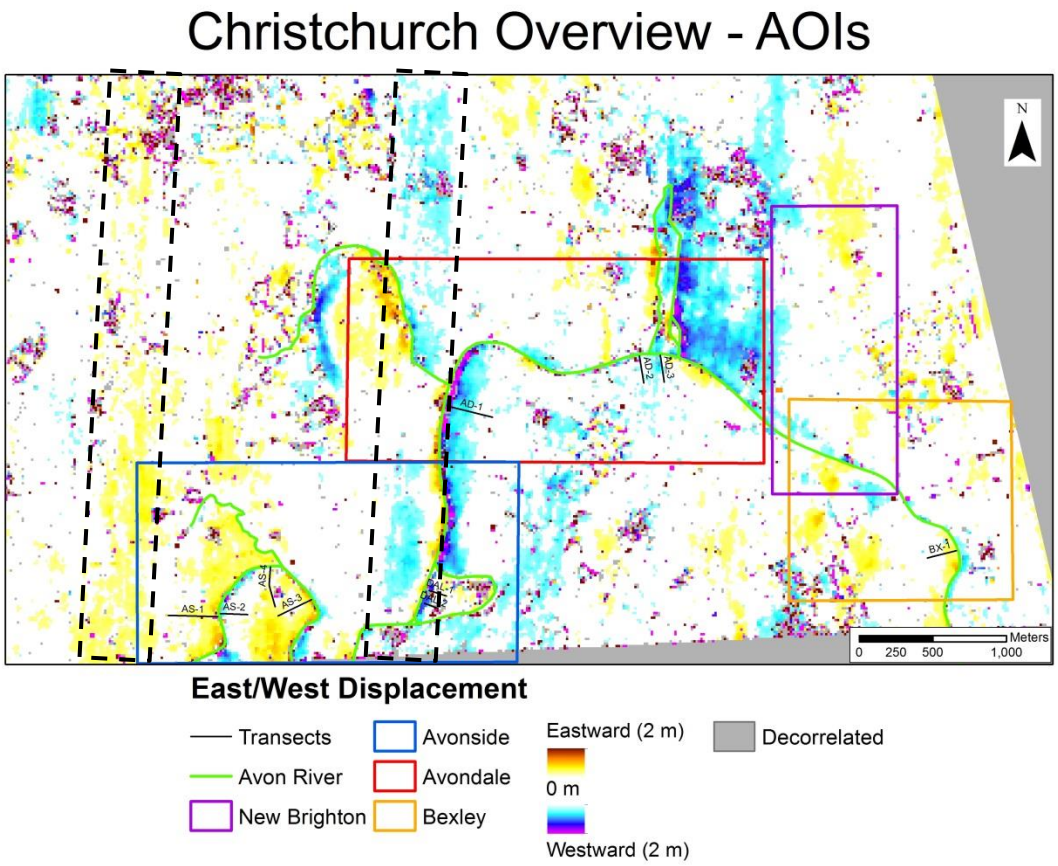

Figure 3.8. Overview of east/west displacements from correlation results.

Deformations in the east-west direction are shown in Figure 3.8 with red/yellow used for the eastward displacements and blue/purple for the westward displacements. Displacements less than the precision threshold were set to zero for visual purposes. Areas to the west of the river displaced predominantly eastward, and areas to the east of the river moved predominately westward, indicating lateral spreading towards the river. The largest displacements occur immediately adjacent to the river. There are significant lengths of the river that experienced 2 m or more of displacement (red and purple areas). These large east/west displacements are focused predominantly where the Avon River

runs north/south in the eastern parts of Avonside and in the eastern parts of Avondale where the river splits.

Two areas outlined by the dashed lines display unexpected displacement patterns. These areas show strips of displacement that are independent from the river location. The distinct linear patterns of the displacement are likely banding artifacts from misalignment in the image acquisition. Pushbroom sensors on the satellites (including Worldview-1) use a linear array of detectors to collect image data (Krause 2008), and the data collected from each detector must be aligned to produce the full image. If the data are slightly misaligned, linear artifacts may be present in the correlation results as seen in the east/west displacements. While some of these artifacts were removed in the co-registration, not all were removed.

Comparisons of the measured displacement with geology, as well as with qualitative and quantitative measurements of displacements from other sources are discussed in the next sections. The results are examined for the four areas of interest identified in Figure 3.7 and Figure 3.8 so that detailed deformation patterns may be discussed more easily.

3.4.1 Geology

An overview of the geology in the region of analysis from Brown and Weeber (1992) is shown in Figure 3.9 with the outlines of the four previously defined areas of interest. The blue-tinted areas indicate marine deposits, and the tan areas represent alluvial deposits. The marine soils may contain clay and peat, so liquefaction (and thus liquefaction induced deformation) is less likely in these areas. The alluvial soils are primarily sands with no indication of significant fines content. Therefore, liquefaction

induced deformation can be expected in the alluvial soils. Soils near the Avon River are predominantly alluvial sandy soils with some intrusions of marine-deposited dirty sands. The map shows that marine soils are found along some segments of the Avon River with sandy alluvial deposits located further from the river in these areas (e.g., Bexley area); this indicates that the location of the Avon River has shifted leaving sandy alluvial deposits to the west of the current river location in Bexley.

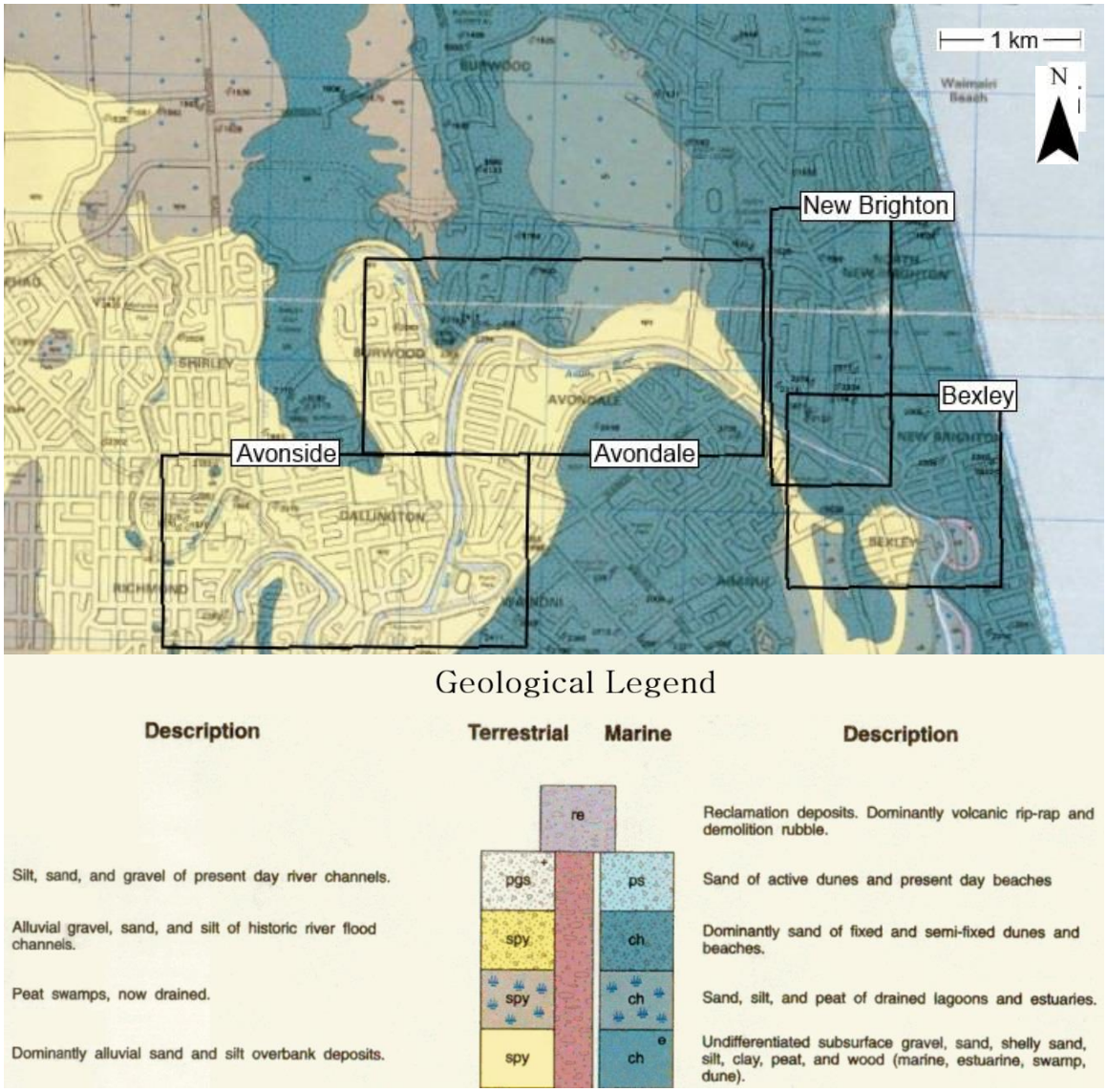

Figure 3.9. Christchurch near surface geology (Brown and Weeber 1992).

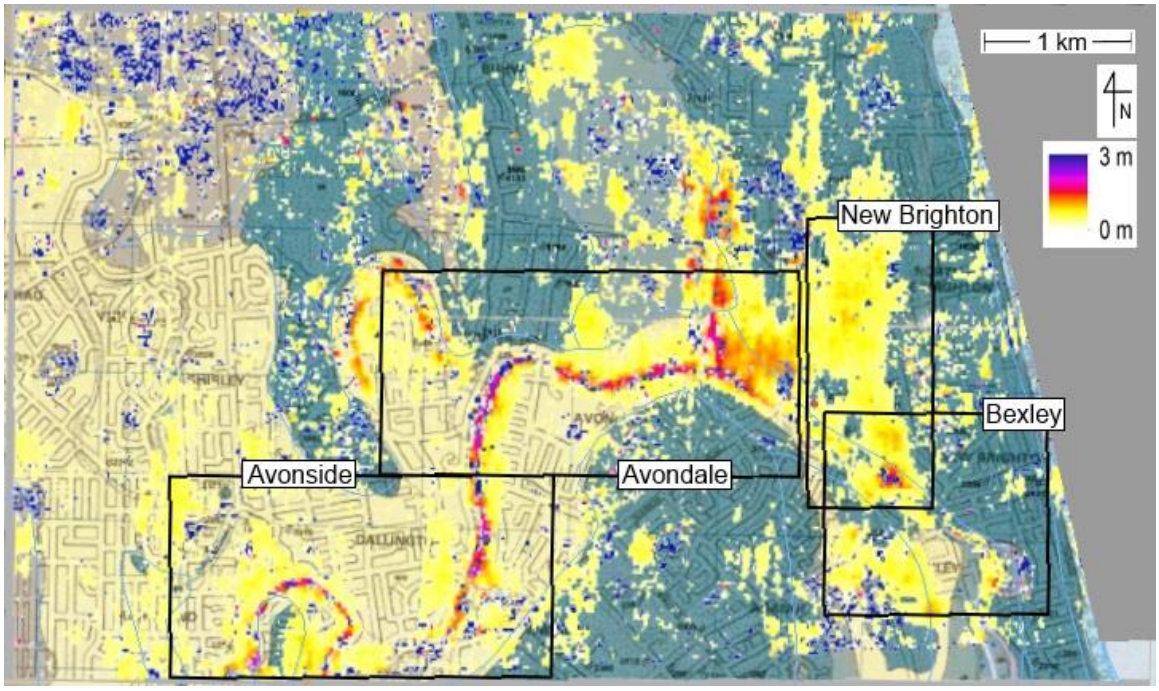

Figure 3.10. Measured displacement amplitudes superimposed on map of near surface geology. Geology map from Brown and Weeber (1992).

Figure 3.10 shows the displacement amplitudes from the correlation analysis superimposed onto the near surface geologic map. The displacement amplitudes were derived from the square root of the sum of the squares of the north/south and east/west displacements, and displacements less than the precision threshold are not shown for visual purposes. In most areas the deformation is restricted to areas of sandy alluvium and is bounded by marine deposits that contain fines. For example, near the river bend near the northwest corner of the Avondale area, liquefaction induced deformation is clear on the south side of the river where sandy alluvium prevails, but little to no deformation is seen north of the bend where marine deposits are located. However, some deformation can be seen in the marine deposits, specifically near the east side of Avondale and within the New Brighton area.

Figure 3.11 shows the near surface geology and displacement amplitudes in the Avonside area in greater detail. Again, displacements less than the precision threshold were set to zero for visual purposes. Deformations are contained within the sandy alluvium and are well bounded by the marine deposits. Specifically, notice the marine intrusion in the southwestern region of Avonside. Both north/south and east/west displacements are measured in the sandy alluvium directly east of the intrusion, but immediately dissipate within the intrusion.

(a)

(b)

(c)

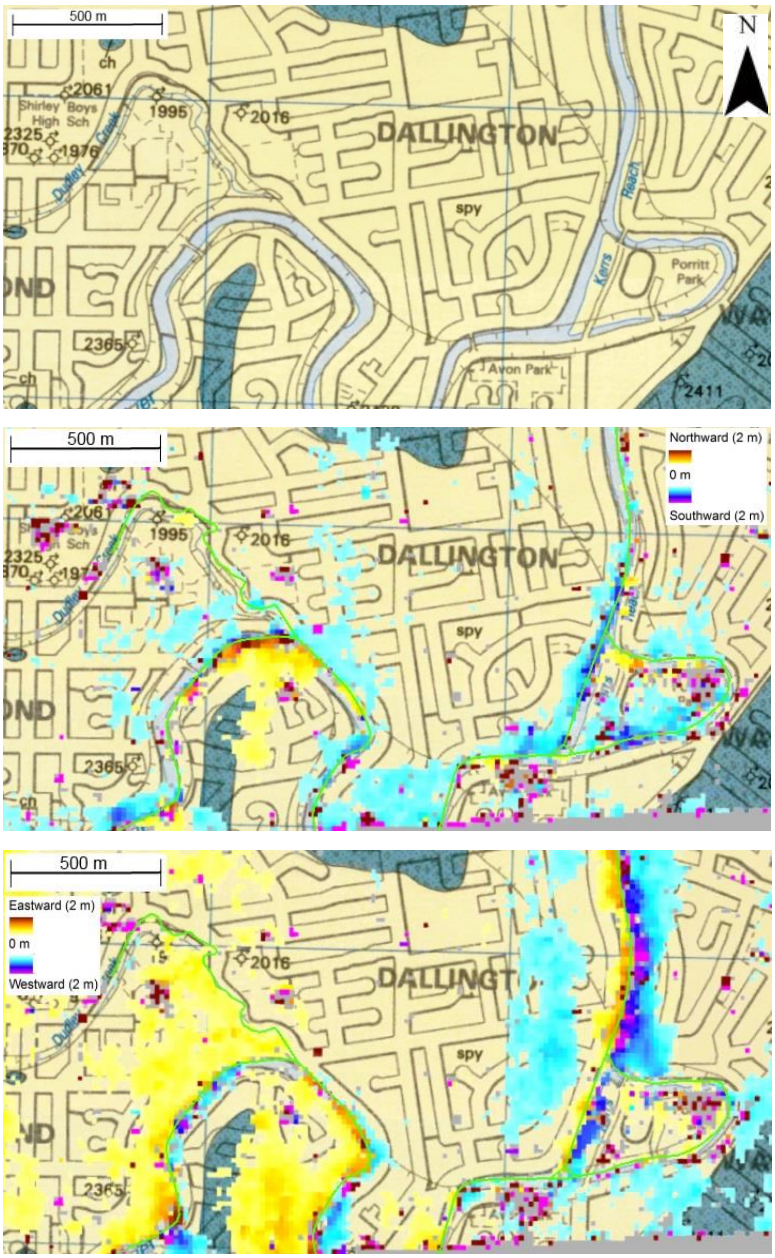

Figure 3.11. (a) Near-surface geology, (b) north/south displacements, and (c) east/west displacements in Avonside area (Brown and Weeber 1992).

(a)

(b)

(c)

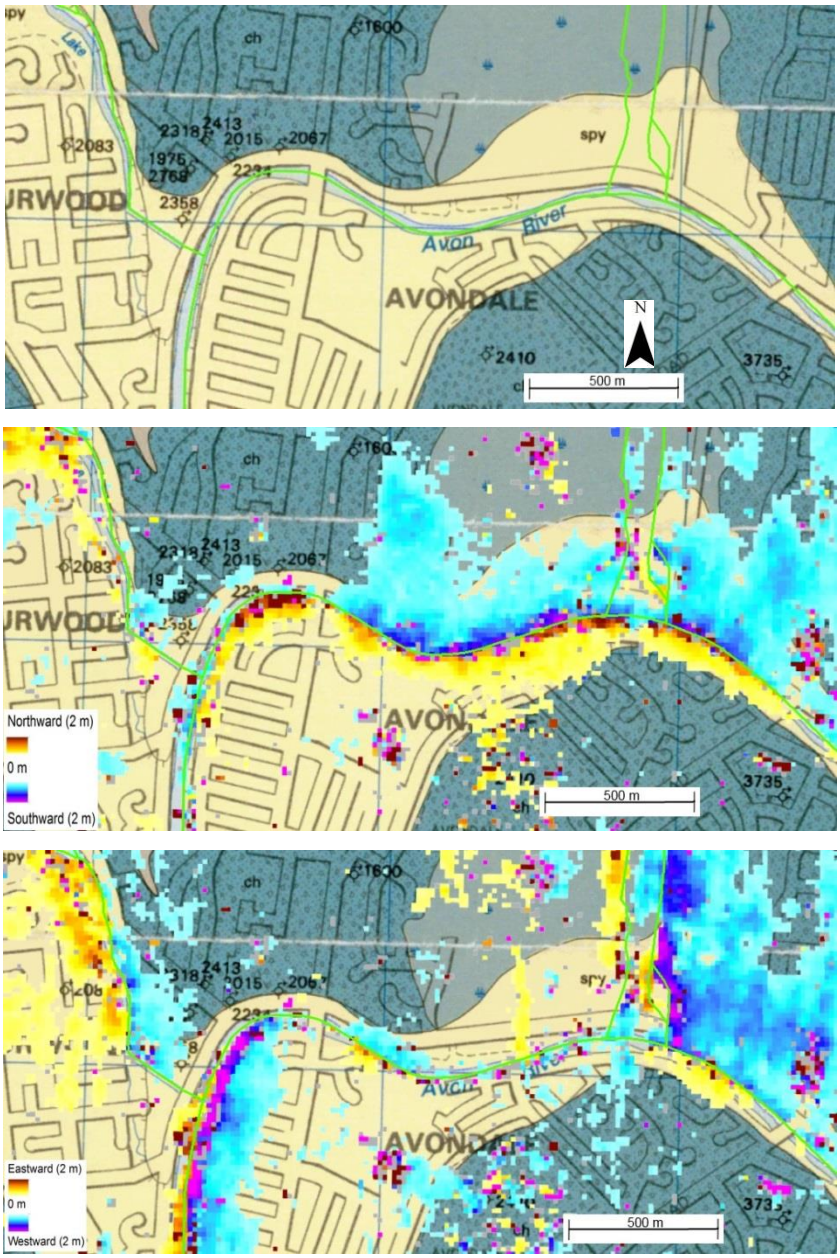

Figure 3.12. (a) Near-surface geology, (b) north/south displacements, and (c) east/west displacements in Avondale area (Brown and Weeber 1992).

Figure 3.12 shows the near surface geology and measured displacements greater than the precision threshold in the Avondale area. Again, lateral displacements are

concentrated within the sandy alluvium and deformation is bounded by the marine deposits. Lateral spread movements extend further from the river where the alluvial deposits extend further from the river. For example, in the eastern part of Avondale near the vertical split of the river, lateral spread movements north of the river extend 200-400 m before termination, but movements only extend 50-200 m on the south side of the river where marine deposits are closer to the river. Although most deformation occurs within the sandy alluvium, some coherent deformation patterns are observed in the marine deposits. North of the river in the center and eastern edge of the Avondale area, displacements extend far into the marine deposits. Further research into the geotechnical characteristics of the subsurface soils in these areas will be required to understand the source of these deformations.

Figure 3.13 compares the near surface geology and measured deformations in the New Brighton area. Here, there is little to no sandy alluvium, but a coherent lateral spread pattern which extends over a kilometer north of the river is present. Again, further investigation into the subsurface characteristics is required to understand the source of this deformation.

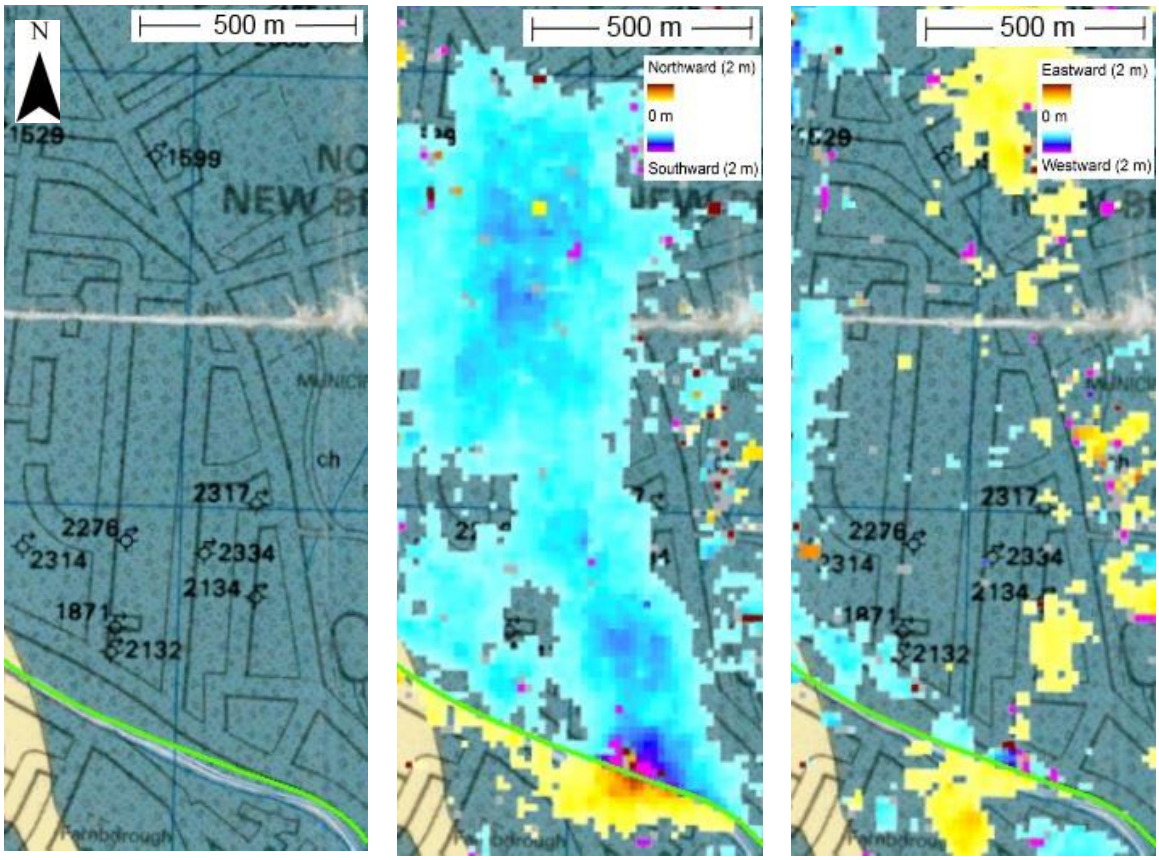

(a) (b) (c)

Figure 3.13. (a) Near-surface geology, (b) north/south displacements, and (c) east/west displacements in New Brighton area (Brown and Weeber 1992).

Figure 3.14 presents the correlation displacement results superimposed on the geologic map in the Bexley area. The large lateral spread along the northern part of the river occurs within the marine deposits, but the remaining deformation patterns are concentrated in the alluvial sandy soils. Deformation in the former path of the Avon River west of its current location is easily detected in the correlation results.

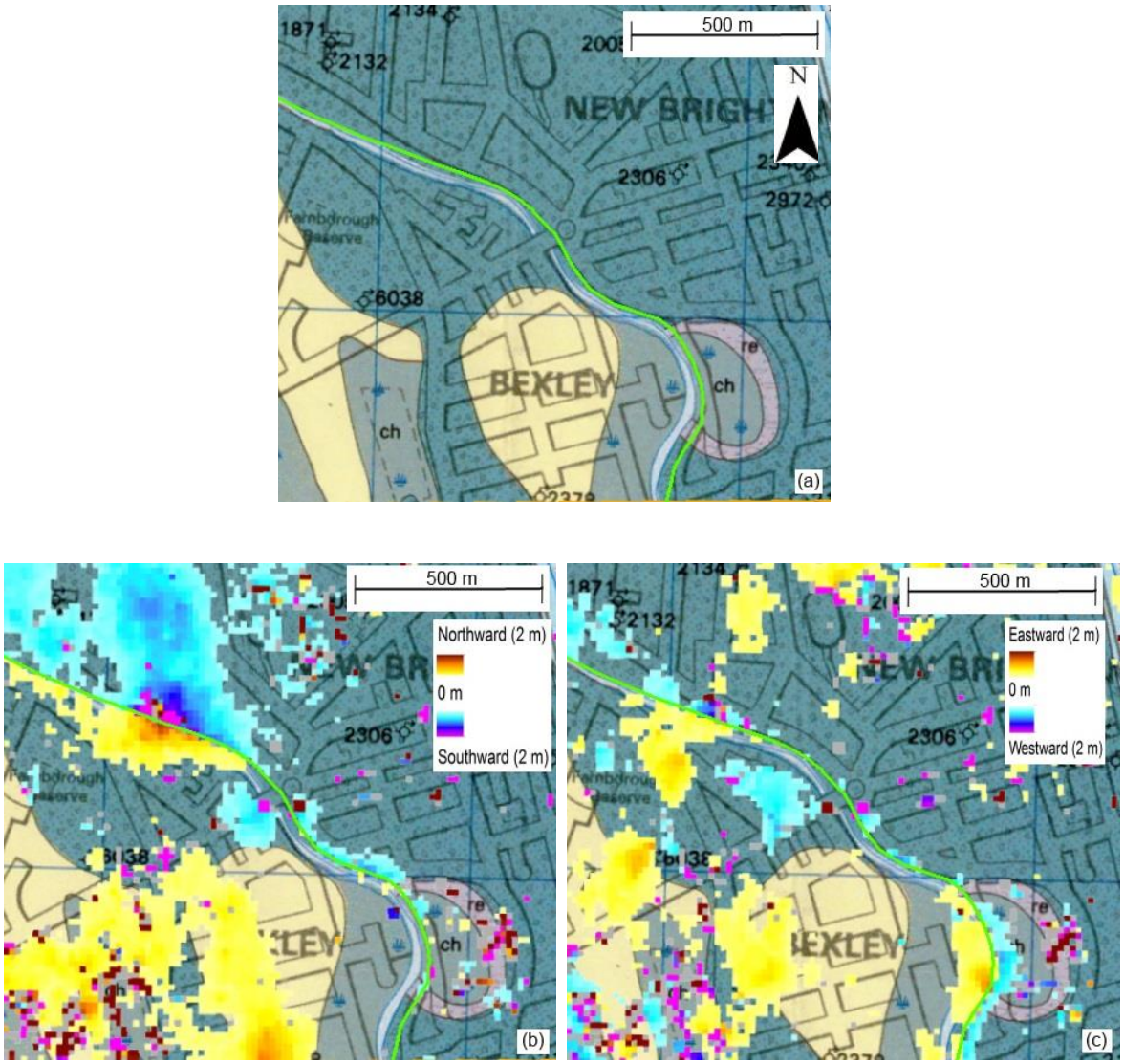

Figure 3.14. (a) Near-surface geology, (b) north/south displacements, and (c) east/west displacements in Bexley area (Brown and Weeber 1992).

3.4.2 Qualitative Lateral Spreading Observations

Ground observations of liquefaction and lateral spreading were collected in residential areas across Christchurch (Canterbury Geotechnical Database 2013). Observations were organized into three categories: (1) no liquefaction, (2) liquefaction, and (3) liquefaction and lateral spreading. These three categories were subdivided based

on severity. A diagram illustrating these categories is shown in Figure 3.15. These observations only account for liquefaction with visible evidence at the surface. Not all properties were assessed before an aftershock occurred in June 2011, so the observations are somewhat incomplete. Also, it is possible that observations made after the February 2011 earthquake may include damage from the September 2010 Darfield Earthquake. Despite these uncertainties, the observations provide the best qualitative assessment of the severity of liquefaction across Christchurch for comparison to correlation results.

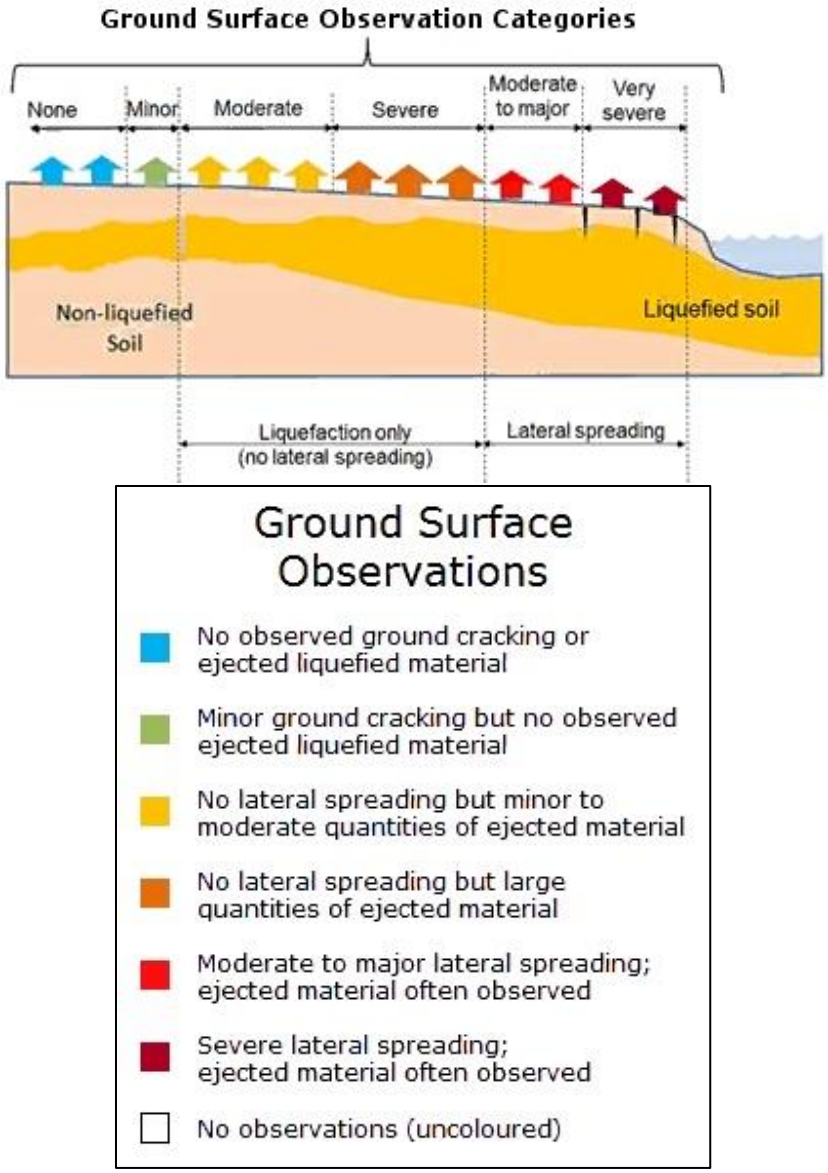

Figure 3.15. Explanation of observation categories (Canterbury Geotechnical Database 2013).

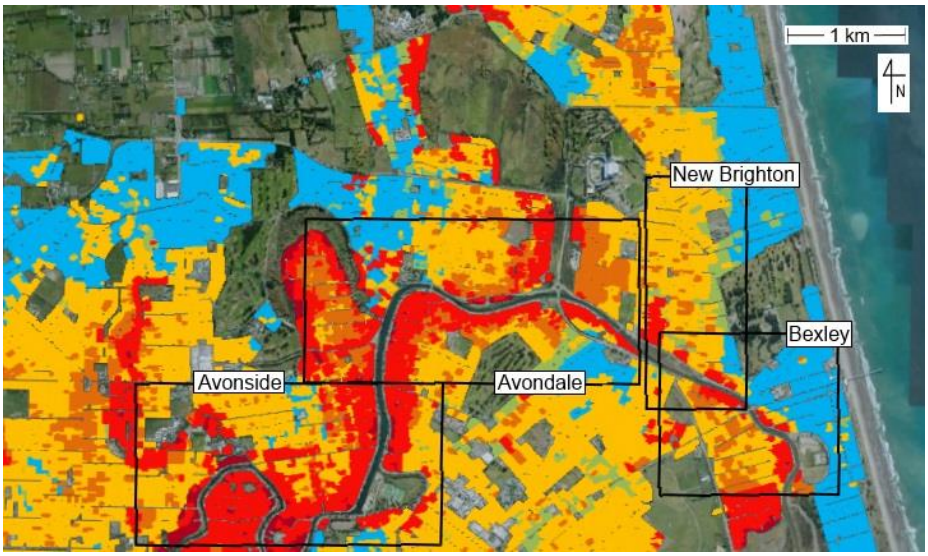

(a)

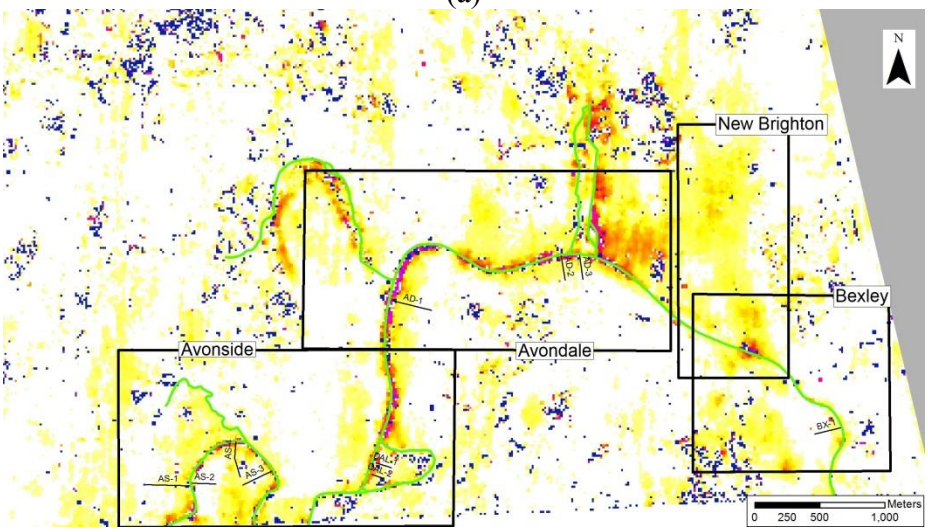

(b)

Figure 3.16. (a) Map of observed liquefaction and lateral spreading (Canterbury Geotechnical Database 2013) and (b) amplitude of displacements from correlation results.

The liquefaction observation map for the area of correlation analysis is shown in Figure 3.16(a) with the four areas of interest identified. The most severe lateral spreading is observed adjacent to the Avon River. Nothing beyond 100-200 m from waterways is mapped as lateral spreading, but large amounts of ejected material are observed further

from the river. Figure 3.16(b) shows the amplitudes of displacement measurements from the correlation analysis. Displacements less than the precision threshold were set to zero for visual purposes. Amplitudes are calculated by taking the square root of the sum of the squares of the north/south and east/west displacements (i.e. $\sqrt{(N/S\ disp)^2 + (E/W\ disp)^2}$). The largest displacement amplitudes are represented by purple/blue and are in excess of 3 m.

Figure 3.17 compares the observed liquefaction with the displacement amplitudes from the correlation analysis (bottom). Areas of severe lateral spreading (dark red) match with areas of large displacement from the correlation analysis. Most areas where moderate to major lateral spreading were observed correspond to moderate to large displacements. However, the correlation analysis shows some areas of little to no deformation where moderate to major lateral spreading was reported on the observation map. For example, in the area outlined with the dashed circle, little to no deformation is measured in the correlation analysis immediately east of the river; however, the observation map indicates moderate to major lateral spreading. In areas where neither lateral spreading nor large amounts of ejected material were observed, the correlation results show little to no displacement.

(a)

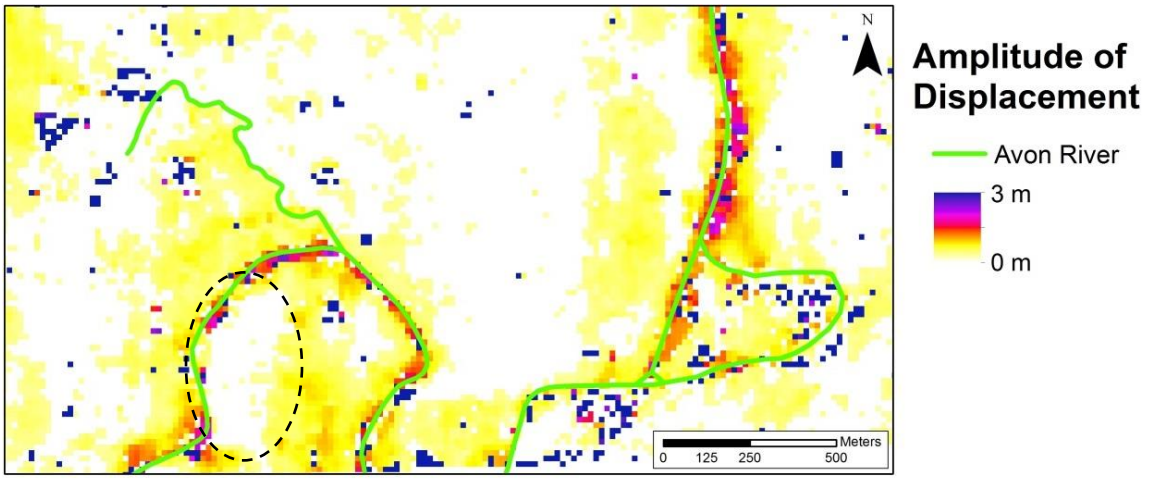

(b)

Figure 3.17. (a) Observations of liquefaction inducded deformation (Canterbury Geotechnical Database 2013) and (b) amplitude of displacement measurements in the Avonside area.

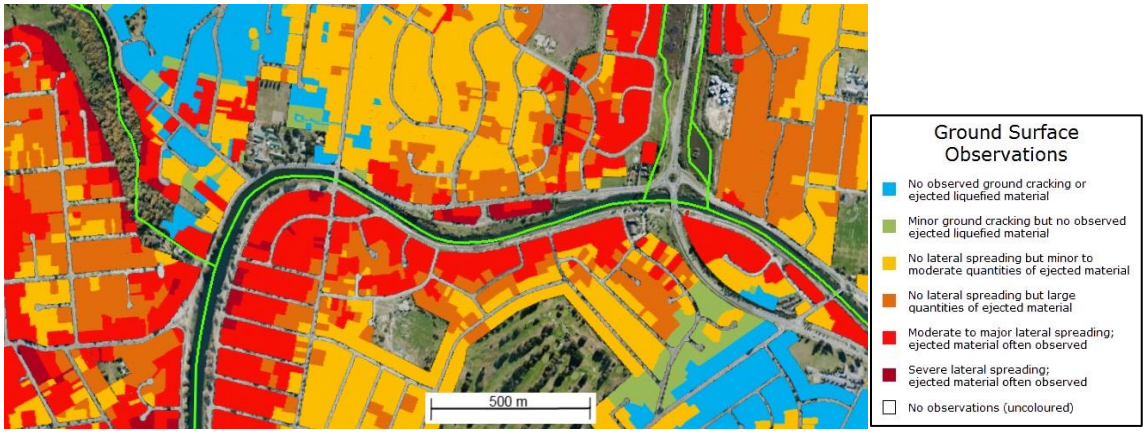

(a)

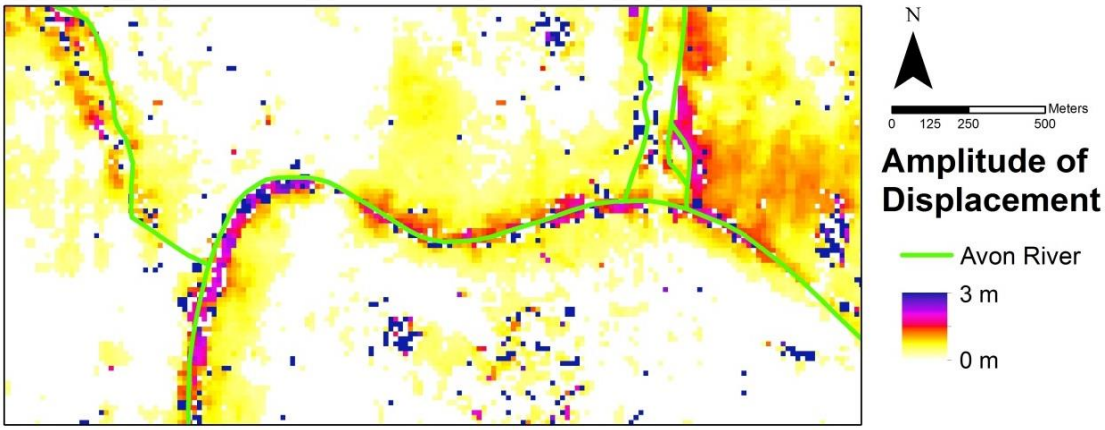

(b)

Figure 3.18. (a) Observations of liquefaction inducded deformation (Canterbury Geotechnical Database 2013) and (b) amplitude of displacement measurements in the Avondale area.

The liquefaction observation map and displacement amplitudes from the correlation analysis for the Avondale area are presented in Figure 3.18. The magnitude and extent of displacements match the severity and extent of observations south of the Avon River. However, displacements north of the river in the center of the image and displacements in the northeast of the area shown do not match ground observations. In these areas, the correlation analysis reveals significant lateral deformation which extends

further than 200 m from the riverbank, but ground observations record only large amounts of ejected material and no lateral spread deformation 100 m from the river. However, it is possible that any lateral displacement in this area was hidden by the significant ejecta and thus not observed or noted by the field mapping.

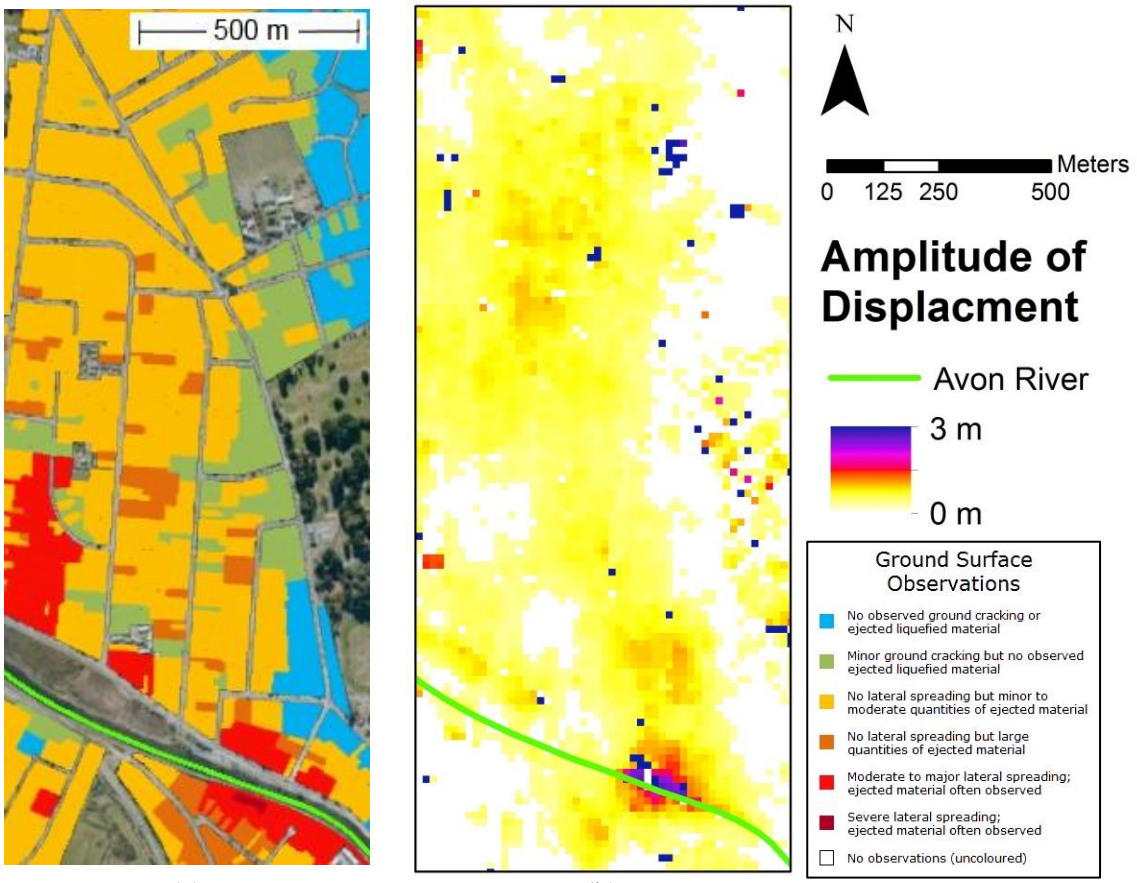

(a) (b)

Figure 3.19. (a) Observations of liquefaction inducded deformation (Canterbury Geotechnical Database 2013) and (b) amplitude of displacement measurements in the New Brighton area.

Figure 3.19 shows the liquefaction observations with the displacement measurements from correlation analysis in the New Brighton area. Both ground

observations and the correlation results show lateral spreading adjacent to the southeastern part of the river in this area. The ground observations indicate lateral spreading terminates within 100 m of the Avon River. The correlation results south of the river agree with the ground observations on the extent of the lateral spread, but the correlation results indicate the lateral spreading north of the river extends well beyond 100 m. In the center and northern parts of the New Brighton area, the correlation results show widespread deformation of about 1 m. The ground observations note large amounts of ejected material in these areas, but lateral spreading was not reported. However, as discussed for the Avondale area, it is possible that significant ejecta masked any evidence of lateral spreading.

Ground liquefaction observations and correlation displacement results in the Bexley area are presented in Figure 3.20. Ground observations show lateral spreading and ejected material predominately west of the Avon River. Little to no lateral spreading and ejected material are indicated east of the river. The correlation results agree well with these ground observations. East of the river, the correlation results reveal no lateral deformation, but significant deformation was measured on the western banks of the Avon River.

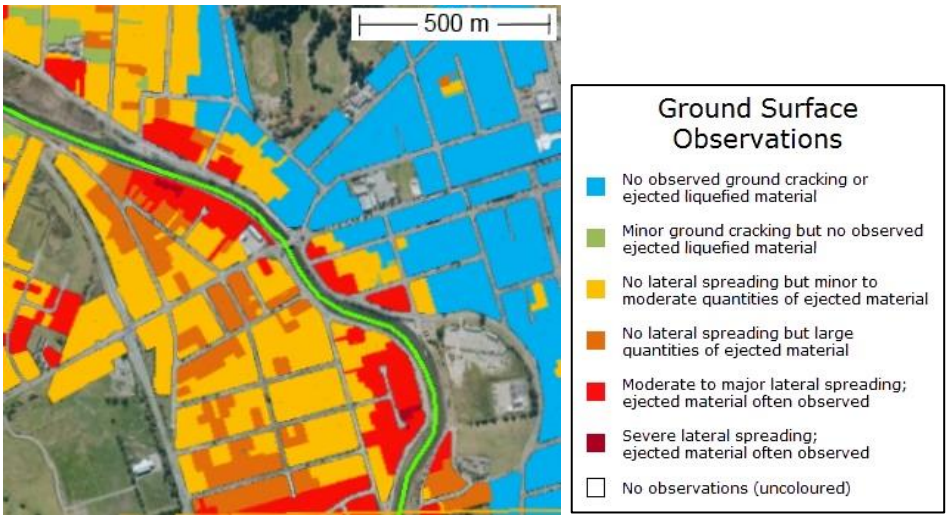

(a)

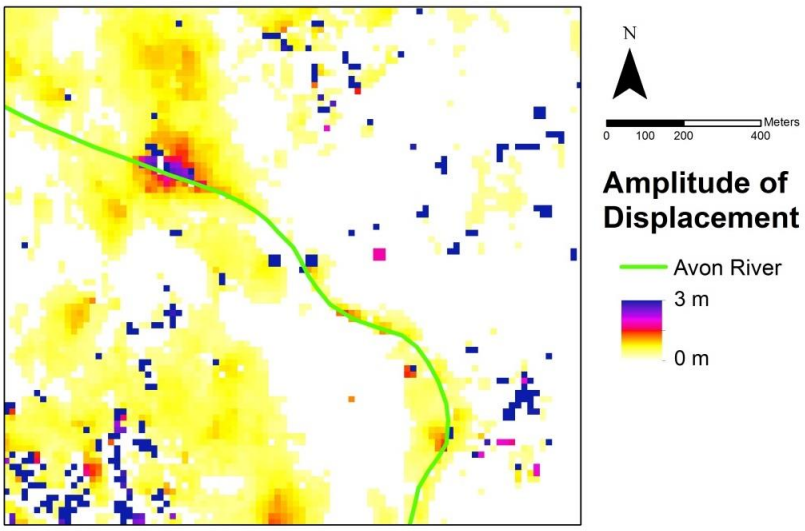

(b)

Figure 3.20. (a) Observations of liquefaction inducded deformation (Canterbury Geotechnical Database 2013) and (b) amplitude of displacement measurements in the Bexley area.

Based on the comparisons shown, the qualitative ground observations agree with the correlation results. Areas where ground observations indicate lateral spreading

correspond with lateral deformation measured from the correlation analysis. In areas where there is disagreement, the significant ejects may have masked evidence of lateral spreading, and thus it was not reported in the field observation map. The correlation analysis was not as significantly influenced by the ejecta because of the presence of buildings upon which to correlate, and thus the correlation analysis could identify displacements in these areas.

3.4.3 Measurement of Cracks Associated with Lateral Spreading

For two weeks following the February 2011 Christchurch Earthquake, cracks associated with lateral spreading were mapped to identify the general direction, magnitude, and extent of lateral spreading (Canterbury Geotechnical Database 2012b). Ground observations of cracks were cataloged by marking the locations of cracks on printed aerial photography using color pens, whose color represented categories of crack widths. These markings were manually digitized to create a database of cracks. Nonetheless, the crack mapping is incomplete, and many cracks on roads were not able to be identified before they were repaired. Mapped cracks will be qualitatively compared with the correlation results in each of the four areas previously identified. Displacements less than the precision threshold were set to zero for visual purposes. Cracks whose widths measured less than 50 mm were excluded from comparison for visual clarity.

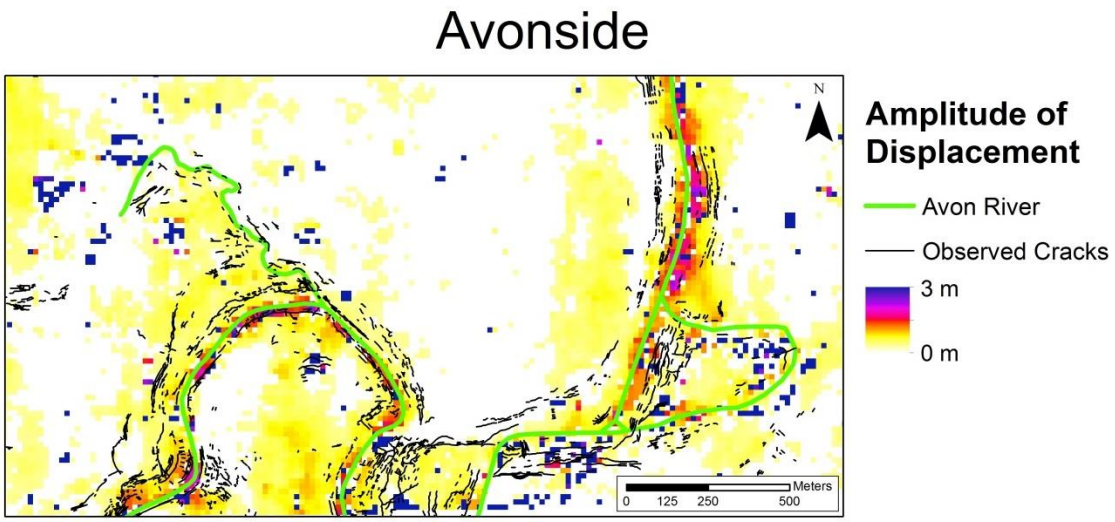

Figure 3.21. Observed cracks superimposed on map of the measured displacement amplitudes in Avonside. Cracks with recorded widths less than 50 mm were excluded for visual clarity (Canterbury Geotechnical Database 2012b).

Figure 3.21 shows observed crack locations superimposed on the amplitudes of measured displacements from the correlation analysis in the Avonside area. Cracks run parallel to the waterways indicating displacements toward the river. The concentration of cracking is consistent with areas of larger displacement from the correlation analysis; i.e., areas of larger displacement correspond with areas of wide and dense cracking. Additionally, displacements approach zero where cracking stops.

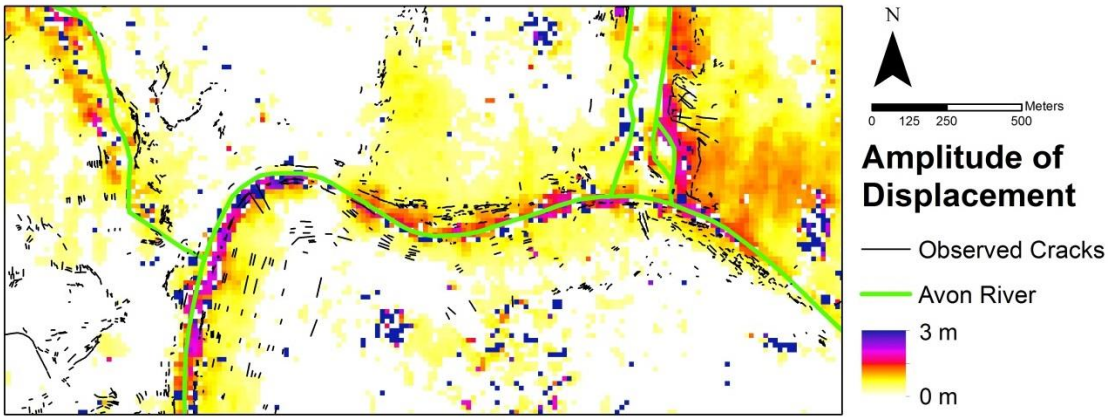

Figure 3.22. Observed cracks superimposed on map of the measured displacement amplitudes in Avondale. Cracks with recorded widths less than 50 mm were excluded for visual clarity (Canterbury Geotechnical Database 2012b).

Crack locations and correlation results in the Avondale area are presented in Figure 3.22. Cracks are predominately oriented parallel to the river indicating lateral spreading toward the river. Measured displacements south of the river are bounded well by the observed cracks, and areas of large displacement are bounded by cracks north of the river. However, as noted in the previous section, lateral spreading generally extends further north of the river than indicated in the map of ground observations of lateral spreading. The observed cracks running parallel to the river in this area bound the largest displacement within 100 m of the river, but observed cracks farther north bound the west side of the zone of deformation indicated by the correlation analysis. Cracks in the northeastern part of the image bound the largest measured displacements, but the full extent is not bound by observed cracks. Again, this may be due to the significant ejecta masking any ground cracks.

Observed cracks and correlation results for the New Brighton area are shown in Figure 3.23. As in the Avondale area, the area of largest displacement is bounded by the observed cracks. However, the full extent of lateral spreading north of the river with displacements of about 0.5 to 1 m is not confirmed from crack observations. The lack of crack observations north of the river may be due to the incompleteness of the database or the effects of ejecta. Additionally, it is possible that this level of deformation did not cause cracking.

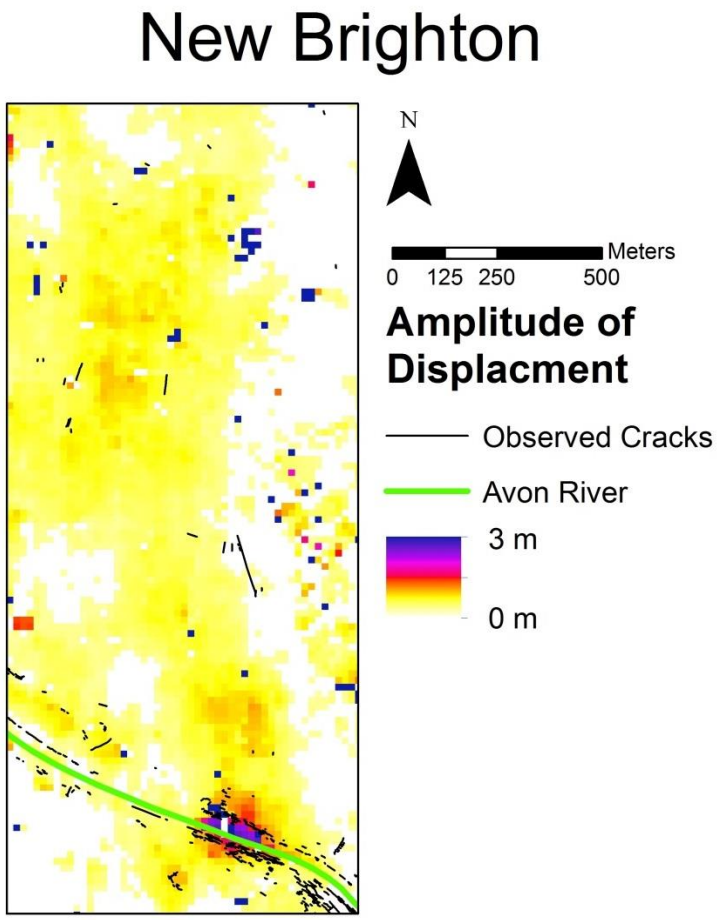

Figure 3.23. Observed cracks superimposed on map of the measured displacement amplitudes in New Brighton. Cracks with recorded widths less than 50 mm were excluded for visual clarity (Canterbury Geotechnical Database 2012b).

Figure 3.24 shows observed cracks with correlation results in the Bexley area. In the areas near the river, crack patterns are consistent with the displacement measurements from correlation results. Specifically, deformation is largest where cracks are concentrated, and displacements approach zero beyond crack observations.

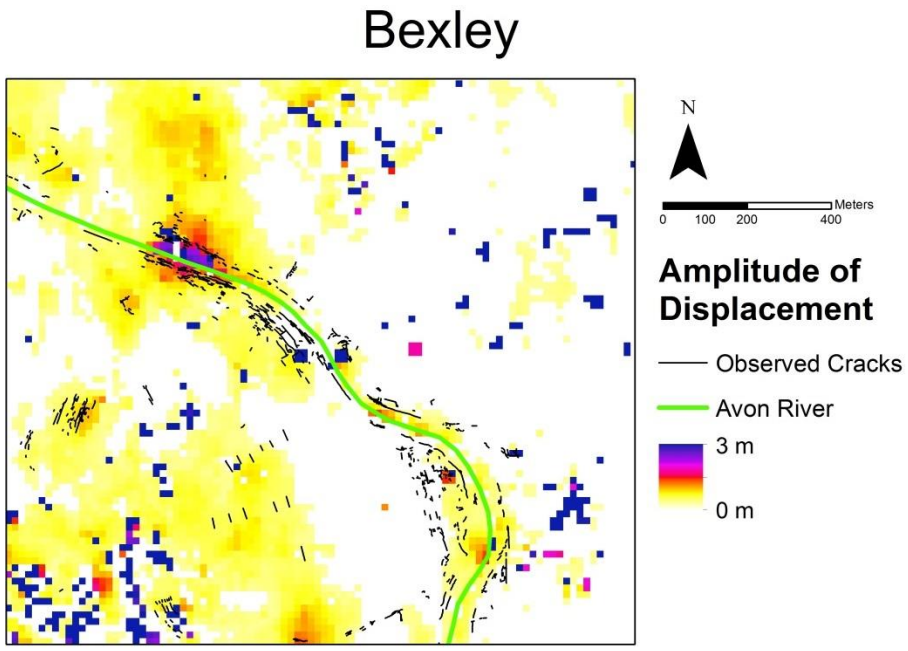

Figure 3.24. Observed cracks superimposed on map of the measured displacement amplitudes in Bexley. Cracks with recorded widths less than 50 mm were excluded for visual clarity (Canterbury Geotechnical Database 2012b).

In most areas, the observed crack patterns are consistent with the lateral spreading displacement patterns from correlation results. Areas of largest displacement are bounded well by cracks, and there is a sharp decrease in measured displacement beyond cracks. Additionally, cracks bound some lateral spreads which extend further than 200 m from the riverbank. However, the full extents of some large lateral spreads were not bounded by crack observations, possibly due to the incompleteness of the crack database

or masking of ejecta. It is also possible that the level of deformation measured in these areas (generally less than 1 m) did not cause cracking.

3.4.4 LiDAR Measurements of Displacement

LiDAR point clouds from before and after the February 2011 Christchurch Earthquake were used in a sub-pixel correlation process developed by Imagin' Labs Corporation and California Institute of Technology (Beavan et al. 2012). This process is similar to the correlation technique used to correlate the optical images. Movements from LiDAR were calculated every 4 m and were averaged to create a grid of measurements every 56 m. Horizontal tectonic movements from GNS Science dislocation models were subtracted from the LiDAR measurements to obtain local deformations due to liquefaction. Correlation analysis on LiDAR data requires topographic features upon which to correlate. As a result, areas associated with waterways and coastal marine areas were poorly correlated and produced inaccurate measurements; these locations were removed from the dataset. The remaining measurements were rendered as arrows scaled 56:1 (i.e. an arrow 56 m long represents 1 m of displacement).

For ease of comparison, the optical image correlation results were averaged to create a grid of measurements with spacing of 48 m. Averaged displacements greater than 6 m were discarded as poorly correlated. Also, measurements in parks, fields, and waterways which were poorly correlated were discarded. Average measurements are represented with arrows having a 56:1 scale for ease of comparison with the LiDAR measurements. Displacements within the precision threshold (0.3 m) are represented

with orange lines, and displacements greater than 0.3 m are represented with yellow arrows.

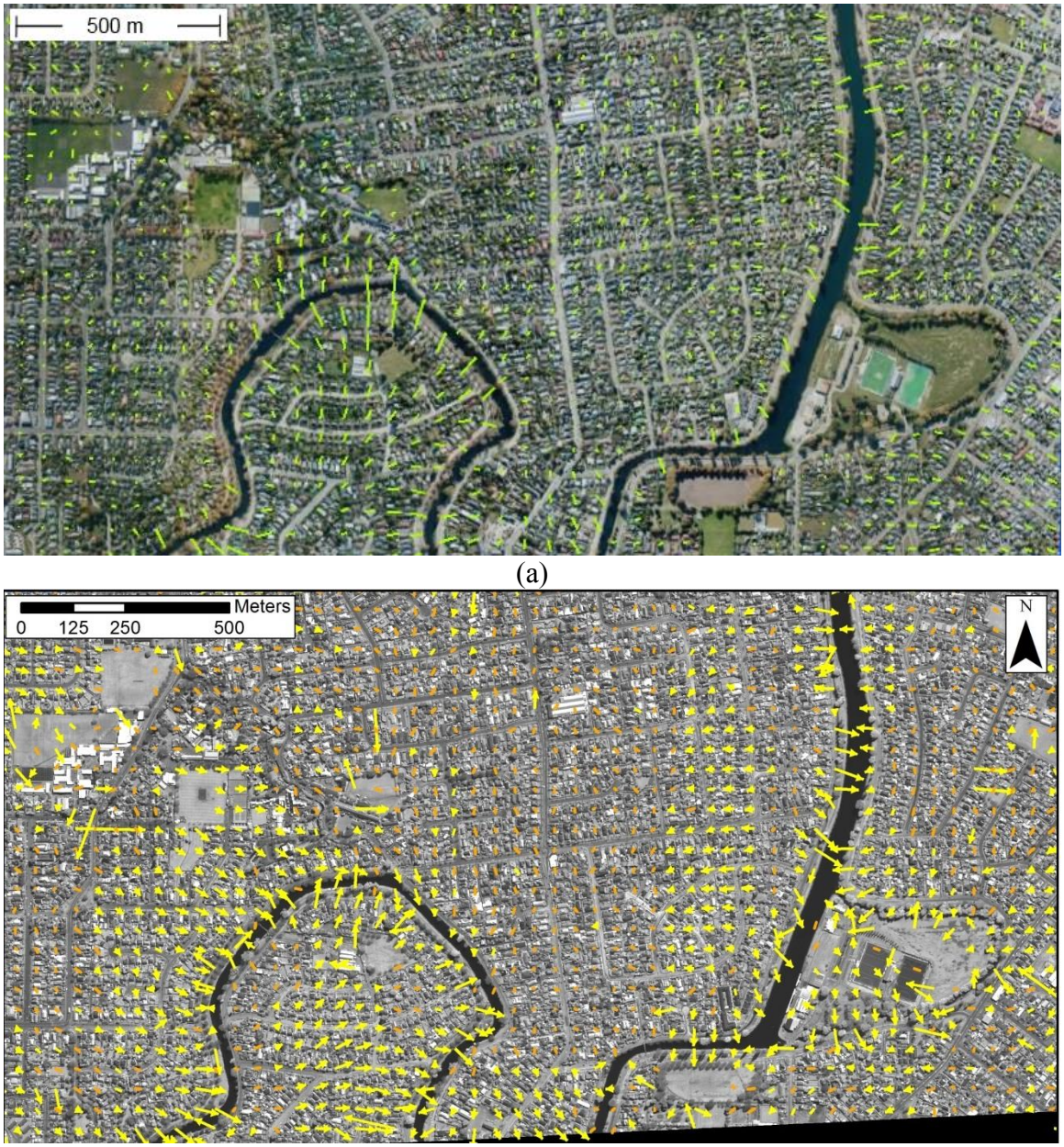

(a)

(b)

Figure 3.25. (a) LiDAR displacement measurements and (b) displacements from optical image correlation in Avonside (Canterbury Geotechnical Database 2012a).

Figure 3.25 shows the displacements from the LiDAR analysis and optical image correlation. The LiDAR measurements generally agree with results from optical image correlation. Displacements are concentrated near the Avon River and attenuate with distance from the river. Also, the general direction and magnitude of arrows from LiDAR correlation matches those from optical image correlation.

Figure 3.26 shows the displacements from LiDAR and optical image correlation in the Avondale area. The displacements from LiDAR agree well with those from optical image correlation in terms of both magnitude and direction. North of the river, both datasets indicate the lateral spreading extends almost 600 m from the riverbank, and the significant deformations in the northeastern part of the image are recorded in both the LiDAR and optical image correlation measurements with similar magnitudes and directions. The others sources of field observations previously discussed did not fully detect the extent of the lateral spreading in these areas, but the consistency between the LiDAR and correlation analyses indicates that displacements did extend a significant distance from the river.

(a)

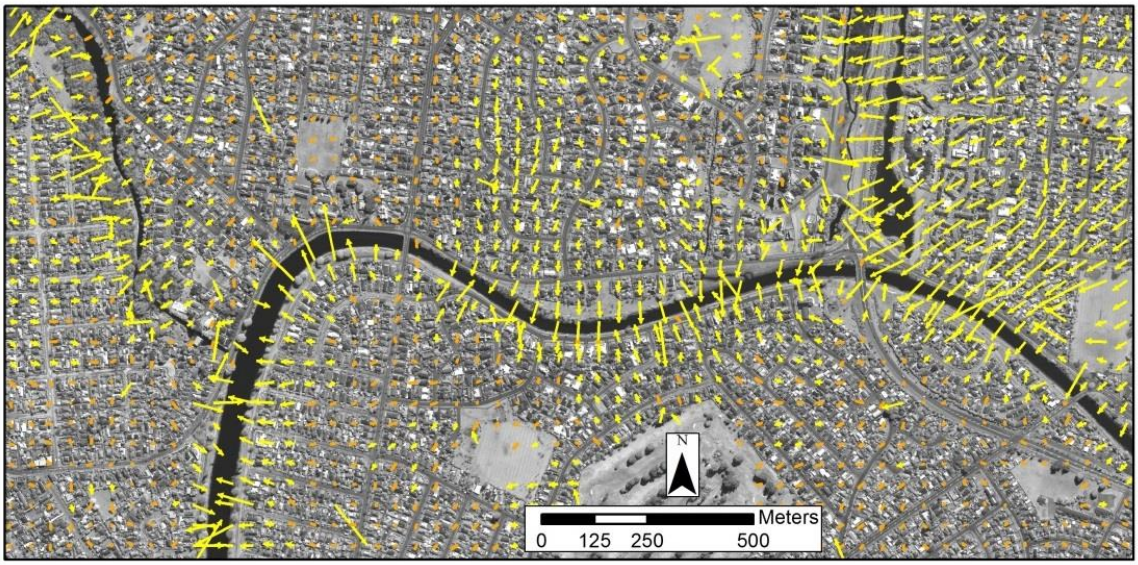

(b)

Figure 3.26. (a) LiDAR displacement measurements and (b) displacements from optical image correlation in Avondale (Canterbury Geotechnical Database 2012a).

(a) (b)

Figure 3.27. (a) LiDAR displacement measurements and (b) displacements from optical image correlation in New Brighton (Canterbury Geotechnical Database 2012a).

Figure 3.27 presents the displacement measurements for the New Brighton area. Both LiDAR and optical image correlation indicate that lateral spreading is severe near the riverbank and that it extends farther than 500 m from the river before termination.

Additionally, the magnitude and direction of displacements are similar in both sets of measurements. This is another location where sources of field observations did not indicate lateral spreading.

Figure 3.28 shows the displacements in the Bexley area rendered from the two methods. Generally, the displacement patterns from optical image correlation and LiDAR correlation are the same. The LiDAR results confirm movement in the old sandy alluvium in the south-central part of Bexley, but the LiDAR does not show significant displacement near the western bank of the river in the south part of the image. However, lateral spreading in this area was noted in the field observations.

(a)

(b)

Figure 3.28. (a) LiDAR displacement measurements and (b) displacements from optical image correlation in Bexley (Canterbury Geotechnical Database 2012a).

Ten transects of displacement in zones of lateral spreading along the Avon River were measured using traditional methods following the 2011 Christchurch Earthquake (Robinson et al. 2012). These measurements were taken by measuring widths of cracks associated with identified lateral spreading along a linear transect and summing the crack widths to obtain a relationships of the permanent displacement versus distance from the river. All field-measured cracks were assumed to contribute to movement towards the river only. The detailed displacements along ten transects were obtained from the University of Canterbury through personal communication with Misko Cubrinovski for comparison with image correlation measurements. For each transect displacements from field measurements and from the correlation analysis are plotted versus distance from the riverbank.

For comparison with the field measurements, displacements along the transects were computed from the correlation analysis by sampling measurements every 10 m along each transect. At each sampling point, the displacement measurements perpendicular to the transect and within 24 m of the transect were averaged to get a representative displacement. An example of the pixels used to estimate displacements along transect AS-1 is shown in Figure 3.29. Each color represents a sampling group of three pixels. From these sampled measurements, both the total displacement amplitude and the displacement perpendicular to the river were computed. The total displacement amplitude is the magnitude of displacement without regard to direction. The displacement perpendicular to the river is the magnitude of the displacement in the direction of the transect and negative values represent movement away from the river. If all displacement is directed along the transect and toward the river, both displacements will be the same. For comparison to the field measurements, displacement perpendicular

to the river is more relevant. Transects will be examined individually, and their locations on satellite imagery will be shown. The transect locations are also shown with the north/south and east/west displacement measurements in Figure 3.7 and Figure 3.8.

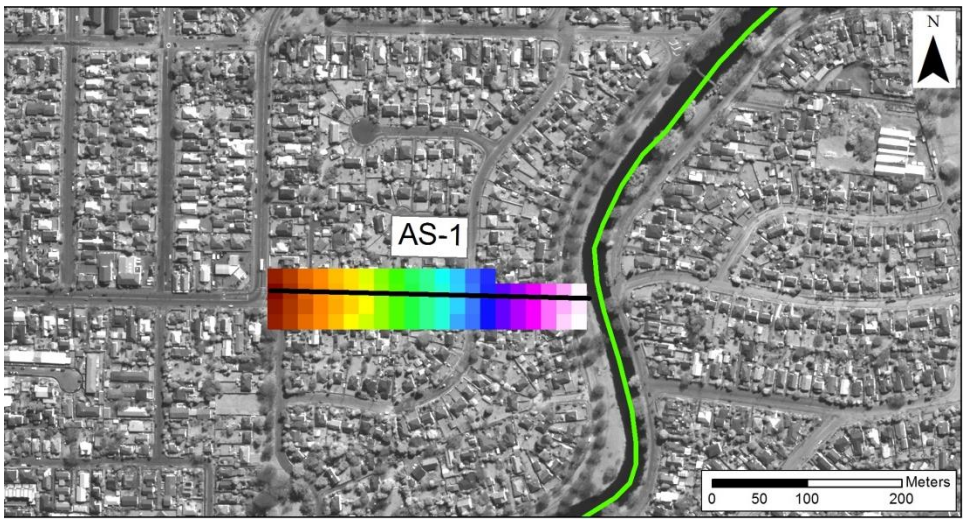

Figure 3.29. Example of transect calculation from correlation results.

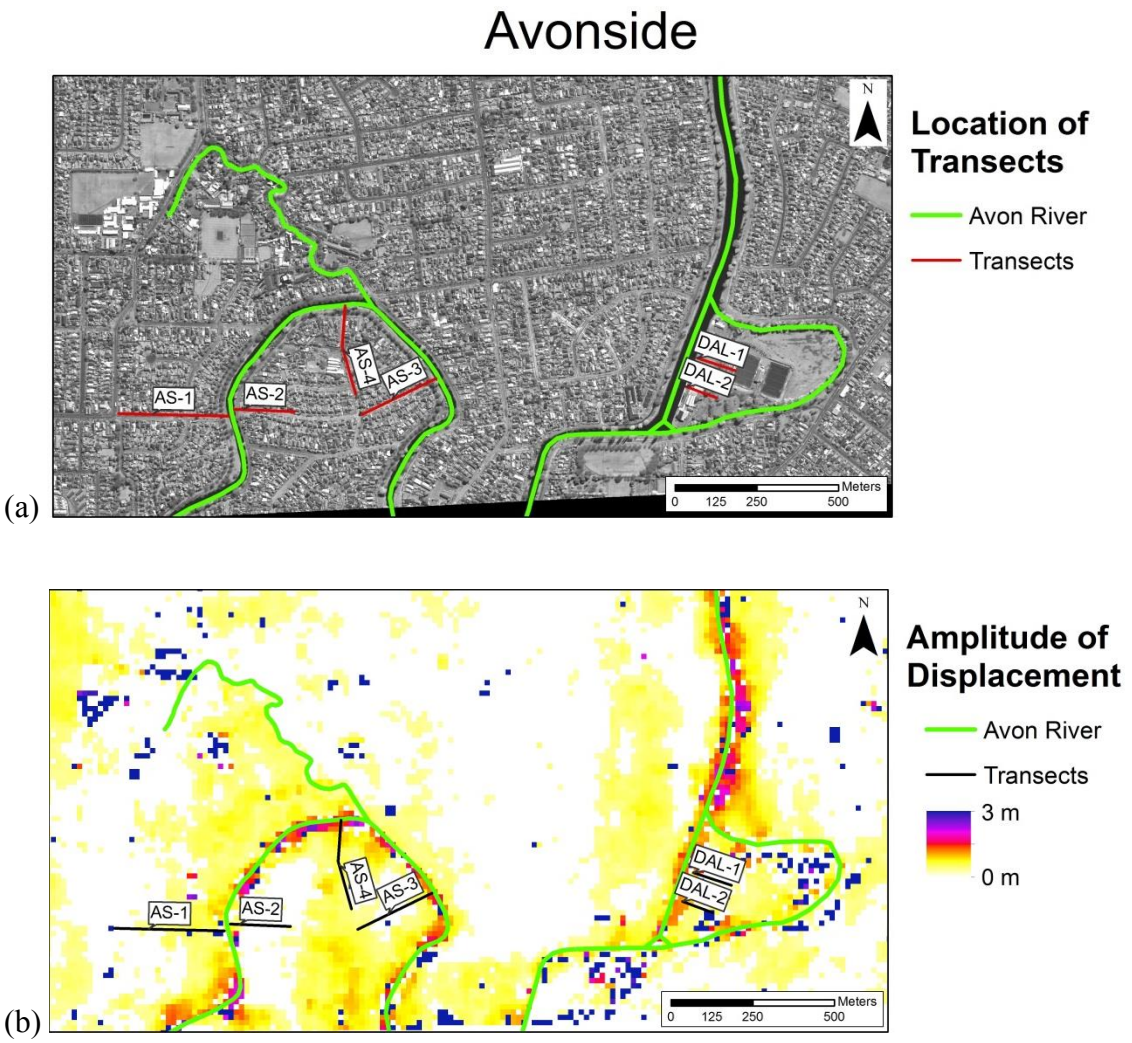

Figure 3.30. (a) Location of transects in the Avonside area and (b) displacement amplitudes from correlation analysis with respect to transect locations.

Figure 3.30 shows the locations of the six transects within the Avonside area. Field measurements for AS-1 were collected four months after the Christchurch earthquake on May 20, 2011 by measuring cracks along North Avonside Drive. These cracks were predominately in sidewalks, retaining structures, and road curbs. Cracks in road curbs were only measured where similar cracks appeared on both sides of the street.

Also, where the road ended near the river, separation between the asphalt pavement and the street gutter was assumed to be from lateral spreading. Other cracks may have been missed because the street had been repaired at the time of survey. Figure 3.31 presents displacement versus distance from the riverbank from the two methods for AS-1. For the correlation analysis, total displacement amplitudes closely follow displacements oriented perpendicular to the river indicating the movement was predominantly towards the river. The correlation results match the ground survey near the river, but beyond 50 m from the river edge the correlation results show larger displacements than ground observations. The lateral spread displacements terminate within 300 m of the riverbank according to the ground survey, but the correlation results indicate movements extend further than 300 m from the river.

Transect AS-2 was measured eastward along the west end of Robson Street on April 7, 2011. Cracks in the street and the top of the riverbank were measured for the ground survey. No other specifics were provided regarding the ground survey. Figure 3.32 shows the ground survey measurements with the correlation analysis results. The correlation analysis results show some differences between the total displacement amplitudes and the displacements perpendicular to the river. The negative displacement perpendicular to the river near the river edge may be due to the pixel at the river edge being influenced by displacements from the other side of the river. Note that the displacements for each pixel represent the average across an area of 64 m by 64 m, and thus pixels close to the river extend across the river. It is not clear why other transects were not affected in the same way. The displacements in Figure 1.33 agree well over distances of 20 to 100 m from the river.

Also on April 7, 2011, transect AS-3 was surveyed along the east side of Robson Street. Measured cracks were predominately in the street curbs and sidewalks. Some cracks were difficult to measure as they had been repaired. Some cracks were compressed due to localized uplift. In areas farther from the river, it was unclear if the cracks were associated with lateral spreading or other liquefaction induced deformation (e.g., ground settlement). Figure 3.33 shows the displacement measurement from image correlation and the field survey for AS-3. For the correlation analysis, the total displacement amplitude closely matches the displacement perpendicular to the river along the majority of the transect showing most lateral deformation occurred in the direction of the transect. The increase in displacement beyond 150 m from the river shown by the correlation results is likely part of a separate lateral spread which is oriented toward the east (See Figure 3.30(b)). Both the ground survey and correlation analysis indicate lateral spreading along AS-3 terminates around 140 m from the river, and both show the permanent displacement near the river is close to 1 m.

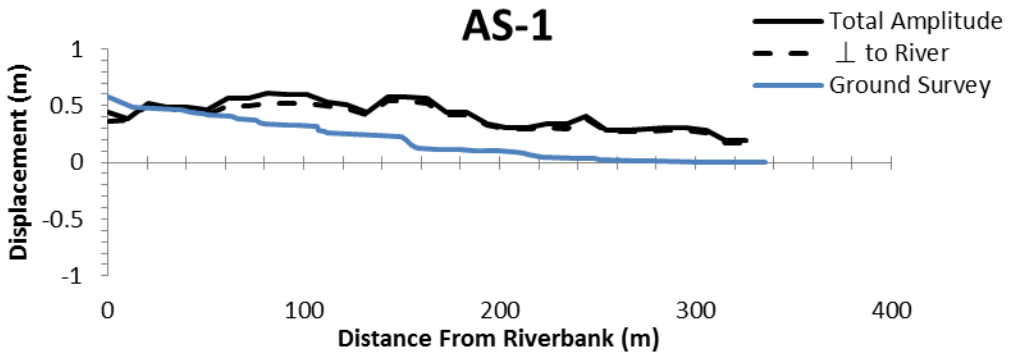

Figure 3.31. Comparison of transect measurements at AS-1 in Avonside.

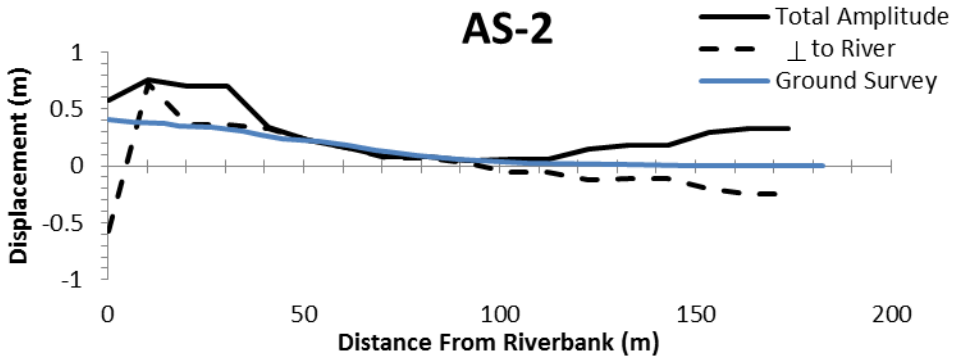

Figure 3.32. Comparison of transect measurements at AS-2 in Avonside.

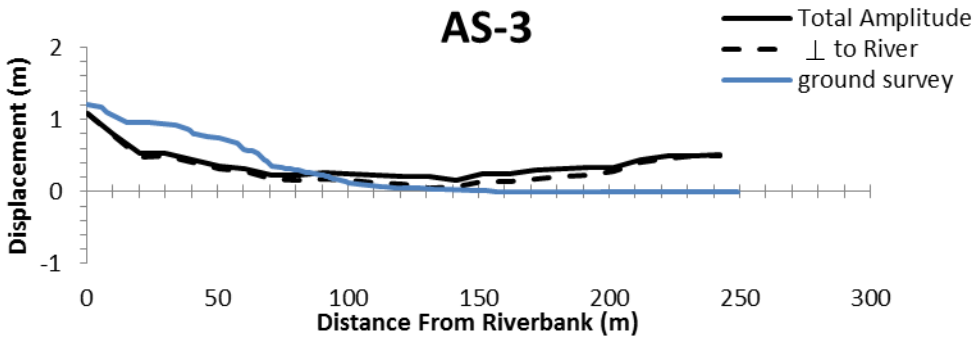

Figure 3.33. Comparison of transect measurements at AS-3 in Avonside.

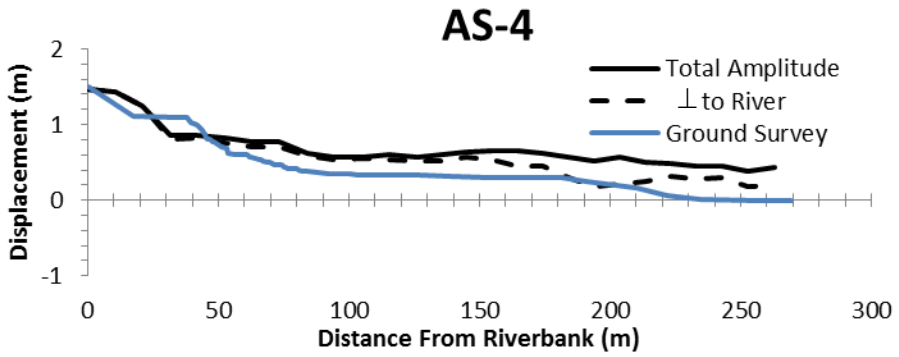

Figure 3.34. Comparison of transect measurements at AS-4 in Avonside.

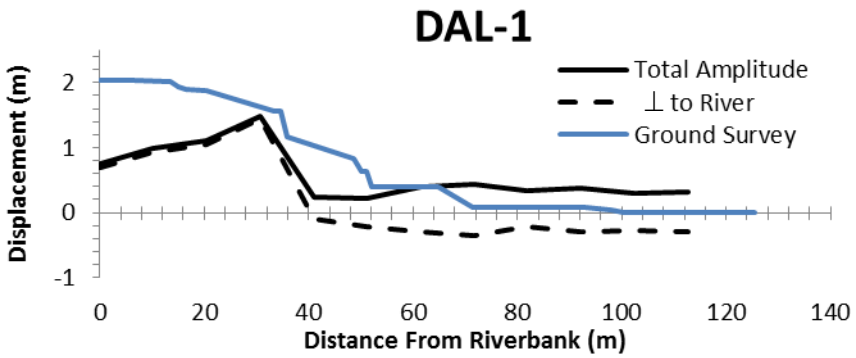

Figure 3.35. Comparison of transect measurements at DAL-1 in Avonside.

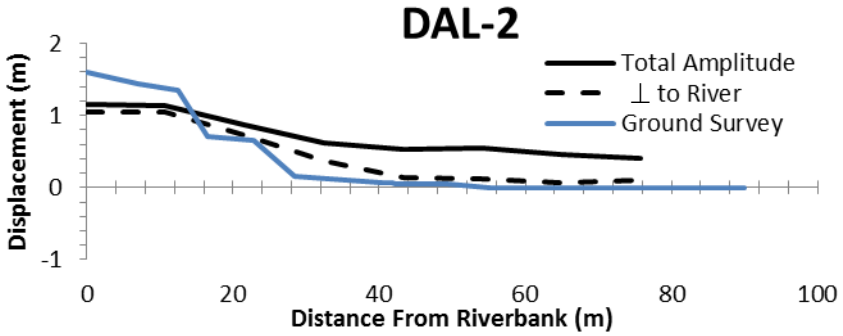

Figure 3.36. Comparison of transect measurements at DAL-2 in Avonside.

Displacement measurements for transect AS-4 were acquired on March 7, 2011 along Gailbraith Drive. Cracks in the street, curb, and sidewalk were measured, and

cracks in the curb were only measured if similar cracks could be found on both sides of the street. Some cracks were partially filled with sand, and the cracks after the shift in the street were transposed onto an ideal transect in a graphical information system (GIS). Figure 3.34 shows the measured displacements versus distance from the river. Correlation results show most of the measured displacement occurred toward the river. Both the ground survey and correlation results suggest the permanent displacement at the riverbank is close to 1.5 m, and both match in their distribution of permanent displacements with respect to distance from the river. The ground survey indicates that the lateral spread displacements terminate around 220 m from the riverbank, but the correlation analysis suggests the lateral spread terminates about 250 m from the river.

Measurements for transect DAL-1 were collected in Porrit Park on March 2, 2011. Cracks were found in the grass, footpath, and parking lot. Some areas in the grass exhibited a graben structure, making measurements difficult. All observed cracks were thought to contribute to lateral spreading moving to the west. Figure 3.35 shows the measured displacements with respect to distance from the river. Within 40 m, the correlation results indicate most of the movement is in the direction of the transect, but displacement beyond 40 m may be due to lateral spreading towards the creek to the south and east (see vectors in Figure 3.25). When compared with the ground survey measurements, the correlation results are very different. The correlation results indicate that lateral spreading terminates abruptly at 40 m, but the ground survey indicates lateral spreading displacements continue to about 70 m from the river. Additionally, permanent displacement measurements at the riverbank differ by more than 1 m. Cubrinovski (personal communication) suggested differences may be explained in part by the assumption that all cracks contributed to movement toward the river along the measured

transect. This explanation is supported by the correlation displacement vectors in Figure 1.27 that show movement towards the east within the park. Differences may be further influenced by poor performance of correlation analyses in fields that do not have significant tonal variation upon which to correlate. This makes the displacement estimates more uncertain in these areas.

Transect DAL-2 was measured on March 2, 2011. Cracks in pavement, concrete, and a gravel lot were measured. Many cracks were filled with sand, and a line of sand boils was observed near 50 m from the river. Cubrinovski and his students also noted that cracks from settlement were difficult to distinguish from cracks due to the lateral spreading, and that southward lateral spreading occurred near the end of the DAL-2 transect. These challenges caused much difficulty in field measurement of the lateral spread. Figure 3.36 shows the distribution of displacements along DAL-2. Correlation results show that most movement is towards the river within 20 m of the riverbank. Ground survey results match the correlation results moderately well. Both methods show the lateral spreading displacement terminating within 50 m of the river, and the distribution of displacement is similar throughout. Permanent displacements at the river edge are from 1.0-1.5 m. Differences in measurements can be explained by the difficulty of ground measurements and the challenges of correlation analyses in grassy areas.

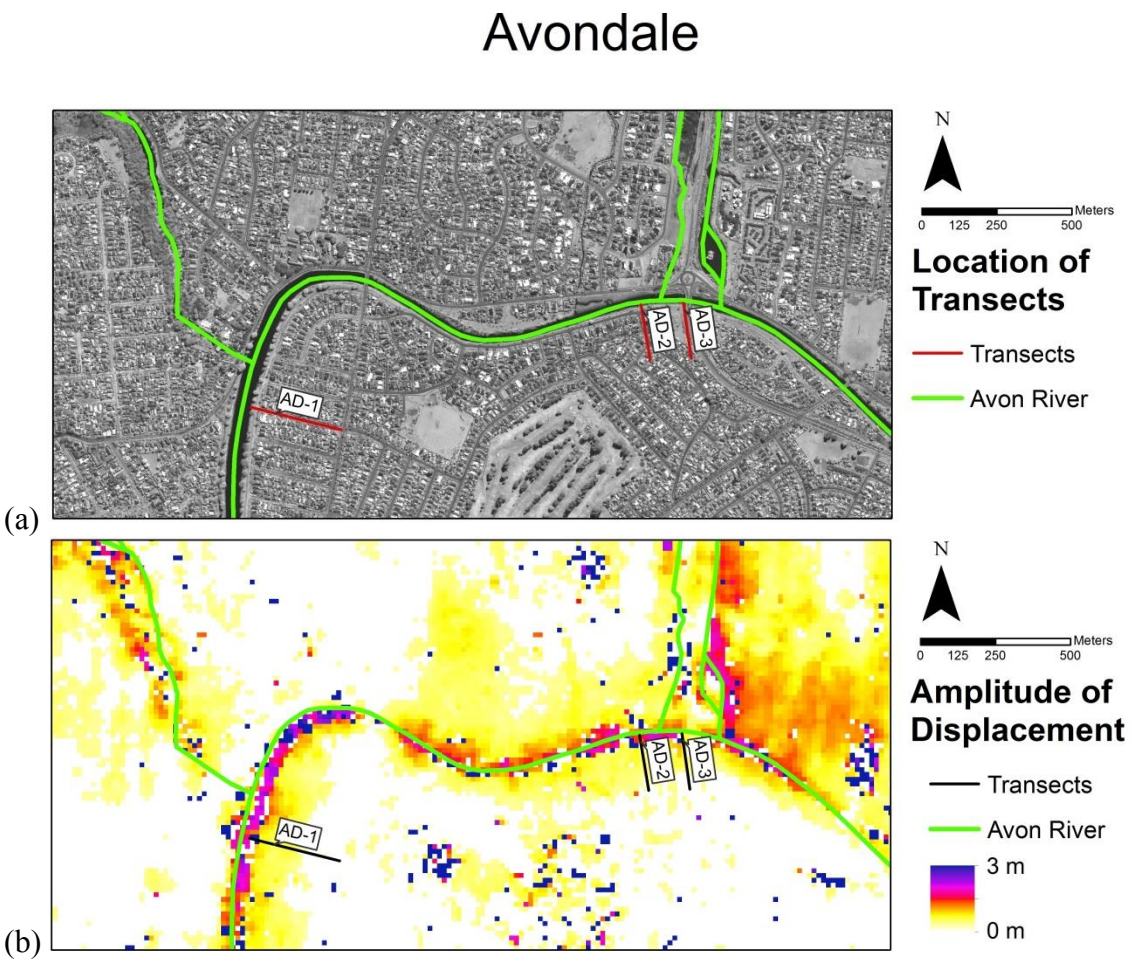

Figure 3.37. (a) Location of transects in the Avondale area and (b) displacement amplitudes from correlation analysis with respect to transect locations.

Figure 3.37 shows the locations of the transects in the Avondale area. AD-1 was collected on March 28, 2011 along Wooley Street. Cracks in the grass of the riverbank, street curbs, sidewalks, and retaining structures were measured. By the time of the ground survey, parts of the road and the riverbank had been repaired, so some cracks may not have been identifiable. Additionally, cracks beyond 160 m from the river were observed, but they were judged to be from local settlement due to liquefaction, not lateral spreading. Figure 3.38 shows the measured displacements versus distance from the

riverbank for AD-1. Correlation results indicate all movement was oriented in the direction of the transect. Both the ground survey and correlation measurements show the permanent displacement of the riverbank was approximately 1.7 m, but the two methods differ in the distribution of displacements with distance from the river. The ground survey indicates the lateral spreading displacement terminates at 140 m of the river, while the correlation results indicate the lateral movements extend to nearly 280 m from the river before termination. This difference may be due in part to misinterpretation of observed cracks beyond 150 m from the river.

Measurements for transect AD-2 were collected on May 3, 2011 west of the south abutment of the Anzac Bridge. Measured cracks were predominately in the grass along the river bank, sidewalks, and the street. Most of these cracks were filled with sand, so measurement of their widths was difficult. Also, it was unclear whether some cracks were due to local settlement or lateral spreading. Figure 3.39 shows the displacement measurements from the ground survey and correlation analysis. Correlation results indicate nearly all movement occurred in the direction of the transect. Results from the two methods produce very different levels of displacement. The ground survey indicates small permanent displacement (~0.4 m) near the river which diminishes to zero within 110 m of the river. The correlation results indicate a lengthy lateral spread which extends beyond 180 m before terminating and significant permanent displacement (~1.5 m) near

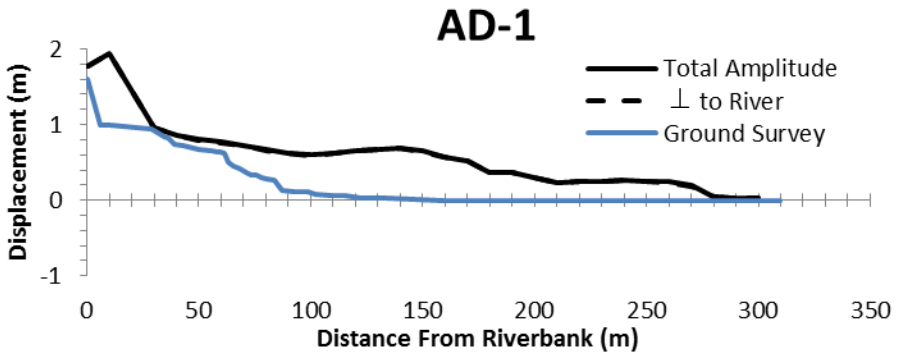

Figure 3.38. Comparison of transect measurements at AD-1 in Avondale.

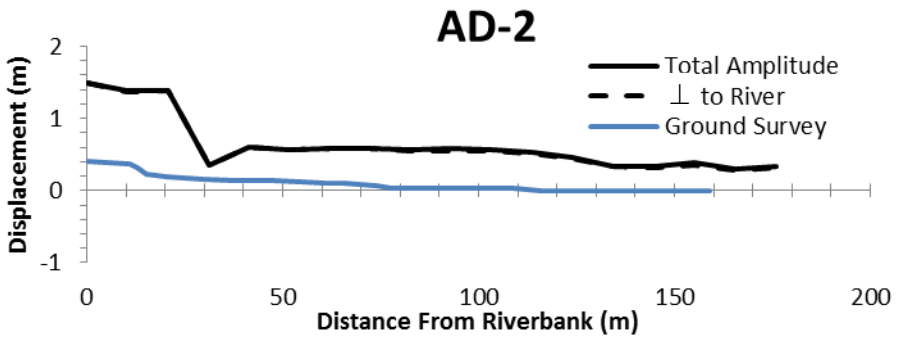

Figure 3.39. Comparison of transect measurements at AD-2 in Avondale

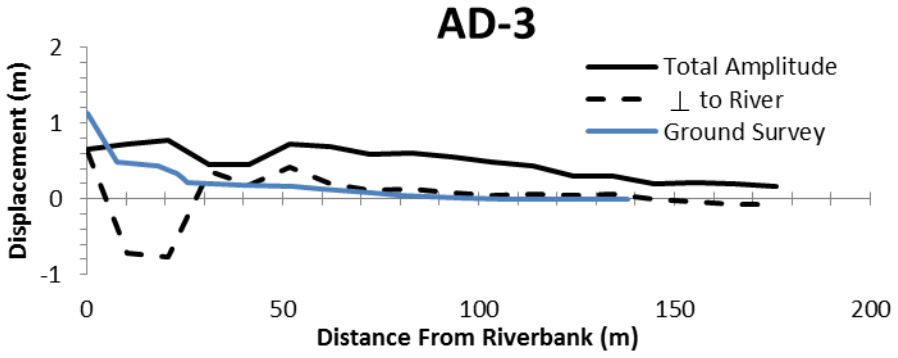

Figure 3.40. Comparison of transect measurements at AD-3 in Avondale

the river. These differences may be explained in part by the filled nature of cracks in this area when surveyed; however, differences from the two measurements are significant.

Transect AD-3 was surveyed on May 3, 2011 next to the south abutment of Anzac Bridge. Cracks were found in the grass and a footpath just east of the transect. Most cracks in the grass were filled with sand, and cracks found in the footpath were transposed onto the idealized transect to create the displacement measurements. Figure 3.40 compares the displacement measurements from the ground survey and from optical image correlation. The correlation analysis indicates not all movement was oriented in the direction of the transect. Examination of Figure 3.8 reveals some westward displacement was recorded in this area. Displacements toward the river from the correlation analysis match displacement measurements from the ground survey from about 30 m to the termination of displacement about 90 m from the riverbank. However, displacements within 30 m of the river differ greatly. Here, displacements from the correlation analysis are likely not associated with lateral spreading along AD-3, but displacements may be associated with surface of the bridge moving 0.5-1.0 m southward.

Figure 3.41 shows the location of transect BX-1 in the Bexley area. Measurements for BX-1 were collected on May 23, 2011 along Brooke Street by measuring cracks in the street, a concrete path, and street curbs. Many cracks were measured just north of the transect and were transposed onto the transect to obtain displacement measurements. Figure 3.42 presents the displacement measurements versus distance from the riverbank. The correlation analysis suggests all displacement is in the

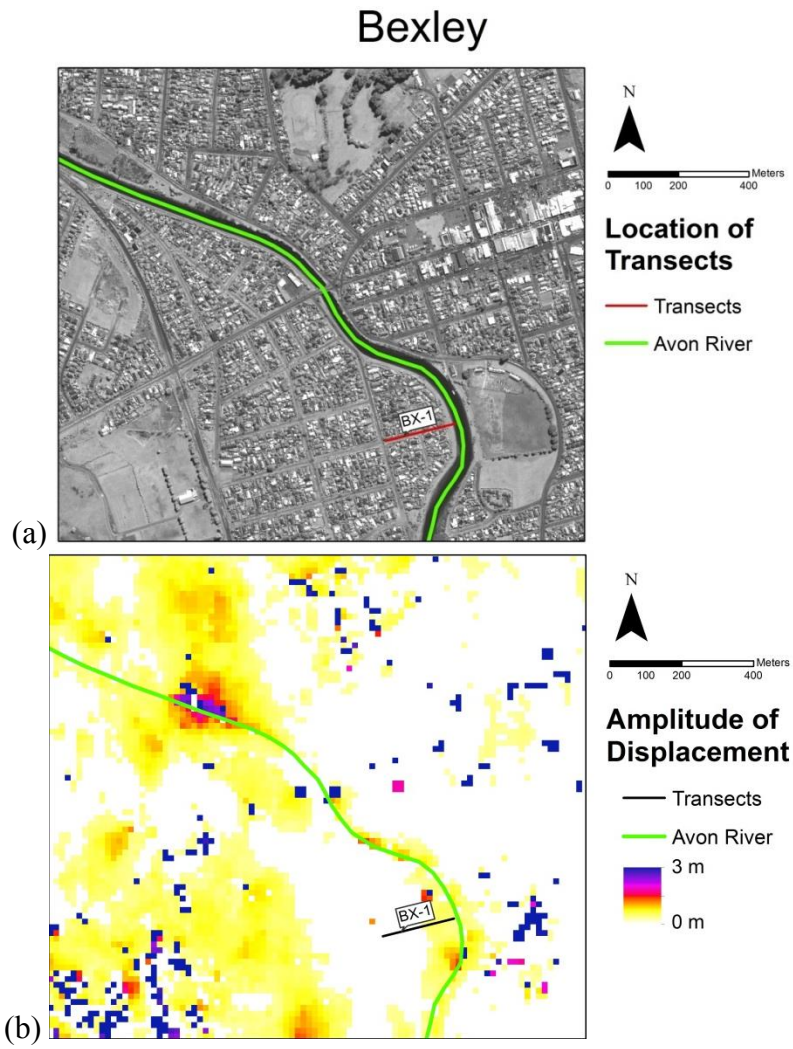

Figure 3.41. (a) Location of transects in the Bexley area and (b) displacement amplitudes from correlation analysis with respect to transect locations.

direction of the transect. Both correlation results and ground survey measurements show permanent displacement of the riverbank is about 0.5 m, and the two methods indicate a similar distribution of displacements with respect to distance from the river. Also, both methods agree that most displacement terminates about the 130 m of the river. The slight displacement measured by the correlation analysis beyond 130 m is less than 0.1 m, which is within the margin of error for the correlation analysis.

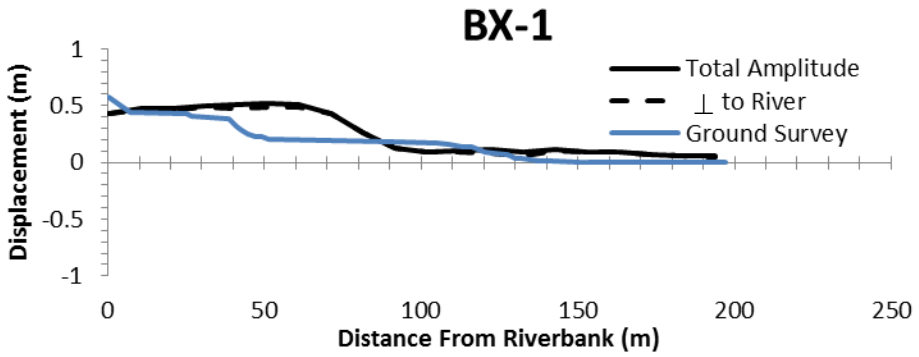

Figure 3.42. Comparison of transect measurements at BX-1 in Bexley.

Although some differences were found in the optical image correlation and ground survey measurements, results matched well overall. Permanent displacements at the riverbank, the distribution of displacement with respect to distance from the river, and the termination locations of lateral spreading displacements were similar for both methods. Many differences were within the range of error for the correlation analysis (0.15 m) or could be readily explained.

Chapter 4: Optical Image Correlation Analysis of Lateral Spread Displacements in Kaiapoi, New Zealand from the 2010 Darfield Earthquake

4.1 Introduction

This chapter describes the use of optical image correlation to measure liquefaction-induced horizontal deformation in Kaiapoi, New Zealand from the 2010 Darfield (Canterbury) Earthquake. Section 4.2 describes the earthquake and general observations of the earthquake damage in the town of Kaiapoi. Section 4.3 discusses the process by which images were selected, corrected for distortions, correlated, and post-processed. Finally, Section 4.4 presents the optical image correlation results and compares them with zones of expected liquefaction, qualitative observations of liquefaction and lateral spreading, displacement measurements from LiDAR point cloud correlation, and transect measurements from traditional ground surveys.

4.2 2010 Darfield (Canterbury) Earthquake

On September 4, 2010, a Mw 7.1 earthquake occurred along a previously unknown strike-slip fault located roughly 10 km southeast of Darfield, New Zealand. Figure 4.1 shows the location of the earthquake's epicenter. The earthquake caused widespread damage and liquefaction, especially in the town of Kaiapoi. In Kaiapoi, severe liquefaction and lateral spreading were observed at the locations of former river channels of the Waimakariri River, where loose silty sands extend to a depth of 8-9 m and the water table is within 1-2 m of the ground surface (Green et al. 2010). Liquefaction-induced deformations caused severe damage to many structures, and the

liquefied zones were widespread. Figure 4.2 shows some photos of damage to residential structures in Kaiapoi from liquefaction and lateral spreading, and Figure 4.3 shows an example of the large extent of liquefied zones (notice the cars and trucks for scale).

Figure 4.1. Location of Kaipoi study area for the Darfield Earthquake (Google Earth 2014).

Figure 4.2. Liquefaction and lateral spreading damage in Kaiapoi, NZ (Green et al. 2010).

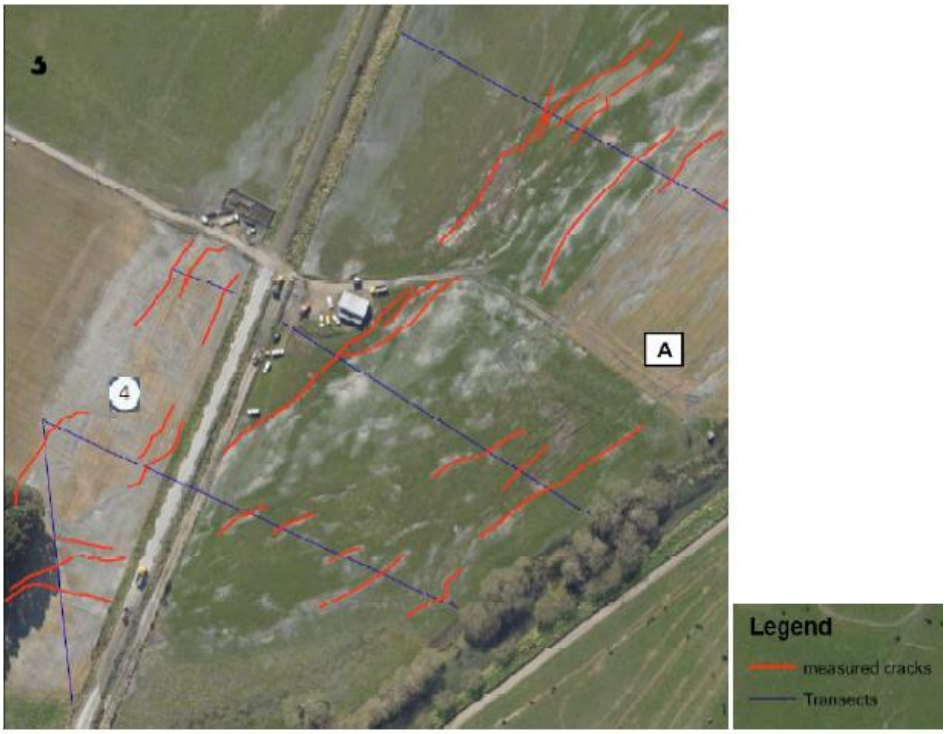

Figure 4.3. Example of large scale liquefaction and lateral spreading (Green et al. 2010).

4.3 IMAGE SELECTION AND PROCESSING

Given the severity and widespread deformations reported near Kaiapoi, a region of study was identified for application of optical image correlation (Figure 4.1). The top 100 m of soils in this area are Holocene and consist of fluvial deposits. Loose silty sands have been found within 8-9 m of the ground surface in previous channels of the Waimakariri River, and the water table at Kaiapoi is typically within 1-2 m of the ground surface (Green et al. 2010).

Two panchromatic (i.e. greyscale) images of 0.5 m resolution were selected based on their similar acquisition angles. Figure 4.4 shows the pre-earthquake image with South Kaiapoi outlined in red. The pre-earthquake image was acquired on February 22, 2010 from the WorldView-2 satellite, nearly one year before the post-event image was acquired with the GeoEye-1 Satellite on January 27, 2011. Of significance, the post-event image was acquired before the February 2011 Christchurch earthquake. The acquisition angles of the pre- and post-event images are agreeable, with target azimuth angles of 237.1° and 232.8° and off-nadir angles of 15.6° and 9.3° for the pre- and post-event images, respectively. By using equations 2.1 , 2.2, and 2.3 and assuming a pseudo-suborbital path of 0° (i.e. $\theta_0 = 0$), north/south look angles (T) of 8.62° and 5.65° and east/west look angles (S) of 13.19° and 7.43° can be established for both the pre- and post-event image, respectively. The difference in the north/south look angles is 2.97°, and the difference in the east/west look angles is 5.76°. Because the north/south look angles are smaller than the east/west look angles and because the difference in north/south look angles is smaller than the difference in the east/west look angles, distortions from topography will be less significant in the north/south direction, and optical image correlation will perform better in the north/south direction.

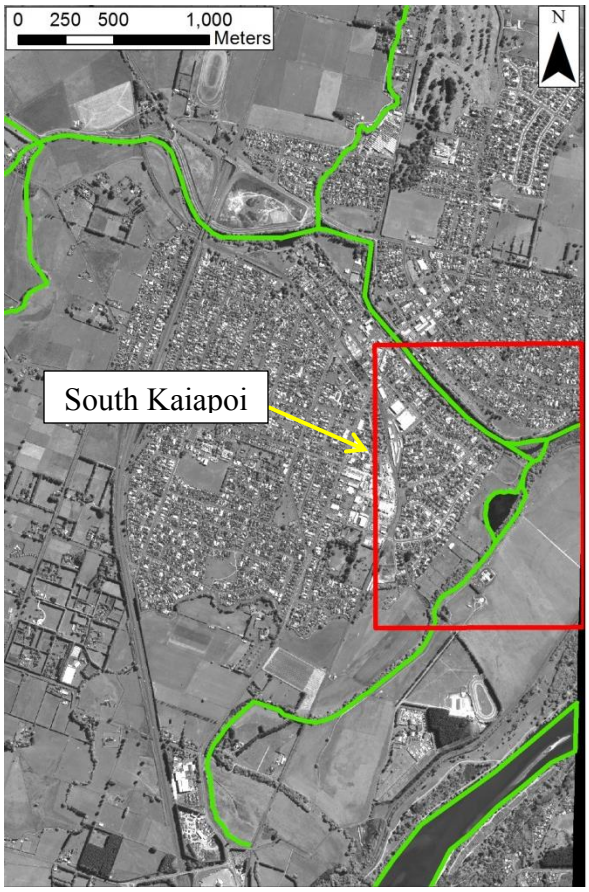

Figure 4.4. Pre-earthquake image.

Both images were orthorectified using the GDAL (Geospatial Data Abstraction Library, GDAL 2012) with a 90-m resolution digital elevation model (DEM) from the Shuttle Radar Topography Mission (SRTM, USGS 2004). As described in Section 3.3 for the Christchurch pair, tie points were generated using ENVI's automatic tie point generation software. Tie points within 200 m of major waterways were not included, and tie points with high residuals when compared with the warping polynomial were excluded. Ultimately, 650 well-distributed tie points (40.5 points per km^2) were selected

for co-registration. The overall RMSE for the 650 points was 0.36 m. Figure 4.5 shows the tie points used for co-registration.

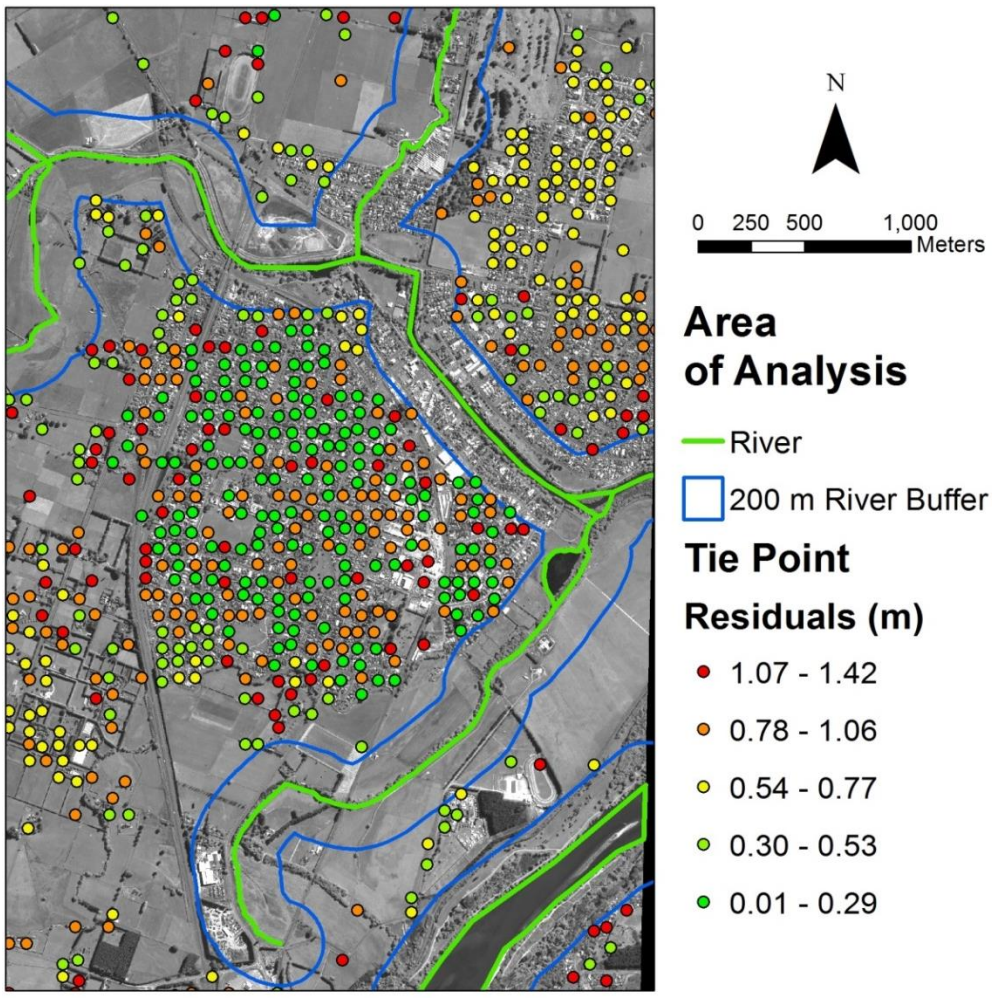

Figure 4.5. Tie points used for co-registration.

Following co-registration, the images were correlated using the method presented by Leprince et al. (2007). A chip window size of 256 pixels (128 m) was used with a step size of 32 pixels, yielding a displacement measurement every 16 m. The chip window size used for correlation in Kaiapoi is larger than the one used for the

Christchurch area (128 pixels) because the areas around Kaiapoi are more agricultural and thus have fewer features and more homogeneous texture. This larger chip window reduces noise such that displacement patterns are clearer. Results were filtered such that measurements with a signal-to-noise ratio (SNR) less than 0.95 were tagged as "decorrelated", and a precision threshold of 0.37 m was established based on the co-registration RMSE.

4.4 Deformation Results and Comparisons

Displacements were measured in the north/south and east/west directions using optical image correlation. Figure 4.6 shows the measured displacements in the north/south direction. Displacements less than the precision threshold of 0.37 m were set to zero for visual purposes. Northward movement is indicated by yellow/red with red representing displacement in excess of 3 m. Southward movement is represented by blue/purple with purple indicating displacement in excess of 3 m. Generally, significant displacements are near waterways, and little to no coherent patterns of displacement are seen further than 300 m from the waterways. Recorded displacements north of the river are directed southward, and displacements south of the river are directed northward. Some areas, especially outside the South Kaiapoi region of interest, have much more noise than those toward the center of the analyzed image pair where the majority of Kaiapoi's population resides. Correlation results are better near populated areas (i.e. areas with many structures) than in rural areas because the agricultural fields of the rural areas possess similar texture. This similar texture leads to false positives for optical image correlation and less reliable results.

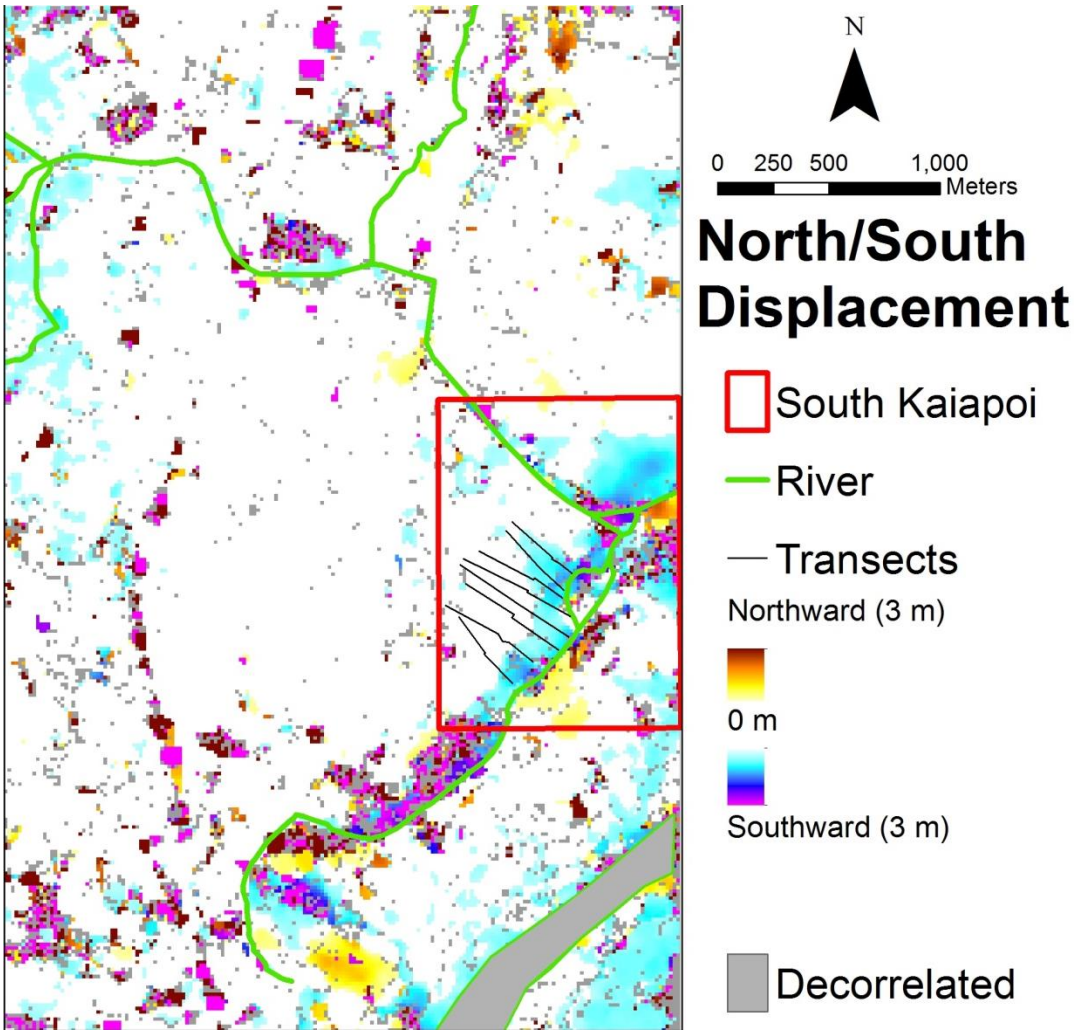

Figure 4.6. North/south displacement measurements.

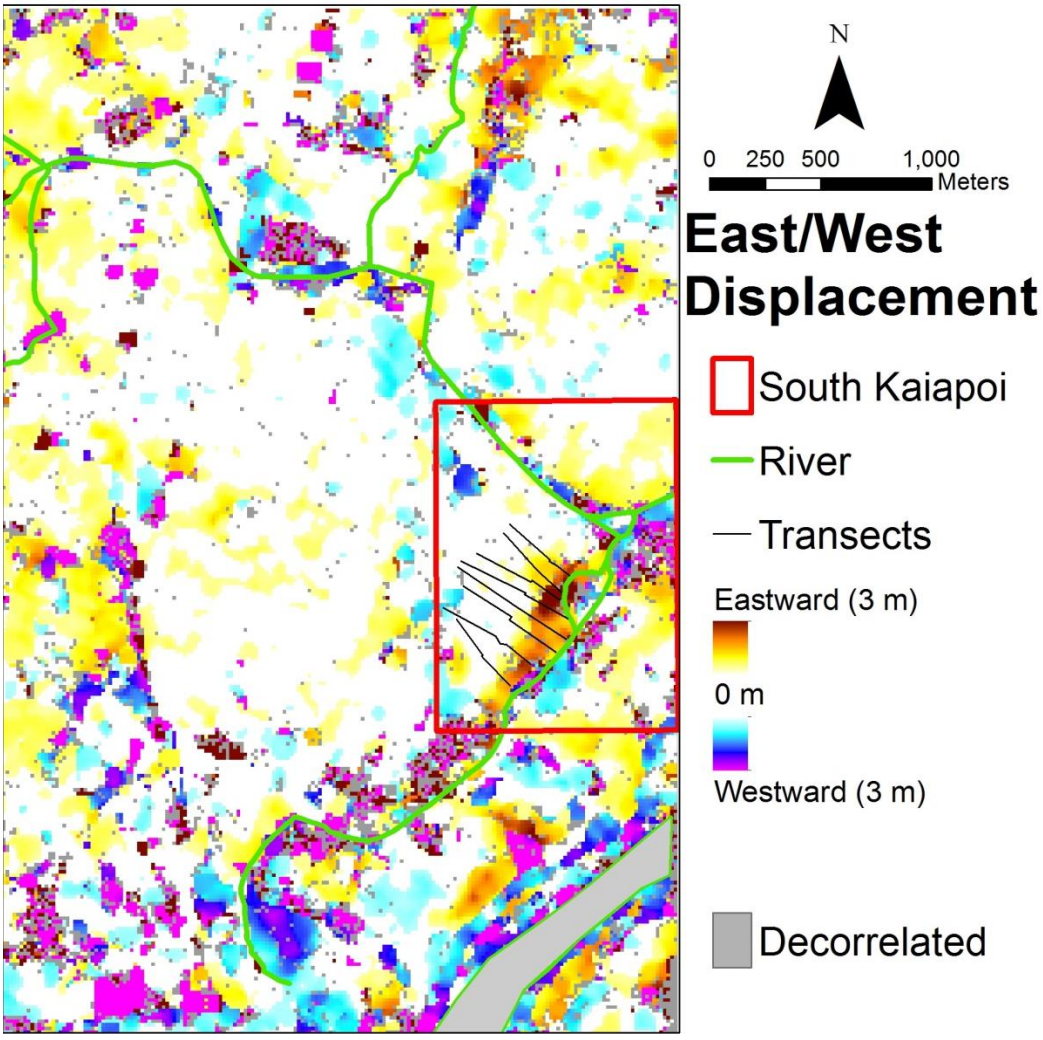

Figure 4.7. East/west displacement measurements.

Figure 4.7 presents the displacements measured in the east/west direction. Again, displacements less than the precision threshold of 0.37 m were set to zero for visual purposes. Eastward movement is represented by yellow/red with red indicating more than 3 m of eastward displacement. Westward displacement is symbolized by blue/purple with displacements in excess of 3 m indicated by purple. As with the north/south displacement measurements, correlation patterns are more coherent around

the populated areas of Kaiapoi, especially in the area marked “South Kaiapoi”. In these areas, displacements are concentrated around the waterways, and little to no displacement is seen beyond 300 m from the waterways. Areas west of the waterways displace eastward, and areas east of the waterways displace westward. However, in less populated areas, the correlation results are poor and results are noisy. Again, correlation results in the east/west direction are not as good as those in the north/south direction because the angles are less agreeable in the east/west direction.

4.4.1 Expected Liquefaction

In 1901, the Cheviot earthquake of estimated magnitude 6.5-7.0 caused liquefaction and lateral spreading in the residential areas of Kaiapoi (Berrill et al. 1994). Specifically, a local newspaper detailed the liquefaction and lateral spreading within two to three town blocks in Kaiapoi. By talking with residents in Kaiapoi, Berrill et al. (1994) were able to establish the location of liquefaction described by the newspaper. Figure 4.8 shows the 1901 liquefied area with the historical layout of Kaiapoi. This account of previous liquefaction shows that soils in and around Kaiapoi are susceptible to liquefaction and conditions for liquefaction have existed around the riverbanks in the past. Deformation results in Figure 4.6 and Figure 4.7 show the area of 1901 liquefaction severely displaced toward the river, indicating liquefaction reoccurred in this area.

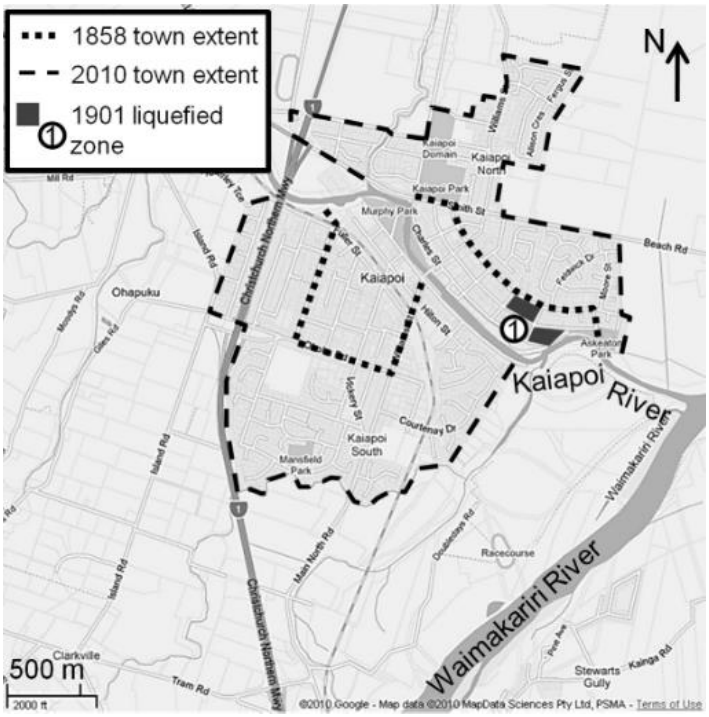

Figure 4.8. Historical Kaiapoi and area of liquefaction in 1901 (Wotherspoon et al. 2012).

The former channels of the Waimakariri River are relevant to expected areas of liquefaction as well. Figure 4.9 shows the path of the Waimakariri River circa 1865. Starting in the southwest corner, the river splits into a northern branch (shaded green) and a southern branch (shaded red) which rejoin near Kaiapoi. The path of the river was altered by manmade channels until it shifted to its present path by 1930 (red dashed line) (Wotherspoon et al. 2012). After the river's shift, flow through the former river channels was reduced to smaller streams, and sediment collected in the former riverbeds (Wotherspoon et al. 2012). Figure 4.10 shows the location of the southern branch of the Waimakariri River circa 1865 (shaded red) superimposed on a Google map of present-day South Kaiapoi. Since the conditions in the former riverbeds are suitable for liquefaction and since widespread liquefaction was observed in these areas (Wotherspoon

et al. 2012), significant displacements from liquefaction induced deformation are likely to be observed in the former channels of the Waimakariri River. From Figure 4.6 and Figure 4.7, one can see a strong correlation between the former river channel and the area of severe horizontal displacement. The largest displacements in South Kaiapoi are contained within the old river path.

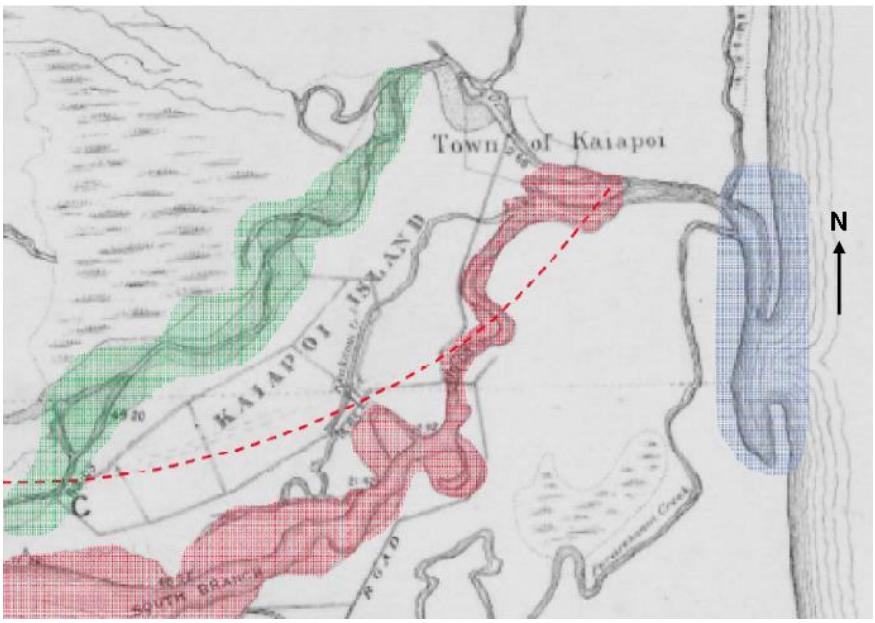

Figure 4.9. Path of Waimakariri River circa 1865 (Green et al. 2010).

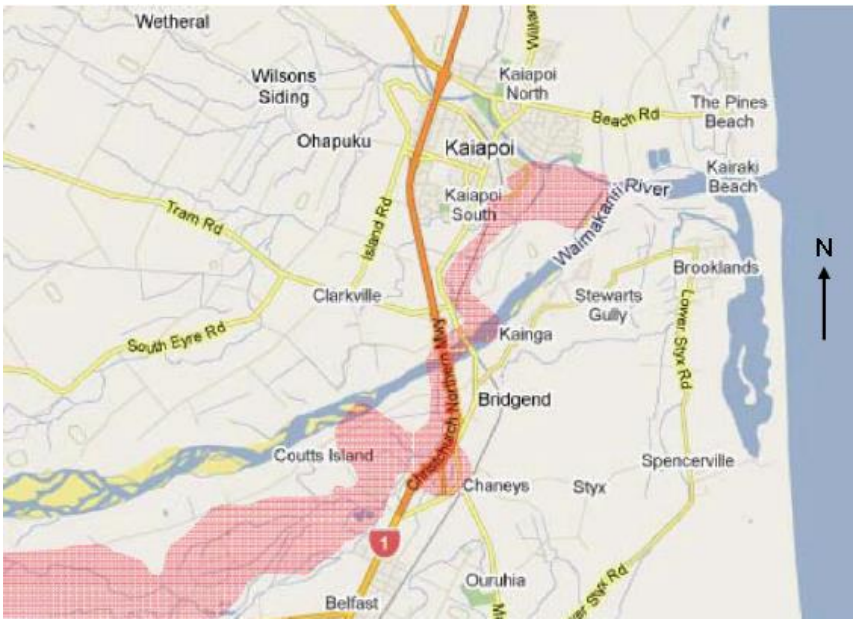

Figure 4.10. Former path of Waimakariri River circa 1865 superimposed on present day Google map of Kaiapoi (Green et al. 2010).

4.4.2 Qualitative Lateral Spreading Observations

Ground observations of liquefaction and lateral spreading were collected in residential areas for the New Zealand Earthquake Commission (Canterbury Geotechnical Database 2013). Observations were organized into three categories: (1) no liquefaction, (2) liquefaction, and (3) liquefaction and lateral spreading. These three categories were subdivided based on severity. A diagram illustrating these categories is shown in Figure 3.15. These observations only account for liquefaction with visible evidence at the surface. Not all properties were assessed before the February 2011 Christchurch Earthquake, so the observations are somewhat incomplete. Despite these uncertainties, the observations provide the best qualitative assessment of the severity of liquefaction across Kaiapoi for comparison to correlation results.

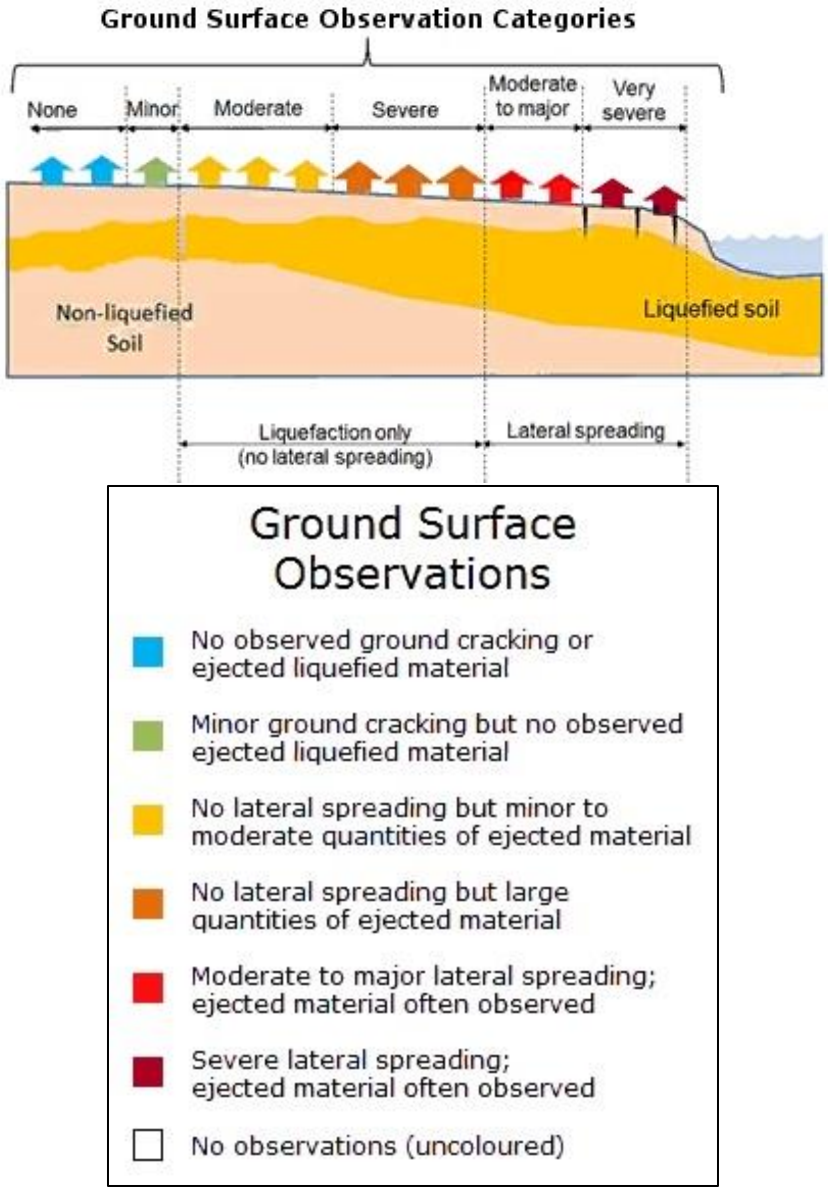

Figure 4.11. Observation categories explained (Canterbury Geotechnical Database 2013).

Figure 4.12 compares the map of observed liquefaction and lateral spreading with amplitudes of displacement from optical image correlation analysis. Observations were

only collected in Kaiapoi and not the surrounding rural areas because only residential properties were assessed. The map of observations indicates the most severe lateral spreading occurred in the corner where two streams meet. In these areas, lateral spreading extended about 100 to 300 m from the waterways. Amplitudes of displacement from the correlation results (Figure 4.12(b)) were calculated by taking the square root of the sum of the squares of the north/south and east/west displacements (i.e. $\sqrt{(N/S\ disp)^2 + (E/W\ disp)^2}$), and displacements less than the precision threshold (0.37 m) were set to zero for visual purposes. Displacements in the residential areas of Kaiapoi are concentrated around the waterways, and the most significant displacement is contained within 300 m of the riverbank. In particular, a large area of coherent displacements is observed in the southeast part of the study area along the north/south stream, and this area corresponds well with the red zone of significant lateral spreading in Figure 1.12(a).

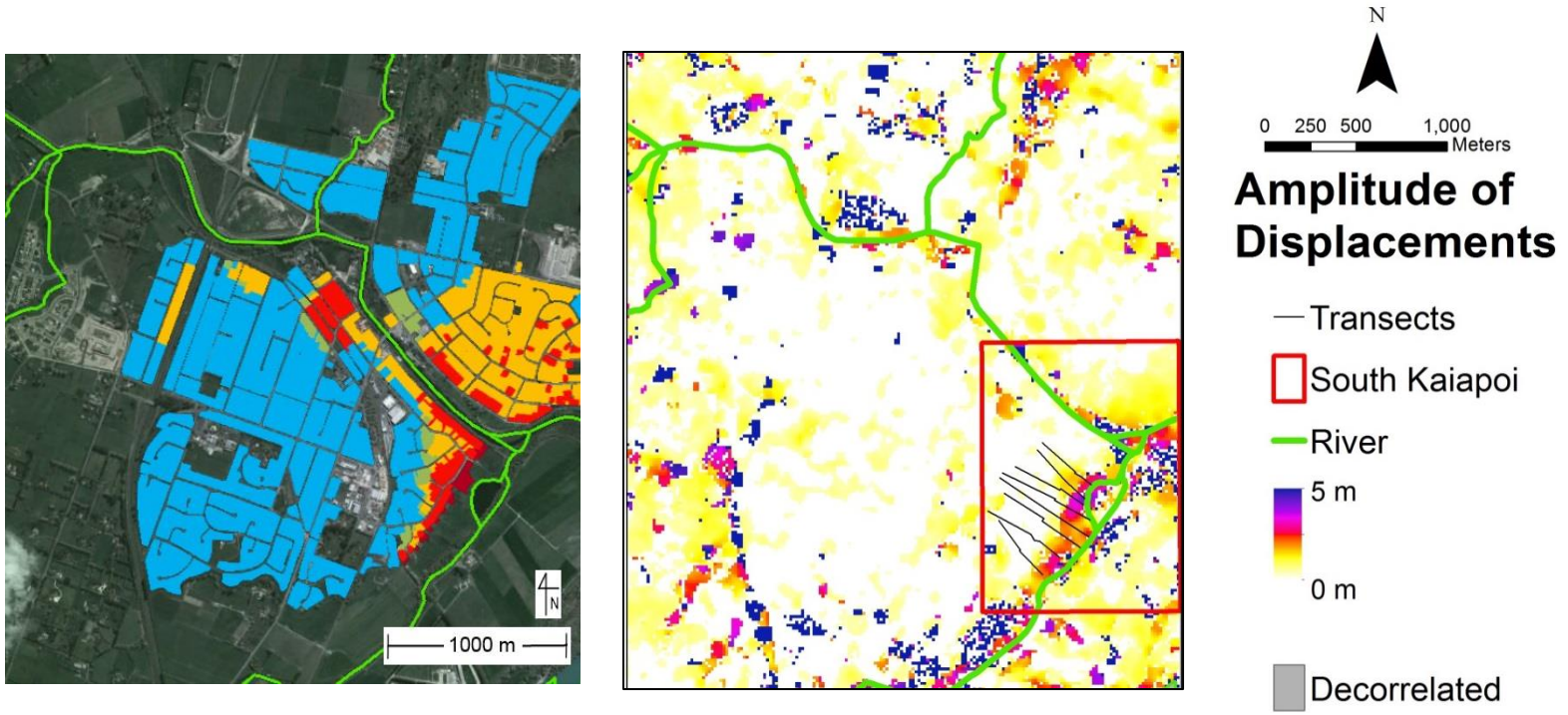

(a) (b)

Figure 4.12. (a) Observed liquefaction and lateral spreading (Canterbury Geotechnical Database 2013) and (b) measured displacement from optical image correlation for South Kaiapoi.

4.4.3 LiDAR Measurements

LiDAR point clouds from before and after the 2010 Darfield Earthquake were compared using a sub-pixel correlation process by Imagin' Labs Corporation and California Institute of Technology (Beavan et al. 2012). This process is similar to the correlation technique used to correlate the optical images. Movements from LiDAR were calculated every 8 m and were averaged to create a grid of measurements every 56 m. The correlation process was significantly affected by elevation errors as the pre-earthquake point cloud is less accurate than the post-earthquake point cloud. Horizontal tectonic movements from GNS Science dislocation models were subtracted from LiDAR measurements to obtain local deformations. Measurements in waterways and areas that were poorly correlated and produced inaccurate measurements were removed. Remaining measurements were rendered as green arrows scaled 56:1 (i.e. an arrow 56 m long represents 1 m of displacement). Displacement arrows from LiDAR were only calculated for the residential areas of Kaiapoi where the infrastructure provided elevation change upon which to correlate.

Figure 4.13 presents the arrows rendered from the LiDAR analysis. Displacements are generally oriented toward the waterways, but significant displacement is recorded throughout much of Kaiapoi. Large displacements are reported well beyond 300 m from the waterways where ground observations reported little to no liquefaction or lateral spreading (see Figure 4.12). Given the poor accuracy of the pre-earthquake point cloud and disagreement between the LiDAR correlation and ground observations, conclusions from comparison of optical image correlation results and LiDAR results must be tempered.

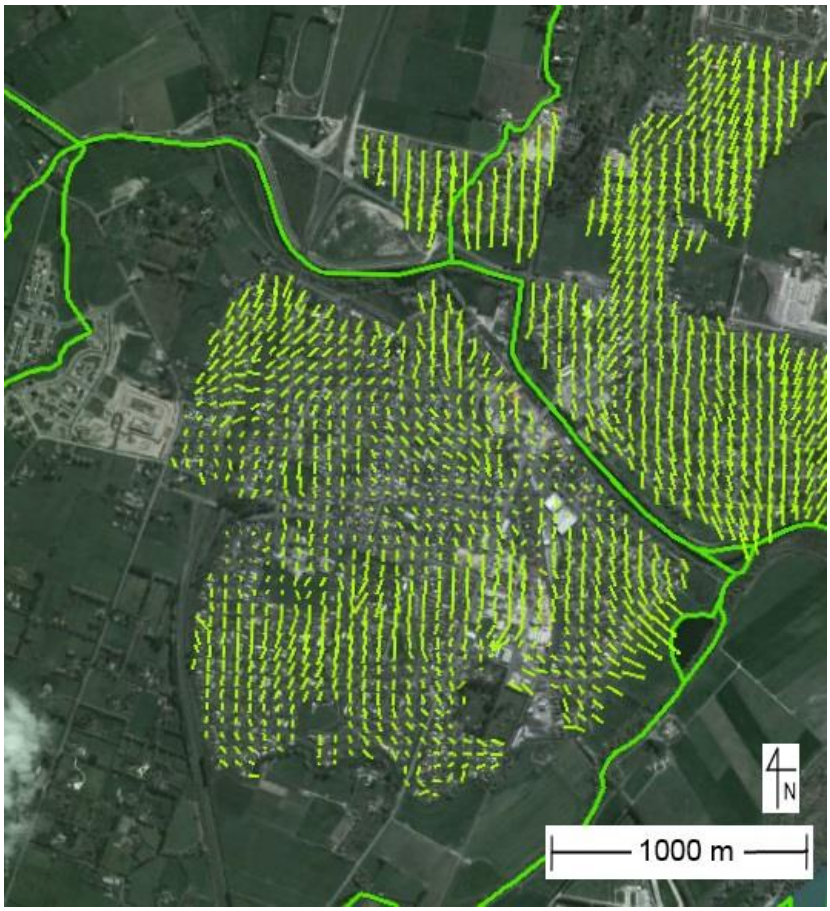

Figure 4.13. Displacements from LiDAR correlation rendered as arrows scaled 56:1 (Beavan et al. 2012).

Optical image correlation results were averaged to create a grid with 64 m spacing. These averaged values were rendered as arrows with a 56:1 scale to allow easy comparison with arrows rendered from LiDAR measurements. Displacements in major waterways were removed for visual clarity. Figure 4.14 shows the arrows rendered from displacement measurements of both LiDAR correlation, as well as from optical image correlation in South Kaiapoi (area outlined in red in Figure 4.4). Optically correlated displacements greater than 0.37 m (precision threshold from the RMSE of the co-

registration) are rendered as yellow arrows, while displacements less than 0.37 m are represented with orange arrows. In the northeastern corner of South Kaiapoi, displacements from both sources are oriented in a south-southwestern direction toward the river. Additionally, both sources show similar displacement patterns on the western side of the northwest/southeast flowing river. However, magnitudes of displacements differ in the two sources. As discussed above, this difference may be explained by the poor quality of the pre-earthquake point cloud used in the LiDAR correlation.

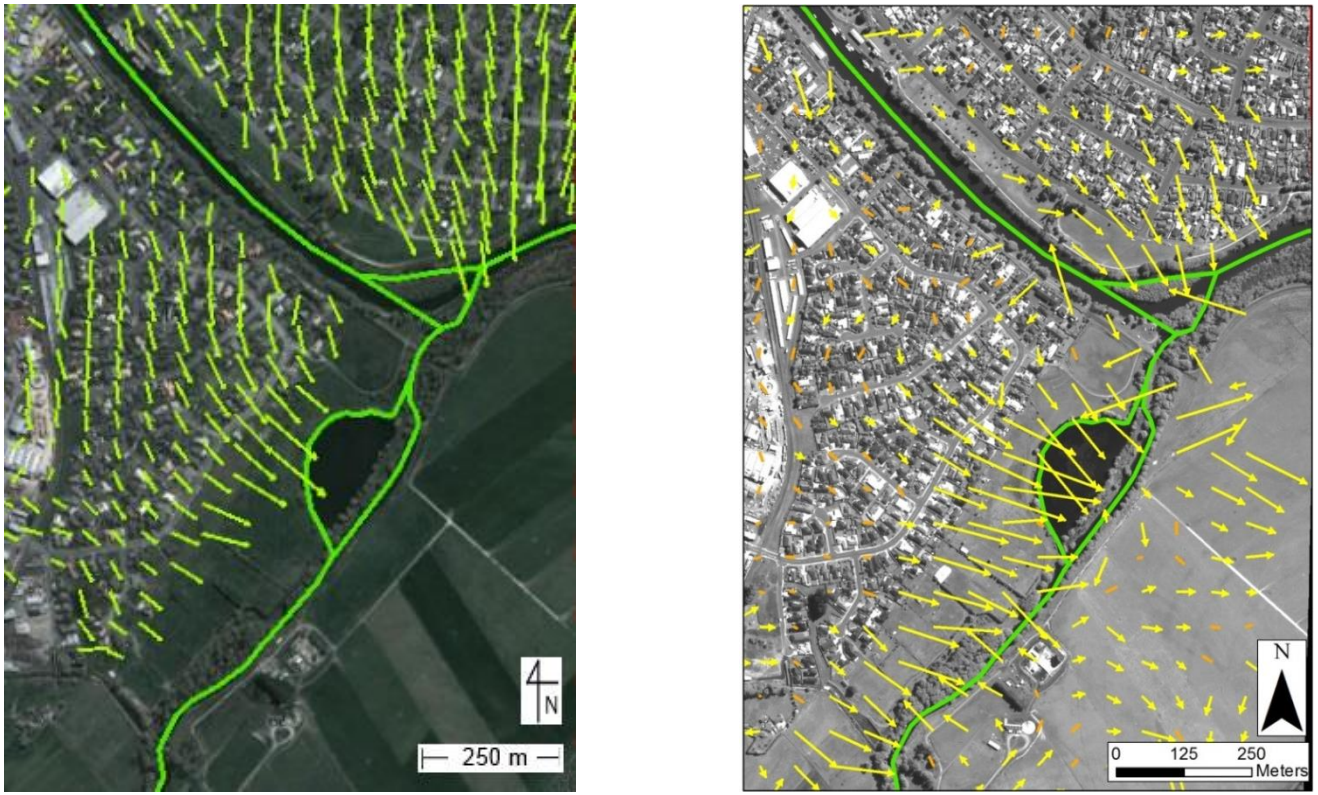

(a) (b)

Figure 4.14. Comparison of displacements from (a) LiDAR correlation (Beavan et al. 2012) and (b) optical image correlation. Displacements less than 0.37 m (precision threshold) are rendered as orange arrows in the optical image correlation results.

4.4.4 Transect Measurements

Robinson et al. (2011) collected displacements along transects in South Kaiapoi by measuring crack widths associated with lateral spreading. Figure 4.15 shows the locations of the transects and cracks measured by Robinson et al. (2011). For most of the transects, the movements were concentrated in a few large cracks found at the same distance from the river, indicating block-type failures as opposed to distributed deformation.

Figure 4.16 shows the locations of six transects overlain on satellite imagery with the amplitudes of displacements from correlation analysis shown. Displacements less than the precision threshold (0.37 m) are not shown for visual purposes. Displacements along each of the six transects were also calculated from the optical image correlation results for comparison with field measurements. Displacements along the transects were computed from the correlation results by sampling measurements every 10 m along each transect. At each sampling point, the displacements of measurements perpendicular to the transect and within 24 m of the transect were averaged to get a representative displacement. An example of the pixels used to estimate displacements along transect KS-13 is shown in Figure 4.17. Each color represents a sampling group of three pixels. From these sampled measurements both the total displacement and the displacement perpendicular to the river were computed. The total displacement amplitude is the magnitude of displacement without regard to direction. The displacement perpendicular to the river is the magnitude of the displacement in the direction parallel to the transect, and negative values represent movement away from the river. If all displacement is

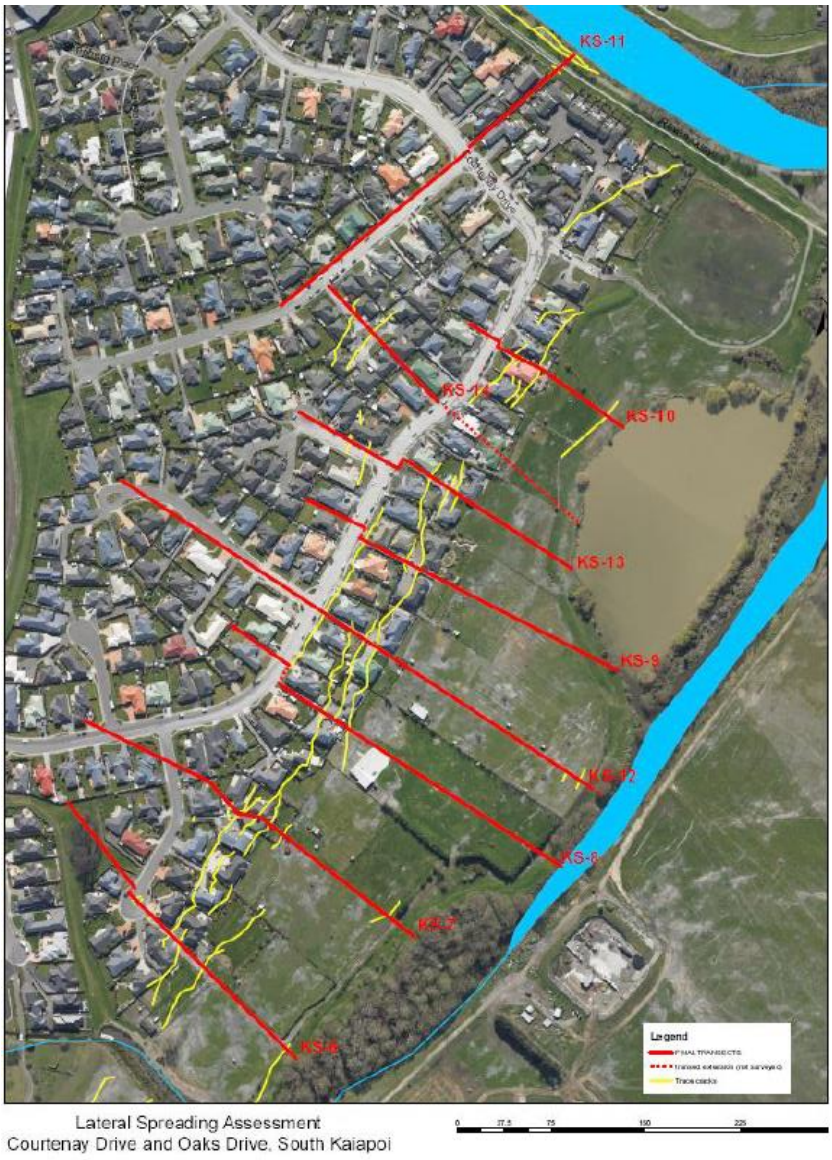

Figure 4.15. Locations of transects (red lines) and measured cracks (yellow lines) from Robinson et al. (2011).

directed along the transect and towards the river, both displacements will be the same. For comparison to the field measurements, displacement along the transect towards the river is more relevant. Transects will be examined individually with displacements from

both ground surveys and correlation results. The transect locations are also shown with the north/south and east/west displacement measurements in Figure 4.6 and Figure 4.7.

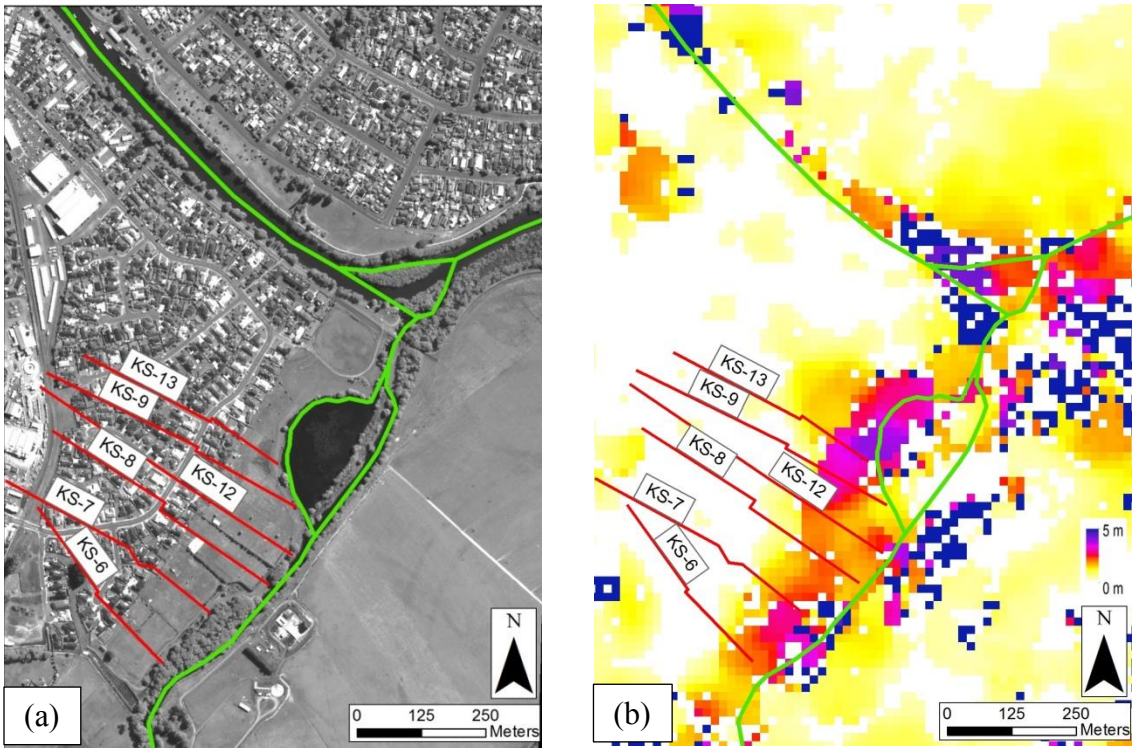

Figure 4.16. Location of transects overlaid on (a) satellite image and (b) amplitudes of displacement measurements from correlation analysis.

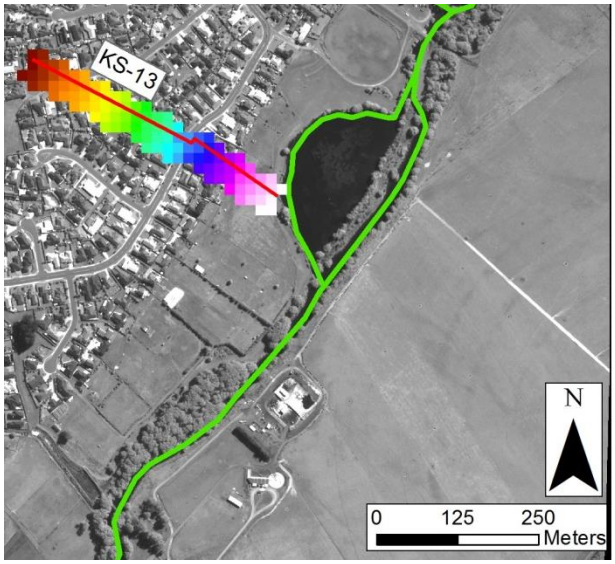

Figure 4.17. Example of correlation displacement sampling for transects. Similar colors represent sample groups.

Figure 4.18 shows displacement with respect to distance from the waterway for transect KS-13. The total-amplitude displacements and perpendicular-to-river displacements follow each other closely indicating nearly all correlated movement along KS-13 is perpendicular to the river. The displacements from the ground survey and the correlation results are distributed similarly, and both show a block-type failure with sharp decreases in displacement over short distances. However, this rapid decrease in displacement occurs in the ground survey data at a distance of about 120 m and at a distance of about 80 m in the correlation data. The displacements at the water's edge also differ in the two data sets, with the ground survey indicating displacement around 2.1 m and the correlation results indicating displacement of 3.2 m. This difference may be the result of the field surveys identifying almost no cracks in the fields between the homes and river (Figure 4.15). The surficial materials in the field may be ductile enough that

cracks did not develop even though there was deformation. Nonetheless, both data sets show that the lateral spread terminates beyond 200 m. The 0.32-0.45 m displacement shown beyond 200 m by the correlation results is close to the precision threshold (i.e. ± 0.37 m), so the lateral spread likely terminates at about 200 m.

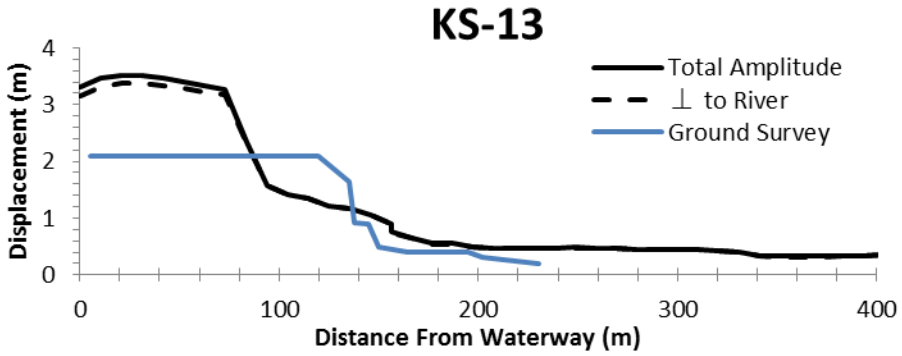

Figure 4.18. Comparison of transect measurements at KS-13 (Ground survey data from Robinson et al. 2011).

Figure 4.19 shows the displacement measurements from the ground survey and correlation results for transect KS-9. The total-amplitude displacements and perpendicular-to-river displacements are nearly identical showing, again, that all measured displacement from the correlation analysis is in the direction of the transect and toward the river. The displacements from both the ground survey and the correlation analysis indicate that the lateral spread deformations terminate about 200 m from the waterway (the displacement of 0.19 m indicated by the correlation results is within the precision threshold of ±0.37 m). Both datasets show a block-type failure as evidenced by the sharp decrease in displacements at about 160-180 m from the waterway. However, displacements within 40 m of the riverbank are different between the two datasets. The ground survey measurements indicate the permanent displacement at the water's edge is 2.5 m and this displacement is constant for a distance of about 160 m. This 160 m

represents the fields between the homes and river, and the absence of cracking in this area may be due to the ductile nature of the surficial materials. The correlation results show a displacement of 1.1 m at the river, and a peak displacement of 3.0 m about 100 m from the river. This pattern of displacement may be due to smoothing effects within the correlation window (128x128 m) that extends across the river where displacements are small or even in the other direction. This smoothing would lead to a measured displacement in between the largest and smallest displacements within the window, like an average.

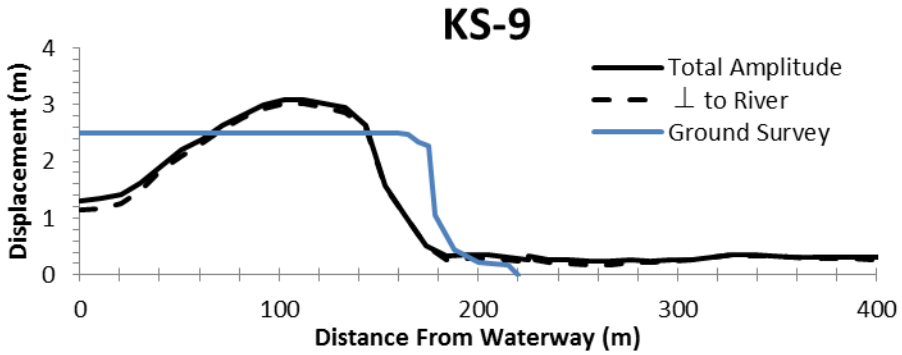

Figure 4.19. Comparison of transect measurements at KS-9 (Ground survey data from Robinson et al. 2011).

Figure 4.20 compares the displacement measurements for transect KS-12. Total amplitude displacements and displacements perpendicular to the river are similar showing that all measured displacement is along the transect and toward the river. The measurements from the correlation analysis agree well with those from the ground survey. Both datasets show a block-type failure in which the lateral spread displacements terminate around 200-250 m from the river. Displacements near the water's edge are also similar. The ground survey results indicate permanent displacement at the riverbank of

about 2.7 m, and correlation results show a permanent displacement of 2.3 m. This difference is within the precision threshold for the correlation analysis.

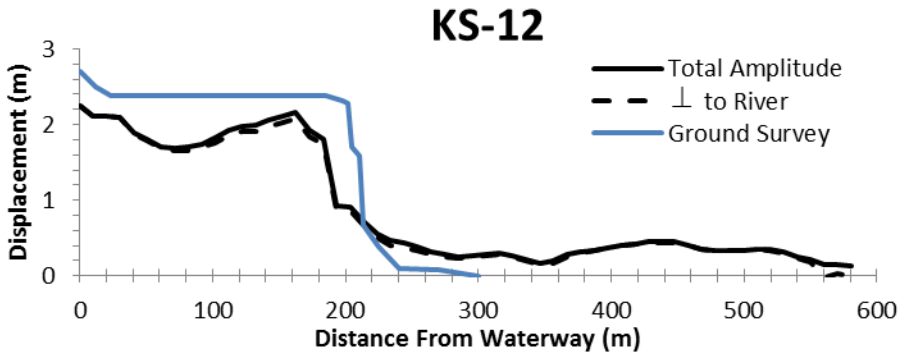

Figure 4.20. Comparison of transect measurements at KS-12 (Ground survey data from Robinson et al. 2011).

Displacement measurements along transect KS-8 are presented in Figure 4.21. Again, the total amplitude displacements and displacements perpendicular to the river match closely indicating all displacement is toward the waterway and along the transect. Both displacement datasets indicate the lateral spread terminates around 250 m from the waterway, the distribution of displacements is somewhat similar in both datasets, and the permanent displacement at the water's edge is nearly the same (~1.6 m).

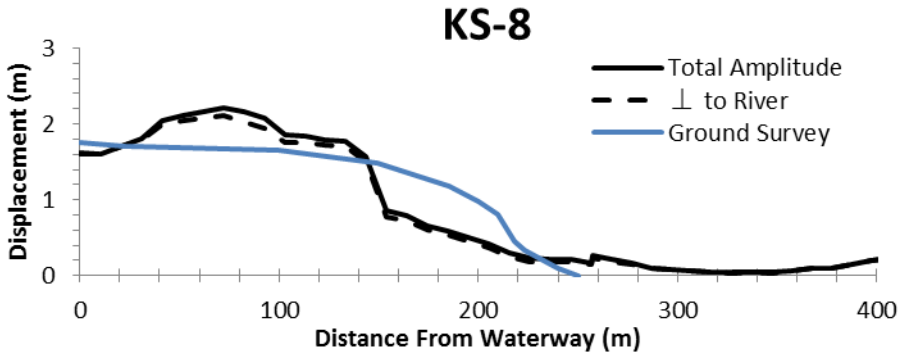

Figure 4.21. Comparison of transect measurements at KS-8 (Ground survey data from Robinson et al. 2011).

Figure 4.22 shows the displacement measurements for transect KS-7. For KS-7, the location of the waterway is taken as the small creek east of the grove of trees in Figure 1.15. Displacements within 50 m of the river measured by the correlation analysis are not included since measurements in this area were very noisy due to the trees. Total-amplitude and perpendicular-to-river displacements are similar for the correlation results indicating all movement is toward the river and along the transect. The ground survey indicates the lateral spread terminates abruptly at about 200 m from the riverbank, but the correlation results show the lateral spread terminating about 170 m from the waterway. The ground survey shows no additional displacement (i.e., cracks) within 180 m of the river, despite the fact that ejecta was observed within this zone which corresponds with the fields beyond the homes (Figure 4.15). The correlation results show a more distributed pattern of deformation within this zone, which may indicate that the surface soils were ductile enough to sustain movement without cracking. As a result, the permanent displacement at the water's edge from the correlation analysis (2.7 m) is much larger than the corresponding displacement from the ground survey (1.3 m).

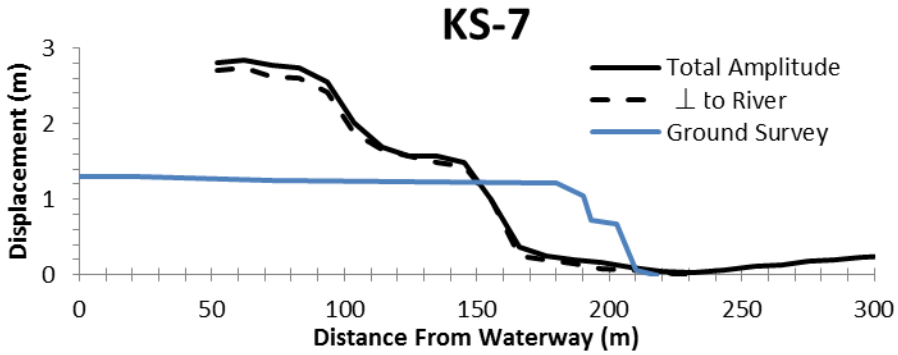

Figure 4.22. Comparison of transect measurements at KS-7 (Ground survey data from Robinson et al. 2011).

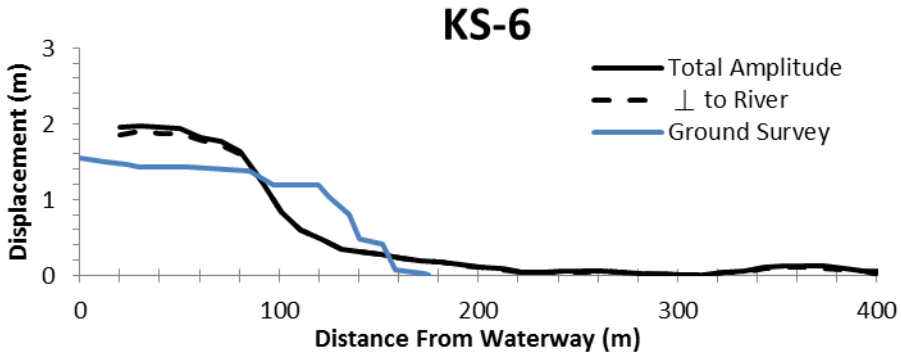

Figure 4.23. Comparison of transect measurements at KS-6 (Ground survey data from Robinson et al. 2011).

Figure 4.23 presents the displacement measurements along transect KS-6. Again, the location of the waterway is taken as the small creek east of the grove of trees in Figure 1.15. Displacement measurements from correlation analysis were excluded within 20 m of the river due to excessive noise in the measurement due to the trees. Also, total-amplitude and perpendicular-to-river displacements are similar indicating all recorded displacement from the correlation analysis is toward the river and along KS-6. Both the correlation results and ground survey results show displacements of about 1.5-1.8 m at the water's edge. This displacement decreases significantly at a distance of about 90 m for the correlation analysis and 120 m for the ground survey.

Chapter 5: Optical Image Correlation Analysis of Lateral Spread Displacements in Katori, Japan from the 2011 Tohoku Earthquake

5.1 INTRODUCTION

This chapter discusses the use of optical image correlation to measure liquefaction-induced deformation in the town of Katori, Japan on the Tone River caused by the 2011 Tohoku Earthquake. Section 5.2 introduces the earthquake and region of study in a broad context. Section 5.3 discusses the image selection and correlation process. Finally, Section 5.4 presents the results and compares them to former river channel locations and horizontal deformation patterns measured using other sources of data.

5.2 THE 2011 TOHOKU EARTHQUAKE

On March 11, 2011, a magnitude 9.0 (M_w) megathrust earthquake struck off the coast of Japan. This earthquake was the fifth largest ever recorded and caused more than 20,000 deaths and an estimated $210 billion in damages (Pradel et al. 2014). Although many of the casualties and damage were directly related to the tsunami caused by the earthquake, observed damage along the Tone River was primarily due to liquefaction and lateral spreading. Specifically, severe lateral spreads were observed in the town of Katori along the Tone River (Pradel et al. 2014). Figure 5.1 shows the location of the earthquake fault rupture relative to the area of study around Katori (green box), and the photos in Figure 5.2 represent some lateral spreading damage observed in Katori.

The Tone River flows through a deep sedimentary basin which has been shown to amplify strong motions in past earthquakes (Pradel et al. 2014). Due to anthropogenic

adjustments of the Tone River, parts of Katori rest upon former river channels of the Tone River (Pradel et al. 2014). Deposition of these materials is estimated to have occurred less than 500 years ago. Coupled with a shallow water table, coarse grained materials in Katori allow favorable conditions for liquefaction to occur. However, older coarse grained materials far from Tone River are thought to have become resistant to liquefaction.

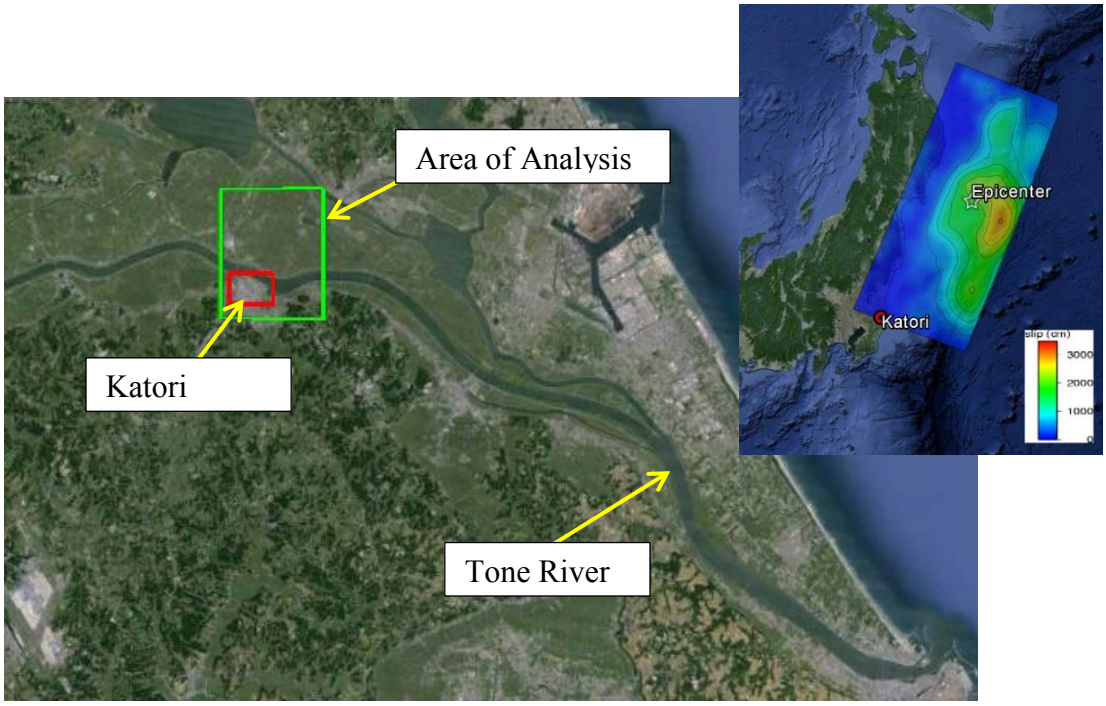

Figure 5.1. Location of Tohoku earthquake fault rupture from Wei et al. (accessed 2014), and the Katori study area shown on Google Earth image (2014).

Figure 5.2. Photos showing damage from lateral spreading in Katori, Japan (Ashford et al. 2011).

5.3 IMAGE SELECTION AND PROCESSING

Based on reports of liquefaction-induced deformation around the town of Katori and availability of satellite imagery, panchromatic (i.e. grayscale) 0.5-m resolution images from WorldView-1 were selected from before the earthquake (December 24, 2010) and after the earthquake (December 11, 2011). Figure 5.3 shows the pre-event satellite image used in the correlation analysis with Katori outlined in red. This area consists of the populated Katori area to the south of the river, agricultural fields north of the river, and some hills to the south of Katori. The acquisition geometry was agreeable in the two images with the pre- and post-event images having target azimuth angles of 15.1° and 15.4° and off-nadir angles of 13.3° and 11.7°, respectively.

By using equations 2.1, 2.2, and 2.3 and assuming a pseudo-suborbital path of 0° (i.e. $\theta_0 = 0$), north/south look angles (T) of 12.86° and 11.29° and east/west look angles (S) of 3.52° and 3.14° can be established for both the pre- and post-event image, respectively. The difference in the north/south look angles is 1.57°, and the difference in the east/west look angles is 0.38°. Since these differences are small for both directions, significant noise is not expected to occur from differences in acquisition angles.

Images were orthorectified with ENVI software (ENvironment for Visualizing Images, ENVI 2014) using a 90-m resolution digital elevation model (DEM) from the Shuttle Radar Topography Mission (SRTM, USGS 2004). Tie points were automatically generated using ENVI, and tie points were assessed in the same way as presented in previous chapters. Points within 200 m of major waterways were removed, and points with high residuals relative to the warping polynomial were excluded from use in co-registration. Ultimately, 2,272 tie points (77 points per km^2) with an RMSE of 0.30 m with respect to the warping polynomial were selected for co-registration. Figure 5.4

shows the tie points selected for use in co-registration with their residuals from the warping polynomial represented by color. Notice the larger density of tie-points identified south of the river in the populated areas, where there are more features upon with to identify tie-points. It was more difficult to identify a large number of tie points in the agricultural fields to the north of the river.

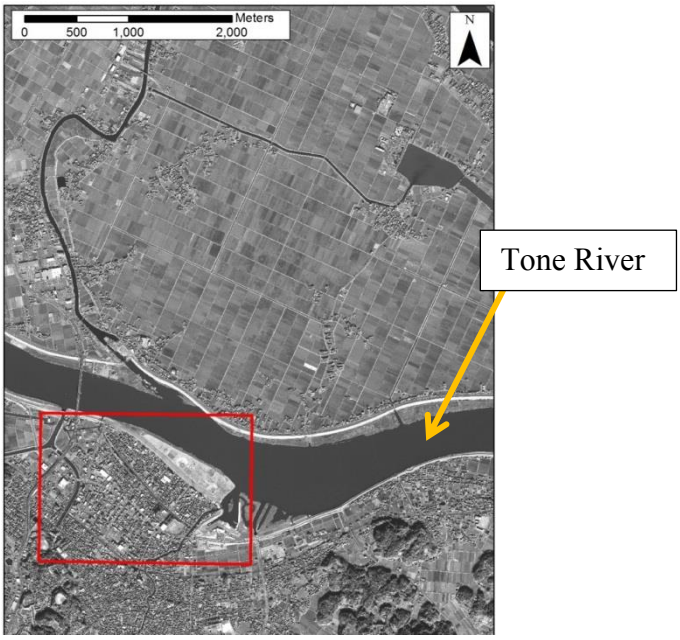

Figure 5.3. Pre-earthquake image; Katori outlined in red.

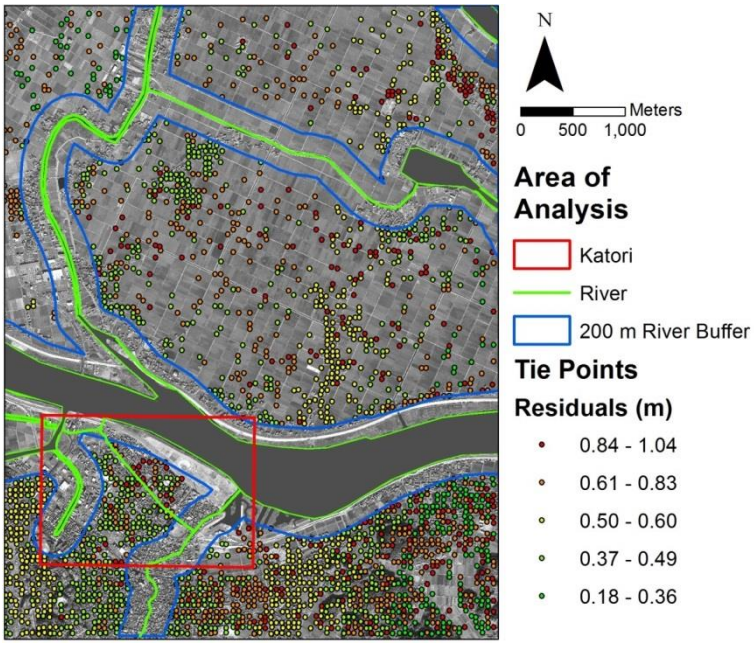

Figure 5.4. Tie points used in co-registration.

Following co-registration, correlation analysis was performed using the method presented by Leprince et al. (2007). A window size of 256 pixels (128 m) was used with a step size of 64 pixels, producing a displacement measurement every 32 m. This window size is larger than used in the analyses for Christchurch because, like the area of around the town of Kaiapoi, the area around Katori is predominately used for agriculture and has homogenous texture. Results were filtered such that measurements with a signal-to-noise ratio (SNR) less than 0.95 were designated "decorrelated". A precision threshold of 0.30 m was established from the co-registration RMSE.

5.4 Deformation Results and Comparisons

Displacement measurements of horizontal deformation were calculated for the north/south and east/west directions. Figure 5.5 presents the north/south displacements in the region of study. Displacements less than the precision threshold (0.30 m) were set to

zero for visual purposes. Northward movements are represented by yellow/red with red indicating displacements in excess of 2 m. Similarly, southward movement is represented by blue/purple with purple indicating displacements in excess of 2 m. In Katori (red box), coherent zones of horizontal deformation are indicated. The southern riverbank of the Tone River displaced northward, while areas on the north side of the small canal running through the middle of the town of Katori displaced southward. Additionally, areas adjacent the tributary north of Katori show large displacement. Areas far from the Tone River and major waterways show little to no coherent horizontal deformation.

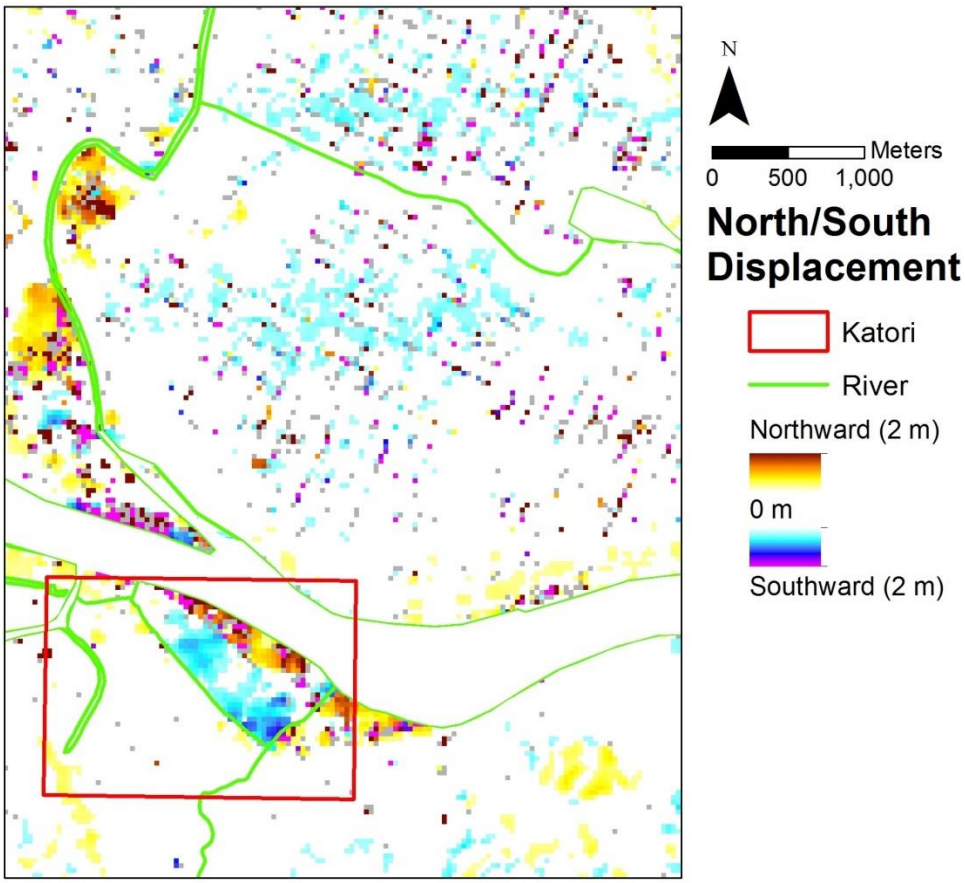

Figure 5.5. North/south displacements from correlation analysis.

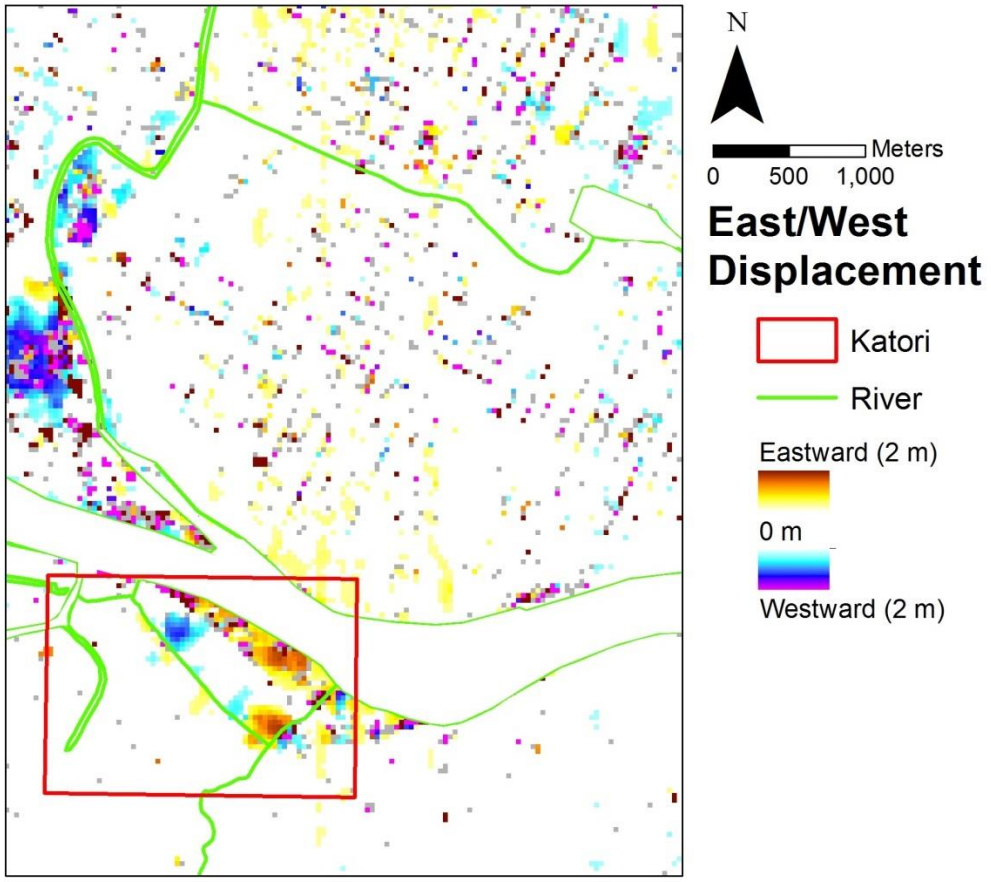

Figure 5.6. East/west displacements from correlation analysis.

Figure 5.6 presents the measured displacements in the east/west direction. Displacements less than the precision threshold (0.30 m) were set to zero for visual purposes. Again, coherent deformation patterns are seen in Katori between the canal running through the middle of Katori and the Tone River. The southern riverbank of the Tone River displaces eastward, which is consistent with displacement perpendicular to the river where the river is slightly oriented northwest/southeast. For the canal running through the town of Katori, displacements toward the west are measured along one section towards the canal's western end. Near its eastern end where the canal meets a stream flowing to the north, eastward displacement toward the stream is observed. To the

north of the Tone River in the western part of the image, a coherent pattern of large displacement is oriented westward, away from the tributary. In areas far from major waterways, little to no displacement is measured.

5.4.1 Former River Channel

Although the Tone River flows near Katori today, it has not always done so. Beginning in the 1600s, many canals were constructed and river channels diverted to facilitate trade to Tokyo (Pradel et al. 2014). During this time, the path of the Tone River was altered such that it flowed eastward into the Pacific Ocean. This alternation is responsible for much of the loose sediment fill placed in and around present-day Katori.

Figure 5.7. (a) 1880's shoreline from Pradel et al. (2014) superimposed on present-day satellite image and (b) displacement amplitudes from correlation analysis superimposed on satellite image (Google Earth 2014).Figure 5.7 compares the shoreline from the 1880s with satellite imagery of the area today and the displacement amplitudes from the correlation analysis. Today, much of Katori rests upon the former path of the Tone River, as indicated by the location of the 1880s shoreline shown in Figure 5.7(a). Consequently, much of Katori is susceptible to liquefaction (and thus lateral spreading). Figure 5.7(b) shows the displacement amplitudes from the correlation analysis superimposed on the Google earth image that shows the 1880s shoreline. The displacement amplitudes were calculated by taking the square root of the sum of the squares of the directional displacements (i.e., $\sqrt{NS^2 + EW^2}$), and measurements less than the precision threshold were not included for visual purposes. Significant displacement is well bounded by the former shoreline of the Tone River with nearly all lateral spreading occurring within the location of the former river channel. Therefore,

displacement measurements qualitatively agree that lateral spreading occurred within these areas most susceptible to liquefaction and lateral spreading.

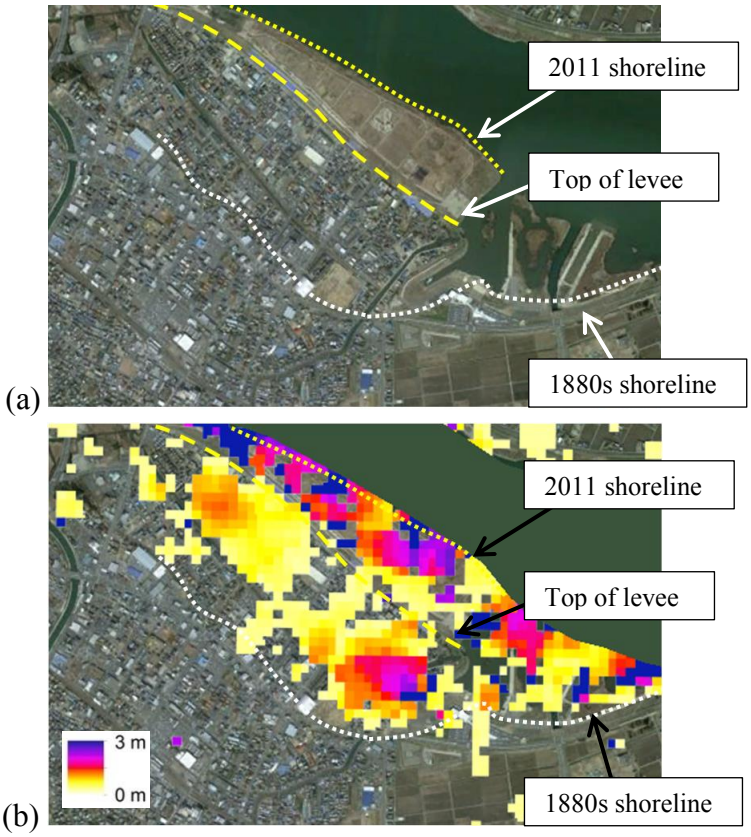

Figure 5.7. (a) 1880's shoreline from Pradel et al. (2014) superimposed on present-day satellite image and (b) displacement amplitudes from correlation analysis superimposed on satellite image (Google Earth 2014).

5.4.2 Ground Observations

From personal communication with Teruo Nikai, Professor of Civil Engineering at the Nagoya Institute of Technology in Japan, measurements of liquefaction-induced horizontal deformation in Katori were obtained. These measurements were collected for the city of Katori and were used to study liquefaction countermeasures. Measurements

were digitized and rendered as vectors scaled 1:50 (i.e. an arrow of 50 m length represents 1 m of horizontal displacement). Displacements from the correlation analysis were also rendered as arrows scaled 1:50 for visual comparison. Displacements below the precision threshold (0.30 m) are excluded for visual clarity.

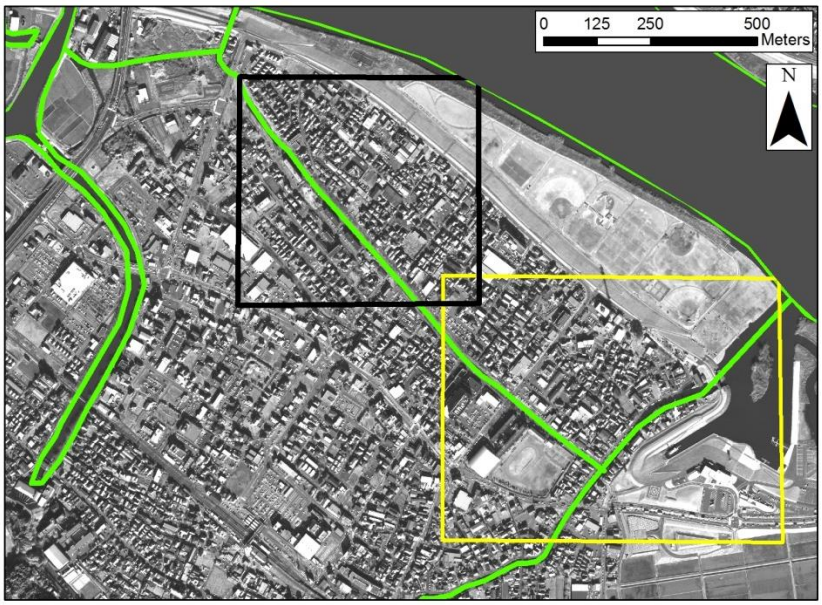

Figure 5.8. Locations of areas of comparison within the town of Katori.

Measurements will be presented in two areas for ease of comparison. Figure 5.9 displays the locations of the two areas. Vectors in the area outlined in black are shown in Figure 5.9(a) along with the location of the canal. North of the canal, displacements from both sources agree in magnitude (~ 1 m) and direction (south and southwest). South of the canal, vectors from ground measurements are oriented northward toward the canal, but vectors from the correlation analysis are oriented southward. This difference may be due to smoothing effects in the correlation analysis due to the use of a large correlation

window (128 m by 128 m). Vectors in the area outlined in yellow in Figure 5.9 are presented in Figure 5.9(b). Vectors are more agreeable in this area. Displacements from both sources have similar magnitude and direction (eastward).

.

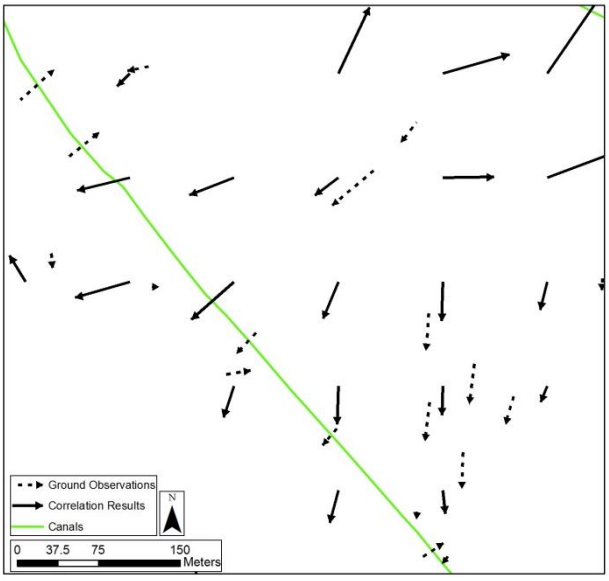

(a)

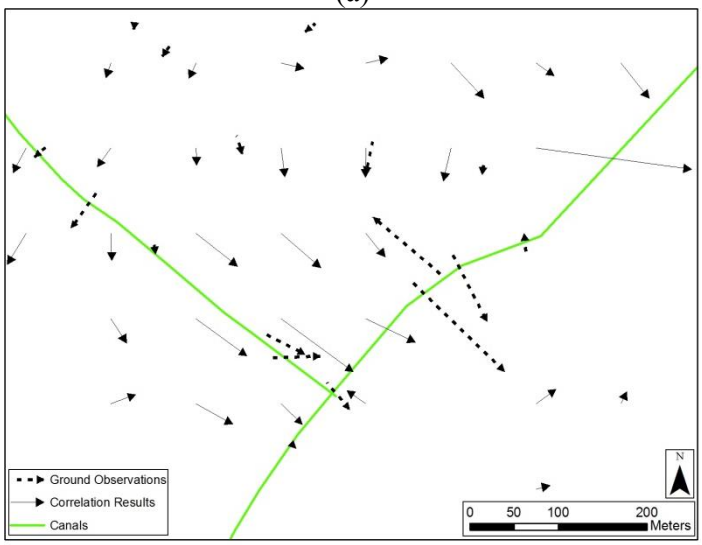

(b)

Figure 5.9. Displacement vectors from ground surveys by the City of Katori (personal communication with Teruo Nikai) and correlation analysis in (a) western Katori and (b) eastern Katori. Vectors scaled 50:1.

Chapter 6: Summary and Conclusions

6.1 Summary and Conclusions

Liquefaction-induced deformations associated with lateral spreading represent a significant earthquake hazard that can cause substantial damage during earthquakes. The ability to accurately predict lateral-spreading displacement is hampered by a lack of field data from previous earthquakes. Remote sensing via optical image correlation can fill this gap and provide data regarding liquefaction-induced lateral spreading displacements.

Liquefaction-induced horizontal deformations were measured using optical image correlation. Specifically, 0.5-m resolution, panchromatic satellite image pairs were analyzed for three earthquakes, the 2011 Christchurch Earthquake in New Zealand, the 2010 Darfield (Canterbury) Earthquake in New Zealand, and the 2011 Tohoku Earthquake in Japan. For each study area, the deformations from optical image correlation were compared with available geology, as well as ground observations of liquefaction and its effects.

For the Christchurch earthquake, optical image correlation was applied to the neighborhoods along the Avon River to the northeast of the Christchurch Central Business District. Horizontal deformation patterns from optical image correlation were concentrated around the Avon River. Most displacement patterns occurred within 300 m of the Avon River, but some coherent patterns extended beyond 500 m from the riverbank, specifically in the Avondale and New Brighton areas. These coherent patterns of displacement generally corresponded with clean alluvial sand deposits and were bounded by dirty marine sand deposits. Further, the location of displacement patterns showed a strong correlation to the former channels of the Avon River.

Comparing the displacements from the correlation analysis with field observations, areas with large displacements generally occurred in areas with observed lateral spreading and deformation patterns which extended far beyond the Avon River were typically contained within areas of observed liquefaction. Additionally, the most severe lateral spread displacements were well bounded by observed crack patterns. LiDAR measurements of displacement agreed well with the correlation results, even in the areas of displacement further from the river which were not identified in other field observations. Finally, ground survey measurements along ten transects were quantitatively compared to measurements from optical image correlation. While the degree and nature of similarity between the ground survey measurements and those from image correlation differed in each transect, measurements along most transects were agreeable.

For the Darfield earthquake, the town of Kaiapoi along the Kaiapoi River was analyzed. Acquisition angles were generally similar in the pre- and post-event images. However, the difference in angles describing the line-of-sight in the east/west direction for pre- and post-event images were much greater than the difference in angles describing the line-of-sight in the north/south direction. Thus, the correlation process produced east/west displacements with more noise than those in the north/south direction.

Coherent displacement patterns from optical image correlation were concentrated around the Kaiapoi River and its tributaries, and these patterns generally terminated within 300 m of these waterways. The correlation process was more effective in the populated areas around the town of Kaiapoi than in the surrounding agricultural regions. The optical image correlation analysis measured significant displacement in the areas which liquefied in the previous 1901 Cheviot Earthquake. Additionally, most coherent

displacement patterns southwest of South Kaiapoi occurred within the abandoned river channel and within areas of reported severe lateral spreading and liquefaction. The displacement patterns from LiDAR were similar to those from the correlation analysis, but the magnitudes of displacement differed. Much of the difference may be explained by poor pre-event LiDAR data. Finally, the correlation results and ground survey measurements along transects both showed block-type failures along all the transects, with sharp decreases in displacement with respect to distance from the river. However, the two sources tended to differ in displacements at the riverbank. These differences may be attributed to smoothing effects from using a large correlation window or the possible ductile nature of the surficial materials near the river.

For the Tohoku earthquake, the town of Katori along the Tone River was analyzed. Pre- and post-earthquake images shared similar acquisition angles, but the acquisition angles compared better in the east/west direction than in the north/south direction. Displacement patterns from the optical image correlation analysis were concentrated on the southern riverbank of the Tone River in the town of Katori and north of the canal which runs parallel to the Tone River and through the town of Katori. Some coherent patterns of displacement were detected along a tributary to the north of the Tone River as well. Little to no displacement was measured far from the Tone River and other major waterways. Comparison of the correlation results with the historical path of the Tone River revealed a strong correlation between areas of significant displacement and the location of the Tone River in the 1880s. Specifically, nearly all coherent patterns of displacement near the town of Katori occurred within the land reclaimed from the Tone River. Correlation results were also compared to measured horizontal deformation patterns in the town of Katori collected for the City of Katori. Correlation results

generally agreed with horizontal deformation measurements in both direction and magnitude. However, some measurements differed from correlation results largely due to smoothing effects from using a large correlation window.

Overall, the displacement patterns from optical image correlation compared favorably with all sources of comparison for all three earthquakes. Correlation results matched sources of comparison better in areas with more features or heterogeneous texture (e.g. urban areas) than in areas with few features and homogeneous texture (e.g. agricultural fields). Typically, large-scale displacement patterns were more easily discernable in correlation results than in other sources of lateral spreading measurements.

While a sub-pixel precision threshold (i.e., less than 0.5 m) was achieved for all three correlation analyses, many factors contributed the quality of correlation results. Agreement of acquisition angles between the two images being analyzed had the greatest effect on the correlation results. Where acquisition angles differed more significantly, false matches were more likely to occur during the correlation process, and thus, the displacement results tended to have more noise. Co-registration errors largely controlled the precision of measurements. Specifically, the RMSE of the tie points with regard to the warping polynomial dominated other sources of error, and this RMSE was found to be a reliable predictor of measurement precision. Tie points were more easily identified in areas with many features or heterogeneous texture. For example, more tie points tended to be generated in urban areas than in agricultural fields.

In addition to tie point generation, the correlation process was affected greatly by the texture of the area. False matches were more likely in areas with few features and homogeneous texture. Thus, the correlation process performed more reliably in areas with many features and heterogeneous texture. Additionally, false matches were more

common when a smaller correlation window was used because fewer distinguishable features were encompassed in the correlation window. Thus, analyses with a smaller correlation window produced more noise than with a larger window. However, a trade-off exists in correlation window size. Displacements from correlation analysis were somewhat averaged or smoothed over the correlation window. If a large correlation window encompassed areas that displaced both a large amount and a small amount, the correlation analysis would yield a displacement measurement in between the two displacement magnitudes. Therefore, to measure more localized/discrete deformation patterns a smaller correlation window is required. Thus, the smallest correlation window which produces an acceptable level of noise was preferred.

6.2 Recommendations for Future Work

Given the favorable performance of optical image correlation in measuring horizontal displacements, measurements from optical image correlation would provide a suitable means to create an accurate and diverse database of lateral spread displacements. This database could be used to study the complex mechanics of lateral spreading and improve theoretical understanding of these mechanics. Additionally, this database could be used to calibrate existing empirical models and create new, more comprehensive empirical models that would predict the likelihood of lateral spreading and severity of lateral spreading given an earthquake. These models are of significant value given their use in determining options to mitigate lateral spreads. Without an accurate predictive model, design requirements for structures are difficult to determine, and if the effects of lateral spreading are under predicted, costly damage or even loss-of-life may occur. Additionally, designs may be overly conservative if predictive models are inaccurate or

unreliable. In many cases, strengthening the structural design may be significantly more economic than ground improvement. However, determining which option is preferred is highly dependent on accurate lateral spread prediction. With measurements from optical image correlation, empirical models could be made more reliable and accurate for use in design and decision making.

Even with the level of precision and agreement achieved in the studies of this thesis, future work exists for improving the optical image correlation process. Since errors in the co-registration process largely control the level of precision achievable with optical image correlation, much work remains to improve the co-registration process. This process could be improved with better algorithms and methods for automatically generating tie points. Generally, the more tie points available to assess for co-registration, the more likely the final selected tie points will be appropriate, and thus, the co-registration RMSE will be lower. The co-registration process could be improved with better methods of evaluating tie point quality as well. Generally, if tie points are better distributed throughout the area of study, distortions are less likely to affect correlation results (e.g., artifacts from misaligning of image strips will be less prevalent). If the residual of each tie point is used to evaluate its quality as well, then the co-registration and correlation process could be iterated such that no tie points within areas of coherent displacement are included in co-registration.

References

Ashford, Scott A., Ross W. Boulanger, Jennifer L. Donahue, and Jonathan P. Stewart. *Geotechnical Quick Report on the Kanto Plain Region during the March 11, 2011, Off Pacific Coast F Tohoku Earthquake Japan*. Rep. no. GEER-025a. N.p.: Geotechnical Extreme Events Reconnaissance (GEER), Apr. 2011.

Beavan, J., Levick, S., Lee, J. and Jones, K. "Ground displacements and dilatational strains caused by the 2010-2011 Canterbury earthquakes" *GNS Science Consultancy Report* 2012/67. p. 59. (2012).

Bethel, J. Purdue University, n.d. Web. 20 Feb. 2014. <https://engineering.purdue.edu/~bethel/elem3.pdf>.

Berrill, J. B., P. C. Mulqueen, and E.T.C. Ool. "Liquefaction at Kaiapoi in the 1901 Cheviot New Zealand Earthquake." *Bulletin of the New Zealand National Society for Earthquake Engineering* 27.3 (Sept 1994): 178-89.

Binet, R. and L. Bollinger. "Horizontal Coseismic Deformation of the 2003 Bam (Iran) Earthquake Measured from SPOT-5 THR Satellite Imagery." *Geophysical Research Letters* 32.2 (2005).

Bukata, R. P. Optical Properties and Remote Sensing of Inland and Coastal Waters. Boca Raton, FL: CRC, 1995. 76-79. Print.

Brown, L. J., and J. H. Weeber. *Geology of the Christchurch Urban Area, Scale 1: 25000*. Lower Hutt, N.Z.: Institute of Geological & Nuclear Sciences, 1992. 1. Print.

Caee.utexas.edu. “Evaluation of Integrated Seismic Hazards & Ground Failure in Pull-Apart Basins during The Izmit Earthquake In Turkey.” Web. 13 Dec. 2013. http://www.caee.utexas.edu/prof/rathje/research/turkey.html

Canterbury Geotechnical Database (2012) "Horizontal Ground Surface Movements", Map Layer CGD0700 - 23 July 2012, retrieved Feb 15 2014 from https://canterburygeotechnicaldatabase.projectorbit.com/

Canterbury Geotechnical Database (2012) "Observed Ground Crack Locations", Map Layer CGD0400 - 23 July 2012, retrieved Oct 21 2013 from https://canterburygeotechnicaldatabase.projectorbit.com/

Canterbury Geotechnical Database (2013) "Liquefaction and Lateral Spreading Observations", Map Layer CGD0300 - 11 Feb 2013, retrieved Feb 15 2014 from https://canterburygeotechnicaldatabase.projectorbit.com/

Casson, B., C. Delacourt, D. Baratoux, and P. Allemand. "Seventeen Years of the “La Clapière” Landslide Evolution Analysed from Ortho-rectified Aerial Photographs." *Engineering Geology* 68.1-2 (2003): 123-39. Print.

Cubrinovski M, Bradley B, Wotherspoon L, Green R, Bray J, Wood C, Pender M, Allen J, Bradshaw A, Rix G, Taylor M, Robinson K, Henderson D, Giorgini S, Ma K, Winkley A, Zupan J, O’Rourke T, DePascale G, Wells D. “Geotechnical aspects of the 22 February 2011 Christchurch earthquake.” *Bulletin of the New Zealand Society for Earthquake Engineering* 44.4 (2011): 205-226.

Debella-Gilo, Misganu, and Andreas Kääb. "Measurement of Surface Displacement and Deformation of Mass Movements Using Least Squares Matching of Repeat High Resolution Satellite and Aerial Images." *Remote Sensing* 4.1 (2012): 43-67. Print.

EERI. "The M W 7.0 Haiti Earthquake of January 12, 2010: Report #1." EERI Special Earthquake Report April. 2010 Web.

EXELIS. "Warp and Resample." *Warp and Resample (Using ENVI) | Exelis VIS Docs Center*. N.p., n.d. Web. 23 Aug. 2013. <http://www.exelisvis.com/docs/warpingresampling.html>.

ENVI version 4.8. Exelis Visual Information Solutions, Boulder, Colorado. Used 2014.

Gao, Feng, Jeffrey Masek, and Robert E. Wolfe. "Automated Registration and Orthorectification Package for Landsat and Landsat-like Data Processing." *Journal of Applied Remote Sensing* 3.1 (2009)

GDAL. 2012. GDAL - Geospatial Data Abstraction Library: Version 1.9.2, Open Source Geospatial Foundation, http://gdal.osgeo.org

Glaser, S. D. "Estimation of Surface Displacements Due to Earthquake Excitation of Saturated Sands." Earthquake Spectra 10.3 (1994): 489. Print.

Google Earth (Version 7.1.2.2041), accessed 2014.

Green, R., Cubrinovski, M., Allen, J., Ashford, S., Bowman, E., Bradley, B.A., Cox, B., Hutchinson, T., Kavazanjian, E., Orense, R., Pender, M., Wotherspoon, L. (2010) Geotechnical reconnaissance of the 2010 Darfield (New Zealand) earthquake. University of Canterbury. 173pp.

Hamada, M., I. Towhata, S. Yasuda, and R. Isoyama. "Study on Permanent Ground Displacement Induced by Seismic Liquefaction." Computers and Geotechnics 4.4 (1987): 197-220. Print.

Krause, Keith S. "WorldView-1 Pre and Post-launch Radiometric Calibration and Early On-orbit Characterization." Proc. of SPIE 7081 (2008)

Leprince, S., S. Barbot, F. Ayoub, and J. Avouac. “Automatic and Precise Orthorectification, Coregistration, and Subpixel Correlation of Satellite Images, Application to Ground Deformation Measurements.” IEEE Transactions on Geoscience and Remote Sensing 2007.

Pradel, Daniel, Joseph Wartman, and Binod Tiwari. "Impact of Anthropogenic Changes on Liquefaction along the Tone River during the 2011 Tohoku Earthquake." *Natural Hazards Review* 15.1 (2014): 13-26. Print.

Puymbroeck, Nadège Van, Rémi Michel, Renaud Binet, Jean-Philippe Avouac, and Jean Taboury. "Measuring Earthquakes from Optical Satellite Images." *Applied Optics* 39.20 (2000): 3486. Print.

Robinson, K., Cubrinovski, M., & Bradley, B. “Lateral Spreading Measurements from the 2010 Darfield and 2011 Christchurch Earthquakes”. Paper presented at the Australia New Zealand Conference on Geomechanics (ANZ), Melbourne, Australia. (2012).

Robinson, K., M. Cubrinovski, P. Kailey, and R. Orense. “Field Measurements of Lateral Spreading following the 2010 Darfield Earthquake.” *Proceedings of the Ninth Pacific Conference on Earthquake Engineering* Apr. 2011: 52-60.

Suncar, Oscar E., Ellen M. Rathje, and Sean M. Buckley. "Deformations of a Rapidly Moving Landslide from High-Resolution Optical Satellite Imagery." *Geocongress* (2013).

USGS. Shuttle Radar Topography Mission, 3-arc second scene s44_e172_3arc_v1, Version 1.0 2004. Data available from the U.S. Geological Survey at eros.usgs.gov

Wei, Shengji, Anthony Sladen, and ARIA Group. "Slip-History Database :: 2011 Tohoku-oki Earthquake." *2011 Tohoku-oki Earthquake*. Caltech, n.d. Web. 28 Apr. 2014. <http://www.tectonics.caltech.edu/slip_history/2011_taiheiyo-oki/>.

Wotherspoon, Liam M., Michael J. Pender, and Rolando P. Orense. "Relationship between Observed Liquefaction at Kaiapoi following the 2010 Darfield Earthquake and Former Channels of the Waimakariri River." *Engineering Geology* 125 (2012): 45-55. Print.

Important Notice:

Figures 3.15, 3.16, 3.17, 3.18, 3.19, 3.20, 3.21, 3.22, 3.23, 3.24, 3.25, 3.26, 3.27, 3.28, 4.11, 4.12, 4.13, and 4.14 were created from maps and/or data extracted from the Canterbury Geotechnical Database (https://canterburygeotechnicaldatabase.projectorbit.com), which were prepared and/or compiled for the Earthquake Commission (EQC) to assist in assessing insurance claims made under the Earthquake Commission Act 1993. The source maps and data were not intended for any other purpose. EQC and its engineers, Tonkin & Taylor, have no liability for any use of the maps and data or for the consequences of any person relying on them in any way. This "Important notice" must be reproduced wherever Figures 3.15, 3.16, 3.17, 3.18, 3.19, 3.20, 3.21, 3.22, 3.23, 3.24, 3.25, 3.26, 3.27, 3.28, 4.11, 4.12, 4.13, or 4.14 or any derivatives are reproduced.